TFT-Based Active Pixel Sensors for Large Area Thermal Neutron Detection

by

George Kunnen

A Dissertation Presented in Partial Fulfillment
of the Requirements for the Degree
Doctor of Philosophy

Approved July 2014 by the
Graduate Supervisory Committee:

David Allee, Chair
Douglas Garrity
Bruce Gnade
Keith Holbert

ARIZONA STATE UNIVERSITY

August 2014

ABSTRACT

Due to diminishing availability of ^{3}He, which is the critical component of neutron detecting proportional counters, large area flexible arrays are being considered as a potential replacement for neutron detection. A large area flexible array, utilizing semiconductors for both charged particle detection and pixel readout, ensures a large detection surface area in a light weight rugged form. Such a neutron detector could be suitable for deployment at ports of entry. The specific approach used in this research, uses a neutron converter layer which captures incident thermal neutrons, and then emits ionizing charged particles. These ionizing particles cause electron-hole pair generation within a single pixel's integrated sensing diode. The resulting charge is then amplified via a low-noise amplifier. This document begins by discussing the current state of the art in neutron detection and the associated challenges. Then, for the purpose of resolving some of these issues, recent design and modeling efforts towards developing an improved neutron detection system are described. Also presented is a low-noise active pixel sensor (APS) design capable of being implemented in low temperature indium gallium zinc oxide (InGaZnO) or amorphous silicon (a-Si:H) thin film transistor process compatible with plastic substrates. The low gain and limited scalability of this design are improved upon by implementing a new multistage self-resetting APS. For each APS design, successful radiation measurements are also presented using PiN diodes for charged particle detection. Next, detection array readout methodologies are modeled and analyzed, and use of a matched filter readout circuit is described as well. Finally, this document discusses detection diode integration with the designed TFT-based APSs.

ACKNOWLEDGEMENTS

I would like to especially thank my advisor Dr. Allee for all of his expert advice and encouragement. I am also incredibly thankful for my colleagues Joseph Smith, Edward Lee, Daniel Pressler, Hugh Chung, Anthony Pelot, and Alfonso Dominguez, and for all of their contributions to this research. I would also like to thank my collaborators at UTD -- John Murphy, Israel Mejia, Bruce Gnade, and Dr. Manuel Quevedo. In addition, I am very grateful for the Flexible Display Center (FDC) engineering team, and for their advancing development in flexible electronics. Research at the FDC was sponsored by the Army Research Laboratory (ARL) under Cooperative Agreement W911NG-04-2-0005. Research at the FDC was also sponsored by the Domestic Nuclear Detection Office under award ECCS-114004.

Finally, I would like to thank my family, and especially my wife Jill, whose love and support have ultimately carried me through this process.

TABLE OF CONTENTS

Page

CHAPTER Page

CHAPTER Page

LIST OF FIGURES

Figure Page

Figure Page

Figure Page

Figure Page

LIST OF ACRONYMS

APS	Active Pixel Sensor
a-Si:H	Hydrogenated Amorphous Silicon
ASU	Arizona State University
CDS	Correlated Double Sampling
COTS	Commercial Off the Shelf
CSP	Charge Sensitive Preamplifier
CS	Common Source (Amplifier)
DRAM	Dynamic Random Access Memory
FDC	Flexible Display Center
HEU	Highly Enriched Uranium
InGaZnO or **IGZO**	Indium Gallium Zinc Oxide
LLD	Lower Level Discriminator
MCA	Multichannel Analyzer
MCNP	Monte Carlo N-Particle
MCNPX	Monte Carlo N-Particle eXtended
PCB	Printed Circuit Board
PPS	Passive Pixel Sensor
SNM	Special Nuclear Material
TFT	Thin Film Transistor

1. INTRODUCTION

1.1 The ^{3}He Dilemma

^{3}He functions as the vital component in today's gas-filled neutron detectors. The inert gas is produced primarily through the radioactive beta decay of tritium (with a half-life of about 12.3 years). The current supply of tritium (and thus ^{3}He as well) originates primarily from the dismantlement of the nuclear stockpile during the post-cold war era. Thus, since tritium production has essentially ceased, there is a simultaneous stop in ^{3}He production as well [9][10]. Following the terrorist attacks on September 11, 2001, there has been steadily increasing demand for neutron detection systems at ports of entry [7][9]. These systems must detect the spontaneous neutrons emitted from Special Nuclear Material (SNM) and thereby interdict said material. As the current technology in neutron detection has primarily used ^{3}He-based detectors, there has been an increased demand for the gas. However, the combination of increased demand and ceased production, have resulted in a continuously dwindling supply of ^{3}He [9]. In order to address this problem, efforts are being made to create new detection systems able to replace the current ^{3}He-based neutron detectors, yet still detect SNM effectively. This research is motivated by these efforts, and is focused on devising a neutron detection system capable of replacing ^{3}He proportional counters in the role of SNM detection and interdiction.

1.2 Outline of Presented Research

The rest of Chapter 1 describes the background and state of the art for neutron detection. Chapter 2 describes the system modeling and optimization of the front-end conversion-layer-based neutron detector. Chapter 3 discusses earlier active pixel sensor (APS)

designs of this research along with measured results. Chapter 4 presents the initial multi-stage APS design along with simulated and measured experimental results. Chapter 5 presents further improvements to the new multi-stage APS design. Chapter 6 discusses array operation and scaling. Chapter 7 discusses the design of a matched filter for use in array readout. Chapter 8 discusses and presents data relating to suitable detection diodes for integration on the designed APS. Finally, Chapter 9 concludes with recommended future work.

1.3 Background: Thermal Neutron Detection State of the Art

This research primarily investigates the passive detection of thermal/"slow" neutrons (generally ranging below energies of 0.5 eV). Thus, the following pages will delve largely in modern thermal neutron detectors, and discuss the necessary background associated with thermal neutron detection methods. Other techniques such as active neutron detection and fast neutron spectroscopy are not discussed in this manuscript in the interest of brevity.

Unlike most other radiated particles, which carry either a positive or negative charge, neutrons by nature, are neutral. This means that they cannot ionize other atoms by means of a coulombic interaction. In fact, if a neutron is to interact with another atom, it will be only with the nucleus. Consequently, the specific nuclear reaction will depend on the type of target nucleus the neutron interacts with, and the kinetic energy of the neutron itself.

One of two types of universal interactions may occur when a neutron strikes a target nucleus. The neutron will either undergo a scattering (which can be either elastic or inelastic), or it will be absorbed. Elastic scattering produces a recoil nucleus, where inelastic

scattering produces an excited nucleus which eventually de-excites through the release of gamma rays [1]. In the absorption interaction, one of multiple reactions may also occur. These include electromagnetic absorption (gamma rays are released), neutral absorption (more neutrons are released), fission (fission fragments are released), and finally charged absorption (charged particles are released) [1]. Most commonly used in thermal neutron detection, is the charged absorption mechanism. Although some other detectors utilize the other absorption mechanisms for detection – neutron detection techniques by means of charged absorption will be the primary subject of discussion in the following pages.

The basics of thermal neutron detection methods center on an incident slow neutron being absorbed in a specialized target material. The subsequent release of charged particles due to the absorption reaction can then be detected. Thus, it becomes particularly important to maximize neutron absorption in which charged particles are released as a result. Due to this fact, the target material in the detector requires an optimal neutron absorption cross section. The neutron cross section essentially is a measure of the probability of a neutron interaction taking place within a specific target material. Thus, a target material for slow neutron detection must not only produce charged particles during an absorption -- but also have a high probability of absorbing a thermal neutron (i.e. have a high absorption cross section). As a result, slow neutron detectors commonly use either ^{3}He, ^{10}B, or ^{6}Li, as target materials because they all fulfill these criteria. Below in Table 1.1, is a summary of these target materials, and the resulting energies of the reaction products due to thermal neutron absorption [1]. One can also observe the total neutron absorption cross sections for the target materials presented in Table 1.1. Note here, that a "Barn" is defined as a unit of area (1 Barn = 10^{-28} m^2), and is used to measure the

effective cross sectional are of an atom. One might also think of this measure as a probability of a certain type of nuclear interaction occurring.

Table 1.1: Key materials and interactions used in charged absorption reactions with thermal neutrons. Information collected from [1].

Target Isotope	**Thermal Neutron Cross-Section [Barns]**	**Reaction**	Q-value [MeV]	Reaction Products and Respective Energies
^{3}He	5333	$^{3}He + {}^{1}n \rightarrow {}^{3}H + {}^{1}p$	0.764	^{3}H: .191 MeV ^{1}p: .573 MeV
^{10}B	3835	$^{10}B + {}^{1}n \rightarrow {}^{7}Li^{*} + {}^{4}\alpha$ *(94%)*	2.31	$^{7}Li^{*}$: .84 MeV $^{4}\alpha$: 1.47 MeV
		$^{10}B + {}^{1}n \rightarrow {}^{7}Li + {}^{4}\alpha$ *(6%)*	2.792	^{7}Li: 1.015 MeV $^{4}\alpha$: 1.777 MeV
^{6}Li	940	$^{6}Li + {}^{1}n \rightarrow {}^{3}H + {}^{4}\alpha$	4.78	^{3}H: 2.73 MeV $^{4}\alpha$: 2.05 MeV

Such target isotopes as ^{3}He and ^{10}B, are commonly implemented in proportional counter-based neutron detectors. A general overview of proportional counters needs to be covered in order to better understand how detectors such as those incorporating ^{3}He and ^{10}B function.

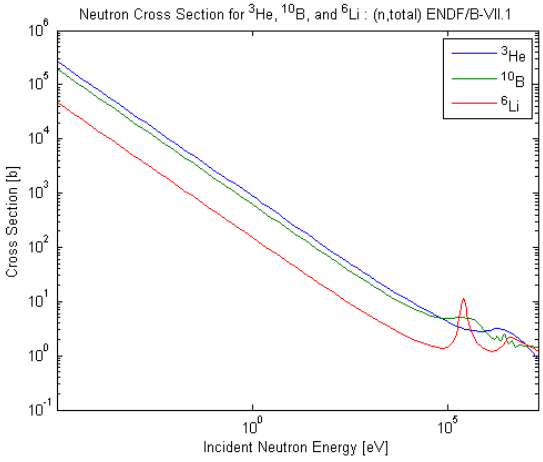

Figure 1.1: Total Neutron Cross Sections for various materials. Data plotted was retrieved from [2].

1.3.1 Proportional Counter

Gaseous proportional counters (most notably ^{3}He proportional tubes) are the core in current neutron detection. Proportional counters implement a gas-filled ionization chamber for detection. A gas ionization chamber uses a confined volume of gas along with an electric field to detect ionizing radiation. Upon incident ionizing radiation, pairs of electrons and positively-charged ions are formed within the gas, and swept to the appropriate electrodes due to the electric field.

Once the electrons reach the anode of the detector (the positive ions reach the cathode sometime after, as they travel at a slower rate), a current pulse may be measured. On a characteristic I-V plot, positive slope will indicate, the applied voltage is low enough such that recombination of some electrons and ions still occur within the gas (before they can reach an electrode). When the voltage reaches a critical point, the electric field in the gas enclosure is large enough in order to eliminate recombination, and the slope will approach zero. From this point on, the current pulse will remain constant, as each electron-ion pair will be measured and the radiation rate will remain constant. This changes when the electric field is greatly increased within the chamber. This is where proportional counters come into play.

As the electric field in the ionization chamber increases past a certain point, a phenomenon known as a Townsend avalanche begins to occur [1]. This is where the electrons created from the ionizing radiation gain enough energy through acceleration in the electric field that they themselves free additional electrons through the ionization of other atoms in the gas. These newly freed electrons may also free even more electrons if they reach a high enough kinetic energy. The end result is a much greater current pulse than

that seen in an ionization chamber. An illustration portraying the operation of such a device can be seen in Figure 1.2.

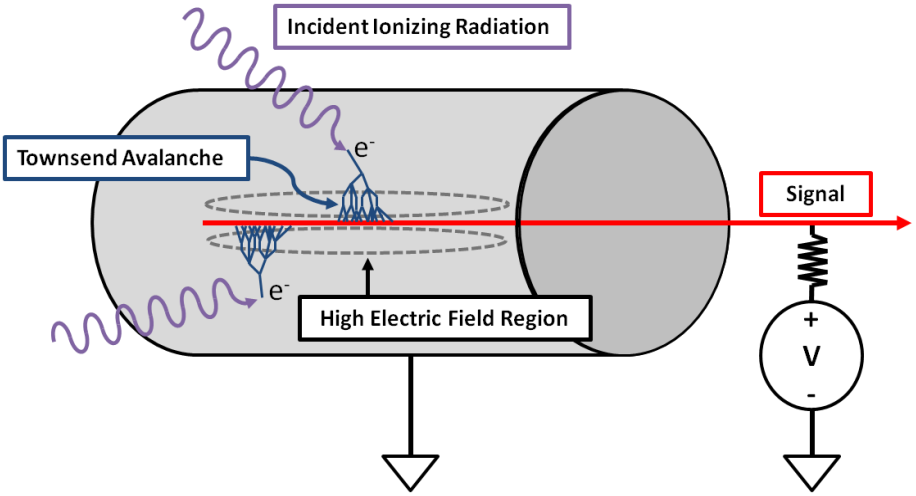

Figure 1.2: Illustration portraying operation of a proportional counter.

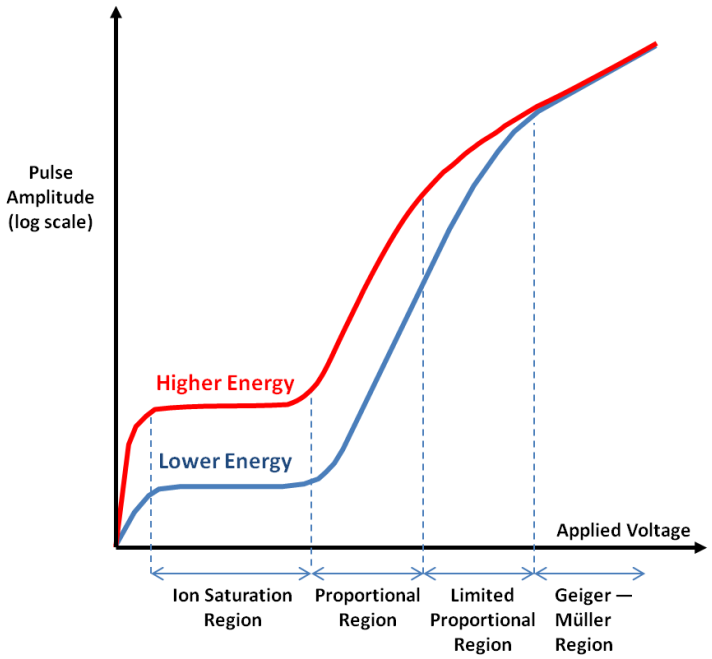

Figure 1.3: Graph showing the effect of increasing applied voltage in a gas-filled detector. Image redrawn from data presented in reference [1].

Figure 1.3 shows how the measured current is affected when the applied voltage is increased a great degree. It is important to note that the proportional fill gas needs to be chosen to have a low electron attachment coefficient in order to allow gas multiplication to occur. So for instance, oxygen would be a poor fill gas due to being electronegative. Thus, noble gases, most commonly argon, are often used as proportional gases in these detectors.

In the proportional counters, the applied voltage to the chamber is carefully chosen such that a high gain of electric charge is generated proportionally depending on how much energy each event deposits in the detection medium. This allows one to still determine the original energy of the ionizing radiation. If the applied voltage is too much, however (as seen in the Geiger-Mueller region in Figure 1.3), then information concerning the original deposited energy is lost, as the avalanching reaches such a degree that any ionizing radiation will trigger the same amount of charge collected at each electrode. Typical operating voltages for a BF_3 proportional counter for example, will be in the range of 2000-3000 Volts [1].

1.3.1a Implementation of the ^{3}He(n, p) reaction

According to Figure 1.1, ^{3}He has the largest thermal neutron cross section when compared to its lithium and boron counterparts. The thermal neutron cross section of ^{3}He is 5333 barns. Because of this, the primary advantage of ^{3}He proportional counters lies in their intrinsic detection efficiency (the amount of detector counts due to one neutron strike). Intrinsic efficiencies of ^{3}He proportional counters have been reported as high as 77% [7]. Upon absorption of a thermal neutron, two reaction products are formed. These two charged particles are a tritium atom (^{3}H) and a proton.

$$^{3}He + {}^{1}n \rightarrow {}^{3}H + {}^{1}p$$

For this specific reaction, the Q-value is .764 MeV. The Q-value essentially highlights the difference in energies between the reactants, and the products of the reaction. If the Q-value is positive, the reaction is exothermic and has an overall release of energy. If the Q-value is negative, then the reaction is endothermic, and needs an overall input of energy to allow the reaction to take place. In the case of the $^{3}He(n, p)$ reaction, there is an overall release of energy. As the incoming neutron is assumed to have a very low kinetic energy (in the eV ranges) and the ^{3}He atom is stationary, the large Q-value reflects the energy of the reaction products. As momentum is conserved between the two reaction products, their energy may easily be calculated using the Q-value and the mass of each reaction product. The kinetic energy values are .573 MeV and .191 MeV for the proton and the tritium atom respectively [1].

The high energy reaction products of the $^{3}He(n, p)$ reaction have enough energy to remove electrons from the orbitals of other target atoms. It is through this process that electron and positive ion pairs are created within the detector. It is worthwhile to note here as well, that the charged reaction products must deposit most, if not all of their energy into the detector medium, for the sake of maintaining a tight energy resolution. In the case of the $^{3}He(n, p)$ reaction, it is optimal to detect these electron-ion pairs using a proportional counter. As ^{3}He is better suited in gaseous form, it works both as a neutron converter material and as a proportional gas (a significant advantage). When characterizing such a detector, it becomes useful to analyze the differential pulse height spectrum. The differential pulse height spectrum essentially plots the differential number of pulses

recorded with respect to pulse height or respective energy (*dN/dE*) vs. the energy deposited in the detection medium. This may be seen in Figure 1.4. The differential pulse height spectrum is analogous to the "real-life" output of a multichannel analyzer (MCA) -- which tallies the amount of pulses occurring within each bin, of a set of energy bins.

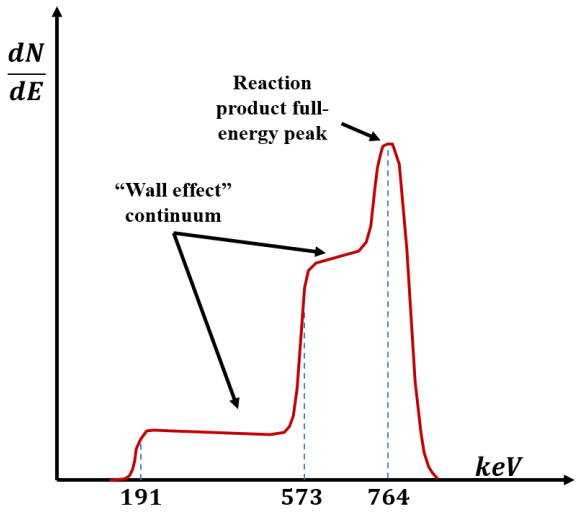

Figure 1.4: Differential pulse height spectrum for a ^{3}He based neutron detector (Figure re-drawn from [1])

Ideally, the pulse height spectrum should simply have a large spike around 764 keV – the Q-value of the reaction. This would mean that all reaction products deposit their energy in the detection medium. In reality, however, some reaction products may strike the walls of the detector and not deposit all of their energy within the detection medium. This consequently leads to "steps" in the differential pulse height spectrum. The lower step in Figure 1.4 is when the proton strikes the wall of the detector, and only the ^{3}H particle deposits its energy of 191 keV. The intermediate step is when the ^{3}H particle strikes the wall, and the proton deposits its energy of 573 keV. This effect, commonly known as the "wall effect", is primarily due to the dimensions of the detector, and the

pressure of the proportional fill gas – not the energy of the neutron. Both the dimensions of the detector tube (especially the diameter) and the pressure of the fill gas can be increased as needed in detector design, in order to achieve a more precise energy peak at the Q-value resolution, and thereby increasing detection efficiency [1].

It should also be noted that gamma rays (which are often a parasitic background source in neutron detection) [5][7], can produce secondary electrons within the walls of the detector. However, the electrons have very long range within gas. Thus, they only deposit a fraction of their energy within the proportional gas. These parasitic pulses are therefore very small when compared to the pulses due to the ionization caused by the reaction products. These small pulses due to gamma rays may be seen later in Figure 1.5 (when discussing BF_3 proportional counters in this case), and can easily be filtered out through pulse amplitude discrimination [1]. This gamma-rejection capability of gaseous proportional counters, presents a key advantage in the interdiction of SNM.

1.3.1b Implementation of the $^{10}B(n, \alpha)$ reaction

The primary disadvantages of ^3He proportional counters, lie primarily in their need of ^3He (as discussed before). This implies a large and increasing cost of production. One of the first obvious alternatives for solving this issue, is directly replacing ^3He tubes with proportional counters using ^{10}B (i.e. BF_3 filled proportional counters or ^{10}B lined proportional counters) [9].

With a smaller thermal neutron cross section of 3835 barns (when compared to that of ^3He), ^{10}B is still likely to undergo slow neutron capture. However, now proportional counters using ^{10}B, need to be scaled up in size in order to maintain a comparable neutron

sensitivity to that of ^{3}He proportional counters. Another major drawback of BF_3 counters specifically, is the toxicity that the gaseous BF_3 presents [7][9]. This makes it much more difficult to maintain and operate the proportional tubes.

Nevertheless, it is worthwhile discussing the use of the $^{10}B(n, \alpha)$ reaction in gaseous neutron detection. The $^{10}B(n, \alpha)$ reaction may be seen below.

$$^{10}B + {}^{1}n \rightarrow {}^{7}Li^{*} + {}^{4}\alpha$$

The total Q-value of the most probable state is 2.31 MeV (where the lithium atom is excited). The energies of the reaction products are 0.84 MeV for ^{7}Li and 1.47 MeV for $^{4}\alpha$. There is a 6% chance that the reaction leads to the ground state (where the lithium atom is not excited). This reaction has a slightly higher Q-value of 2.792 MeV. As ^{10}B cannot be manufactured in gaseous form, this detector uses BF_3 as a fill gas and is enriched to 96% ^{10}B, in order to better facilitate the ^{10}B neutron capture. The differential pulse height spectrum may be seen in Figure 1.5. The first graph shows the spectrum where all reaction products deposit their entire energy in the detection medium. The second graph shows the spectrum of a smaller proportional tube in which the wall effect takes place.

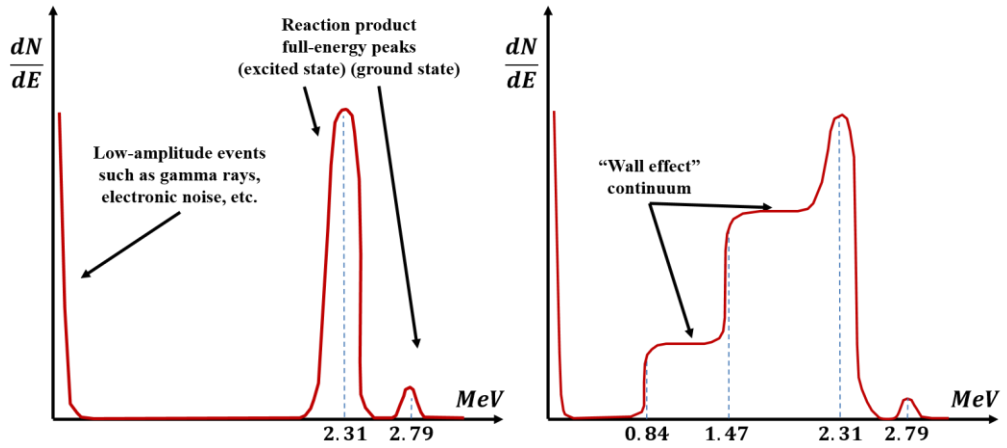

Figure 1.5: Differential pulse height spectrum for a BF_3 proportional counter. The left spectrum corresponds to a large proportional tube, while the right spectrum corresponds to a smaller proportional tube. (Figure re-drawn from [1])

As described with the ^{3}He proportional counter, the wall effect in the pulse height spectrum may be reduced by increasing the dimensions of the proportional tube and by raising the pressure of the fill gas in the proportional tube [1].

Another detection approach uses a ^{10}B lined proportional counter. This can also be used as a direct replacement of ^{3}He tubes. The advantage of this design is the ability to use a more optimal proportional gas such as P-10, which is 90% argon and 10% methane. In this case, ^{10}B gas enrichment is no longer needed, as pure thin film layer of ^{10}B lines the inside walls of the proportional counter [1][7]. Thus, the neutron conversion takes place at the walls of the proportional tube, and not in the gas. The only drawback in this case, is that only one of the reaction products will deposit energy within the proportional gas, while the other reaction product is lost within the outer walls of the proportional counter. The primary disadvantage to this approach is that since the energy deposited in the detector can be potentially much smaller than that seen in a BF_3 tube. This makes it

is much more difficult to discriminate between gamma ray and neutron strikes during operation [1].

1.3.2 Scintillator-based Neutron Detection

Another common method for detecting neutrons is through the use of scintillators. In short, scintillators are specialized materials that emit photons (fluorescence) upon the absorption of ionizing radiation. There are two main categories of scintillators -- these are organic and inorganic. Organic-based scintillators can be either manufactured as crystals, liquid, or plastic. These scintillators use material based on organic molecules with π-electron structures. Incident radiation excites the electron configuration associated with the entire organic molecule to one of a series of excited states. De-excitation back to the ground state, or its associated vibrational states, causes a release of energy observed through prompt fluorescence. The photons emitted from the scintillators can then be detected using photomultiplier tubes. Due to their low Z (low amount of protons) components, organic scintillators become very attractive in the realm of detecting fast neutrons [1].

In the realm of thermal neutron detection, inorganic scintillators become applicable. Scintillation takes place due to the excitation/de-excitation of electrons in the band structure associated with crystal lattice formation. This is different from organic scintillators, in which the scintillation process is due to changing energy states of the electron configuration in the molecule. Upon absorbing enough energy from ionizing radiation (generally enough to surpass the band gap energy), valence electrons become excited, and move from the valence band to the conduction band leaving a hole in the valence band. Through

the addition of activator impurities in the crystal, the electron is able to neutralize an ionized activator site (the activator site is ionized due to the mobile hole in the lattice), while remaining between the valence and conduction bands. In general, this activator site will occupy an excited configuration of its own, and through de-excitation to the ground state configuration, will release photons (refer to Figure 1.6) [1].

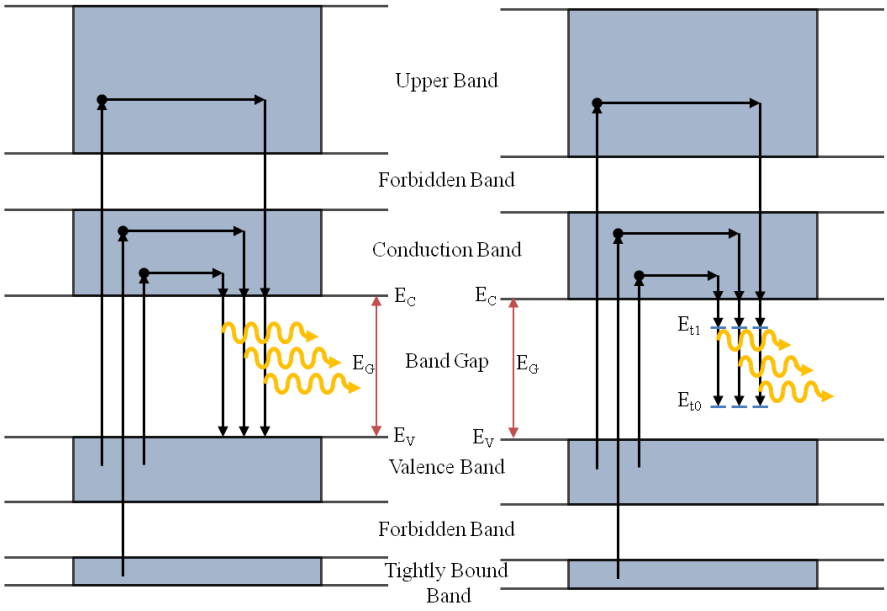

Figure 1.6: Illustration of an inorganic scintillator. The scintillator on the left portrays scintillation photons being released through de-excitation directly from the conduction band. The scintillator on the right portrays de-excitation from one of the excited states of an activator sight to the ground state. Image redrawn from diagram in reference [3]

Through this process, less energy will be released than if the electron had de-excited directly from the conduction band to the valence band. This allows for smaller energies of the scintillation photons, which translates to more visible photon wavelengths. Additionally, the radiated energy of photons emitted during de-excitation directly from the conduction band to the valence band, will often be re-absorbed into the scintillator and not be radiated as prompt luminescence. As the reabsorbed photon reflects the band gap

energy, it could potentially excite more electrons to the conduction band. This means that the scintillator would be opaque to its own emitted light (an undesirable effect). With the addition of impurities, however, the smaller energy associated with the scintillation photon, decreases the likelihood of the photon being reabsorbed and exciting other electrons [3].

The ^{6}Li(n, α) reaction and its use scintillators:

With a comparably smaller (yet still significant) thermal neutron cross section of 940 barns, ^{6}Li presents another viable replacement of ^{3}He as a thermal neutron converter. For instance, Pacific Northwest National Laboratory has implemented ^{6}Li-doped scintillating fibers and reported intrinsic detection efficiencies comparable to those seen in ^{3}He proportional counters [7]. However, as will be described later, this detector suffers from low gamma-ray rejection [9]. The neutron absorption equation for ^{6}Li is given below.

$$^{6}\text{Li} + {}^{1}\text{n} \rightarrow {}^{3}\text{H} + {}^{4}\alpha$$

The total Q value of this reaction is 4.78 MeV, with reaction product energies of 2.73 MeV and 2.05 MeV for the ^{3}H and the α particles respectively [1]. Unlike with detectors utilizing boron and helium, lithium cannot be stably produced as a proportional gas. Thus, most neutron detectors utilizing the ^{6}Li(n, α) reaction incorporate lithium iodide crystals as scintillators. Crystalline lithium iodide bears many similarities to the more common sodium iodide (NaI) used in most inorganic scintillators. Unlike in proportional counters, the range of the reaction products within the crystal is relatively small. Thus, the wall effect is not apparent in the lithium iodide scintillators, as all the reaction prod-

ucts from a neutron capture will deposit all of their energy within the medium. The primary drawback to this system is that secondary electrons produced by gamma rays for instance, will generally have a very short range as well (which is not true in gas), and will deposit their entire energy (in the range of 4 MeV) within the medium. This makes it much more difficult to distinguish between a gamma ray strike and a neutron strike, when observing the pulse height distribution [1].

1.3.3 Thin film conversion-layer-based detector (Approach used in this Research)

Detectors using thin film conversion layers (incorporating ^{10}B or ^{6}Li primarily), have also become attractive replacements for proportional tubes. Detectors based on thin film conversion layer technology especially have the potential for low-cost, and large-scale production. These are both significant advantages over the more expensive and localized gaseous proportional counters [11]. Some detector designs simply coat the inside of proportional counters or ionization chambers with thin film neutron conversion layers (as described before with ^{10}B lined proportional tubes). These detectors are limited to an upper limit of 50% intrinsic efficiencies [7]. However, as described before, this requires the constant operation and maintenance of a gas-filled proportional tube. Thus, the rest of this discussion will primarily focus on using thin film neutron conversion layers without the need of proportional counters -- namely in combination with a semiconductor-based charged particle detector, i.e. a diode.

Referring to Figure 1.7, one can observe the overall structure and mechanisms by which thermal neutrons enter a thin film conversion layer (in this case, pictured is a ^{10}B layer), and are consequently absorbed. A resulting neutron charged absorption reaction

creates two charged particles which travel in opposite directions. One of these particles can enter the semiconductor detection volume. This volume represents the depletion region of a reverse-biased diode (the intrinsic region of a PiN diode for example). While the charged particle travels through the depletion region it slows down through coulombic scattering, and therefore causes electron-hole pairs to be generated along its path of flight [4]. Due to the reverse-bias of the diode, the generated electrons and holes within the depletion region, are swept to their respective electrodes, and thereby create an induced charge on the contacts. This charge can then be detected through various methods of amplification.

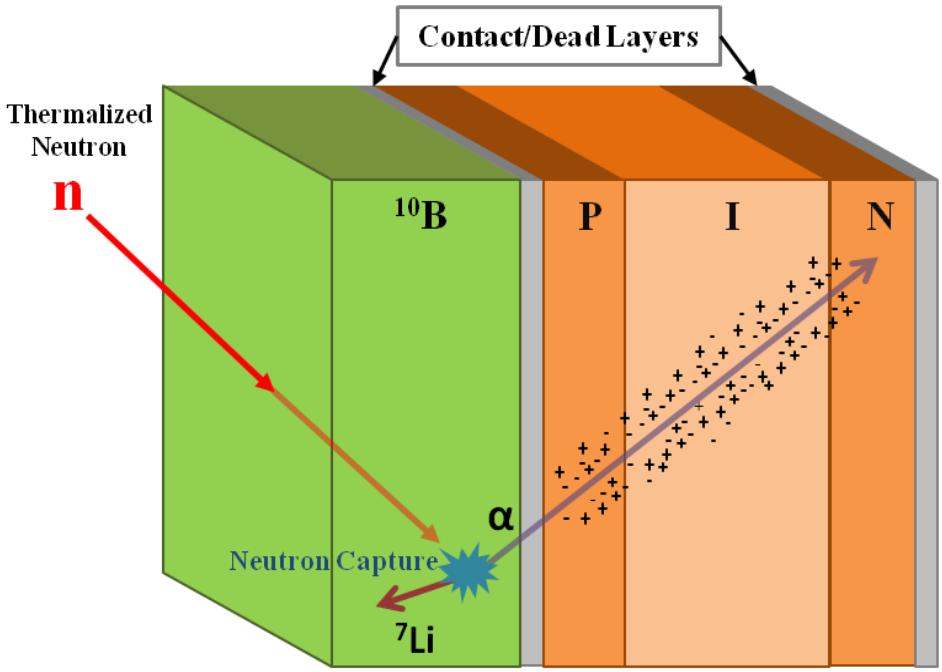

Figure 1.7: Diagram portraying the mechanisms by which neutrons are detected with thin film conversion layers.

The primary drawback of this type of detector is the low intrinsic thermal neutron detection efficiency. Ideally, the charged particles emitted from the neutron absorption need to deposit all of their energy within the detector volume to ensure good energy resolution, and maximum detectability. However, since, the neutron absorption takes place outside of the detector volume (i.e. in the conversion layer), the emitted charged particles will always lose at least a fraction of energy before leaving the conversion layer. In fact, if the conversion layer is too thick, the charged reaction products will be absorbed in the conversion layer, and will never have a chance to enter the detector volume (this is known as self-absorption). However, if the conversion layer is too thin, the chances of neutron absorption decrease significantly. To make matters worse, only one charged particle from the neutron absorption can ever enter the detection volume. Using a planar geometry, with an optimized ^{10}B layer thickness, yields a maximum intrinsic detection efficiency of about 4%. Using ^{6}LiF instead results in a slightly higher efficiency of 4.4% [4].

To increase intrinsic efficiency, converter/detector geometries differing from the planar form shown in Figure 1.7, have been used in order to maximize the probability of charged reaction products entering the detector volume. As reported by Nikolic et al., a pillar-based design implemented with ^{10}B is reported to have 7.3% intrinsic detection efficiency [12]. Layering different types of conversion layers on one another (such as $^{6}Li/^{10}B$) in conjunction with a detection diode, can also significantly increase intrinsic detection efficiencies up to 13.5% as reported by McGregor et al. [4] . Another technique proposed by McHugh et al., suggests using multi-layer conversion layer/diode detectors to enable intrinsic detection efficiencies comparable to ^{3}He proportional counters [11].

Even though these detectors exhibit low intrinsic detection efficiencies when compared to ^{3}He proportional counters, large surface area implementation allows for greater collection efficiency (percentage of neutrons striking the detector per neutron emitted from SNM). Thus it is feasible to achieve absolute detection efficiencies in detecting SNM comparable to those seen with ^{3}He. Furthermore, the possibility of leveraging the low-cost and large-area manufacturing capabilities of the flat-panel display industry to implement detection arrays (utilizing thin film neutron conversion layers) is an especially attractive notion. It is because of these benefits and opportunity for new innovation that this research focuses on developing a detector based off of thin film neutron conversion layers.

2. SYSTEM MODELING AND OPTIMIZATION

2.1 Introduction

It is essential to model the neutron detection system in order to better optimize parameters of the detector, and understand the expected performance. The entire neutron detection system model consists of two primary components. The first model component encompasses the "front-end" nuclear interactions, and resulting ionizing radiation. This component is modeled primarily with **Monte Carlo N-Particle Transport Code (MCNP)**. The second model component encompasses the "back-end" sensing circuitry and read-out arrays. This component is primarily modeled using both **HSPICE** and **MATLAB**. The following discussions will primarily focus on the simulations with MCNPX -- especially when defining the reasons for choosing initial detector parameters. As a reference, one can observe the overall architecture and functioning mechanisms of the neutron detection system in Figure 2.1.

2.2 Detector Front-End Modeling

In simulations, MCNPX is primarily used to determine how spontaneous neutrons from SNM will interact with the designed detector. As a result, MCNPX also provides a means of optimizing detector parameters to ensure the best operating characteristics. The parameters of most importance are the following: the size (primarily thickness) of the neutron conversion layer, the thickness of the diode, and the thickness, composition, and geometry of the neutron moderator.

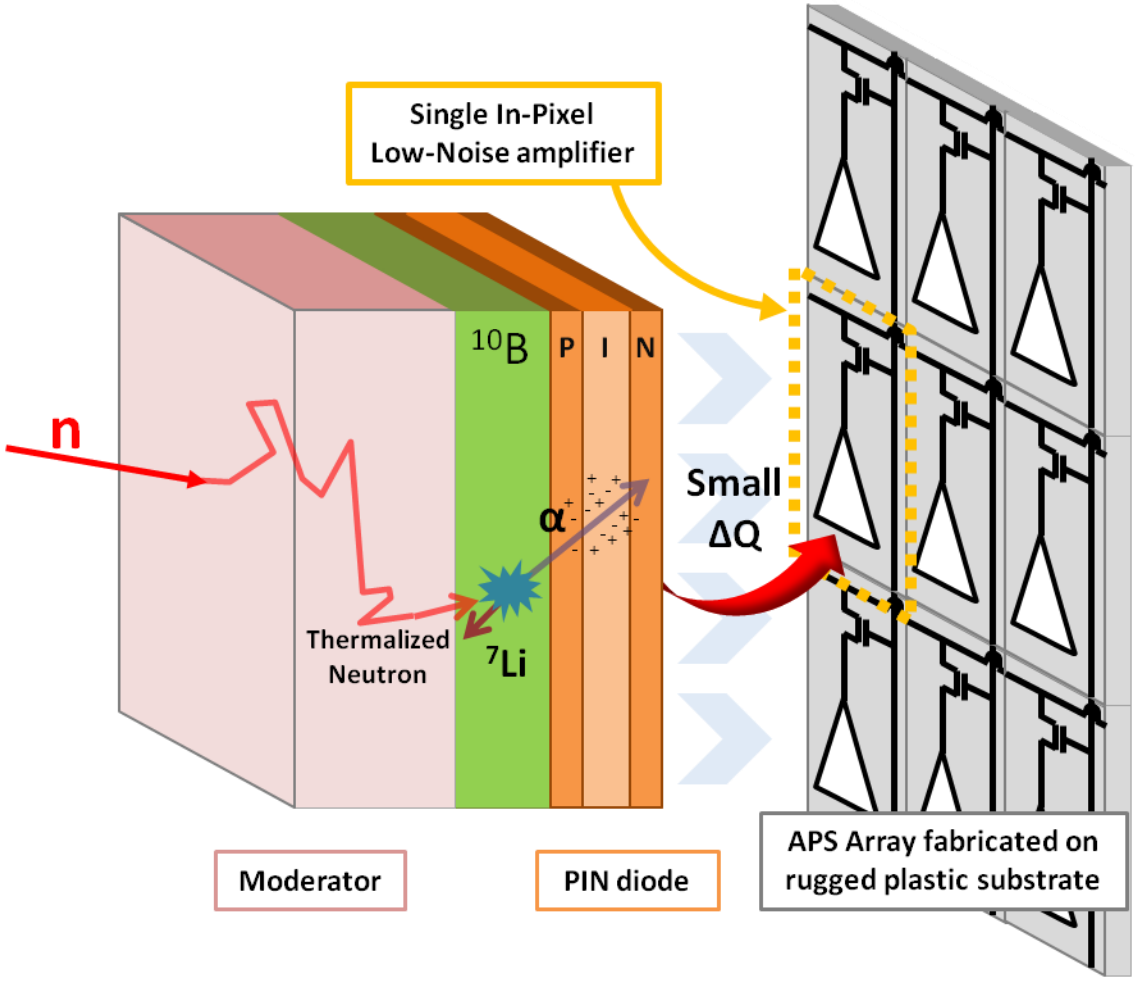

Figure 2.1: Diagram portraying the thermal capture of neutrons, and the subsequent charge collection due to ionizing charged particles.

2.2.1 Modeling the Special Nuclear Material

Before any modeling and optimization of the detector front end can take place, the material being detected needs to be defined and modeled first. Typical special nuclear material (SNM) will usually be enriched with a fissile material (i.e. a material that can undergo a nuclear fission when an incident thermal or fast neutron is absorbed). Examples of such fissile materials are ^{235}U, ^{233}U, and ^{239}Pu. SNM used in nuclear weapons

manufacturing either consist of highly enriched uranium (HEU) or weapons grade plutonium. Kouzes et al. presents two models of SNM -- one with 25 kg of HEU (90% ^{235}U and 10% ^{238}U), and the other with 4 kg of weapons-grade plutonium (90% ^{239}Pu and 10% ^{240}Pu) [8]. In most passive neutron detection techniques, it is more realistic to detect plutonium-based SNM due to its high rate of neutron emission. To further portray this, a 4 kg weapons-grade plutonium example emits $1.11*10^6$ neutrons/sec, whereas a 25 kg HEU example only emits 97 neutrons/sec [8]. Due to the low neutron emission rate of HEU, detection of such material generally falls in the realm of active neutron detection techniques. Thus, the following detection system modeling is based off of the 4 kg weapons-grade plutonium SNM model described in [8].

SNM in general, will emit neutrons at high energy (in the MeV range). This distribution in energy is commonly modeled with the Watt spontaneous fission spectrum. The equation representing the spectrum for a nuclide $\boldsymbol{k}$ can be seen below [13].

$$\boldsymbol{\chi_k^{SF}(E) = R_k(SF) * e^{\frac{-E}{a}} * sinh\sqrt{bE}}$$

$\chi_k^{SF}(E)$ represents the distribution of spontaneous fission (SF) neutrons occurring in nuclide $\boldsymbol{k}$ as a function of energy. $R_k(SF)$ is a normalizing constant representing the average amount of neutrons emitted in the decay of the nuclide. Constants $\boldsymbol{a}$ and $\boldsymbol{b}$ are coefficients used to fit the spectrum to experimental data. All of these values needed for determining $\chi_k^{SF}(E)$ of various nuclides may be found in [13]. The Watt SF spectrum for common nuclides present in SNM is plotted below in Figure 2.2. It should be noted that the distribution was normalized such that the resulting plot was a probability distribution of SF neutrons being emitted with a given energy.

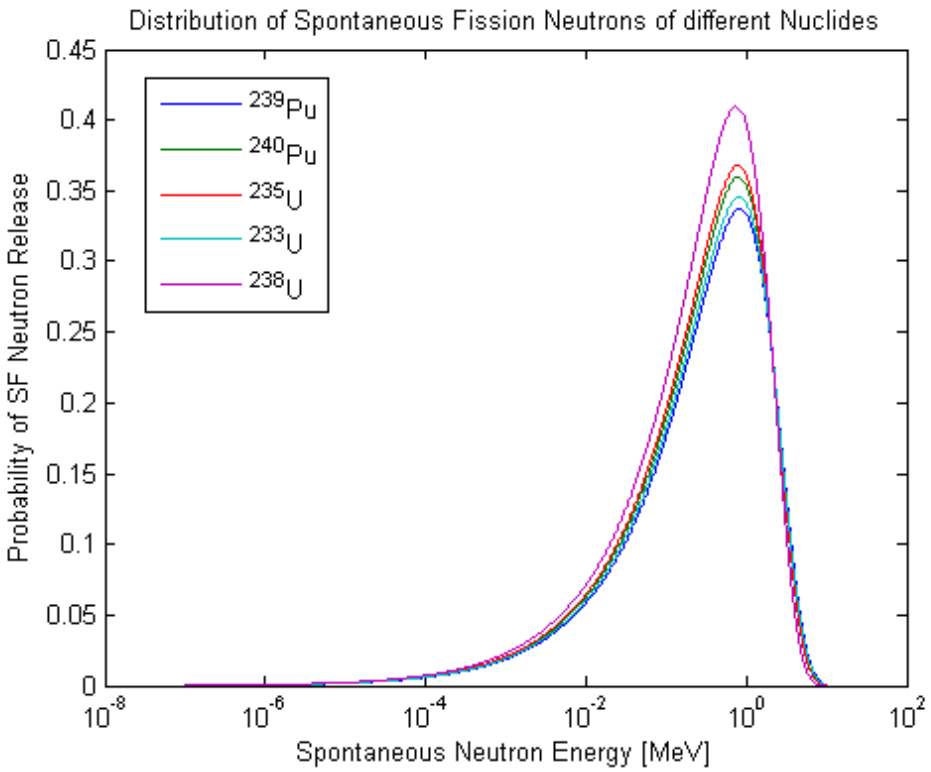

Figure 2.2: Watt spontaneous fission spectrum for common nuclides seen in SNM. The Y axis represents the probability that spontaneous fission neutrons will have a certain energy. Watt fission spectrum parameters were retrieved from [13].

It is clear from this plot, that SNM will most likely emit SF neutrons that range in energies from 1 MeV to about 1 keV. This fact becomes key in the rest of the modeling and design for the front end of the neutron detector.

2.2.2 Initial Moderator Modeling and Optimizations

Due to the fact that at higher energies, neutron absorption cross-sections in converter materials drop off significantly (refer back to Figure 1.1), a thermal neutron detector by itself will have very low detection efficiency. Thus, it is necessary to "slow" the high energy/fast neutrons originating from the SNM (as portrayed in Figure 2.2). This process

is known as neutron moderation. Once sufficiently slowed, the kinetic energy of the incident neutrons are small enough such that the resulting absorption cross-section of the converter material in the thermal neutron detector is high enough to allow a nuclear reaction to occur. The ideal moderator decreases the energy of incident fast neutrons to thermal levels, without absorbing any neutrons during the process. Essentially, this means that a neutron moderator needs to have a high scattering cross section and a low absorption cross section. Materials that exhibit these characteristics are made up of low-Z (low proton) atoms -- most commonly Hydrogen. Thus, solid materials such as paraffin and polyethylene $(C_2H_2)_n$ are often used as moderators in neutron detection applications [7][8].

For the purposes of modeling the moderator material, polyethylene was chosen. A preliminary moderator design implements only one moderating material above the detector volume. Another implementation, similar to the technique reported by Kouzes et al., however, uses a moderator at the back-end of the detector -- which in turn acts as a neutron "reflector" [8]. The general MCNPX simulation setup, which models these two moderation techniques, may be seen in Figure 2.3. It should be noted here as well, that the lateral dimensions of the entire planar detector were 37 cm by 47 cm, for a total surface area of 1739 cm^2. For these simulations, the source was separated by approximately 1 meter of air from the detector. The thicknesses of moderator were varied for each moderating technique, and the resulting neutron flux in the detector volume was tallied with respect to neutron energy. The end results can be seen in Figure 2.4.

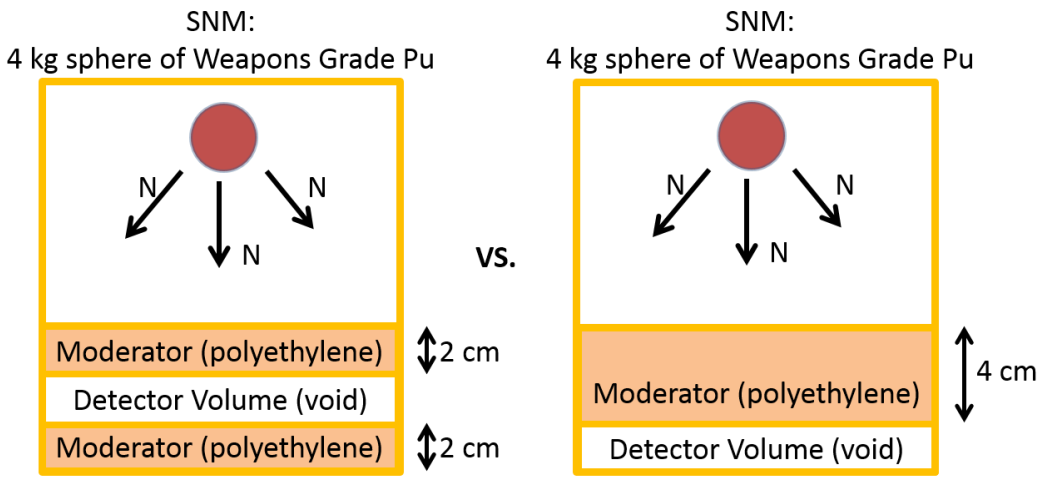

Figure 2.3: MCNPX test setup for modeling and optimizing moderating layers.

The extra moderator on the back-end of the detector increases the chance of neutrons being scattered back to the detector volume, and in the process, increases the thermal neutron flux within the detector volume as well. Thus, based on this simulation, it is optimal to incorporate a two-layer "sandwiched" moderator design with each moderator being 6 cm thick. This moderator thickness agrees closely with the 5 cm thickness chosen in [8]. It should be noted that the moderator thickness on the backside of the detector (i.e. the neutron reflector) can ideally be infinite. However, due to size restrictions, the 6 cm of moderator on each side, serves as a good starting point for further optimizations. In a later section, similar simulations as seen in Figure 2.4 be carried out, while taking into account all of the modeled layers in the detector.

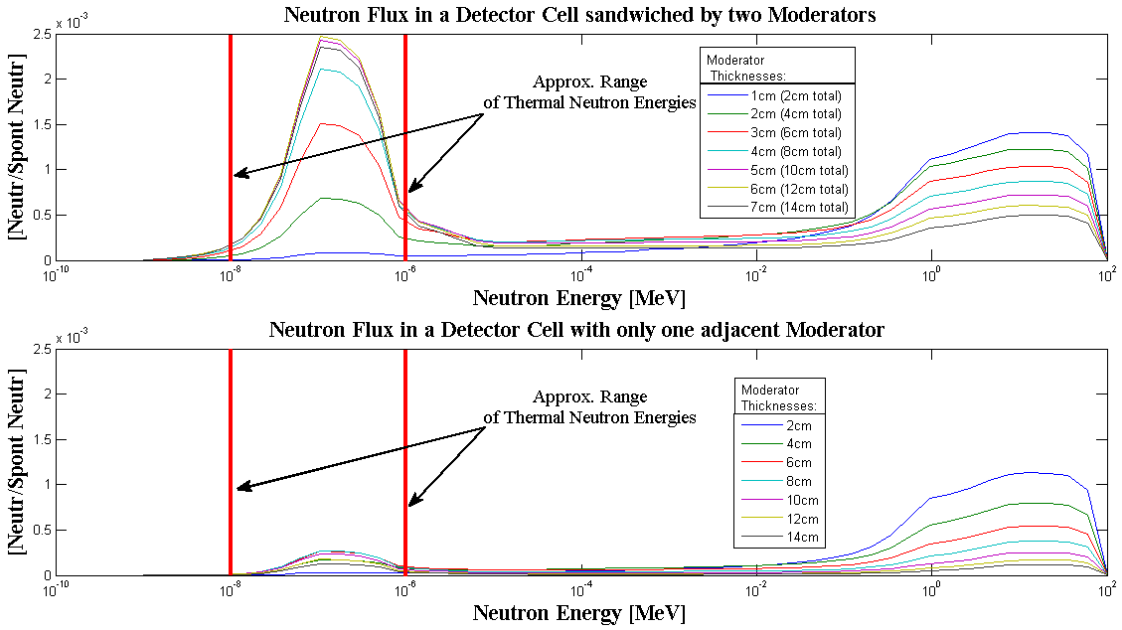

Figure 2.4: MCNPX simulation showing the average neutron flux in the detector volume with respect to neutron energy. The top plot shows the reflector moderating technique, with differing moderator thicknesses. The bottom plot shows the single moderator technique, again with varying thicknesses of moderator. It should be noted that each colored curve corresponds to one total thickness of moderator used (for both plots).

2.2.3 Initial Neutron Conversion Layer Modeling and Optimizations

After optimizing the moderator, it is necessary to model and optimize the conversion layer. In this section, only a single, planar conversion layer will be considered. Other exotic techniques such as using different layers or pillar-based geometries (as described previously), are not modeled in this section. As described before, there needs to be an optimal thickness of conversion layer in order to provide the maximum amount of thermal neutron absorptions, while decreasing the average amount of energy deposited by emitted charged reaction products. Thus, a similar simulation to what was seen in the section before is carried out. In this case, however, the average flux of alpha particles within the

detection volume will be tallied. In this case, the detection volume will remain void (similar to the moderator modeling). The general simulation setup is portrayed in Figure 2.5. With this setup, it was possible to then simulate different conversion layer thicknesses, and then tally the resulting alpha flux (with respect to alpha energy) within the detector volume. The results of this simulation may be seen in Figure 2.6

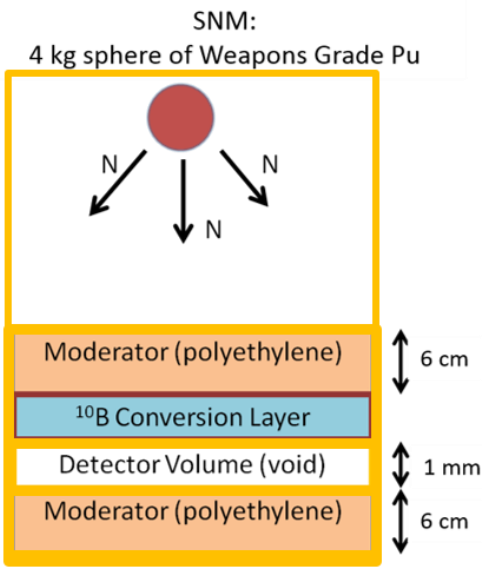

Figure 2.5: Initial modeling setup in MCNPX for optimizing the thickness of the Neutron Conversion Layer (In this case, ^{10}B).

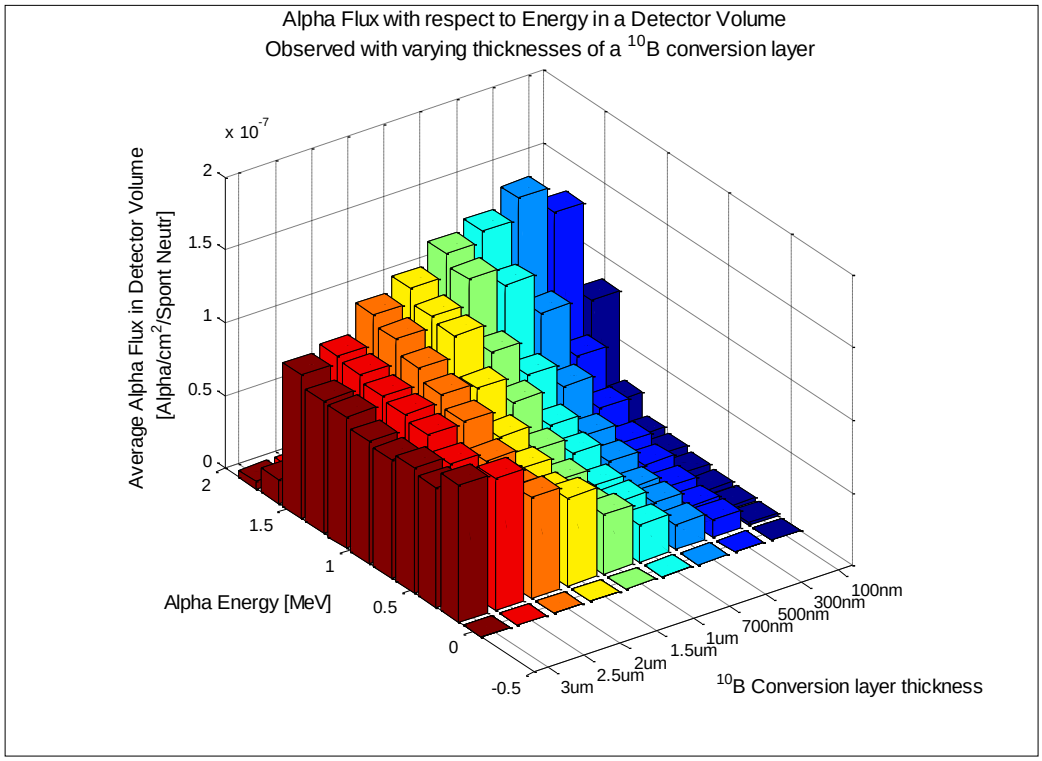

Figure 2.6: MCNPX Simulation showing the average alpha flux (resulting from neutron capture in solid ^{10}B).

From this simulation, it appears that a conversion layer thickness of 0.5 μm will provide a rather tight energy resolution centered on 1.4 MeV. This would be an optimal thickness to choose if the intent of detection was spectroscopy – determining the energy of the alpha particles for example. However, if designing a detector to purely detect the presence of an alpha particle, it is more optimal to choose a conversion layer width that enables the maximum amount of detectable alpha flux within the detector volume. Thus, using the data plotted in Figure 2.6, the maximum total alpha flux is calculated to be approximately: $7.7*10^{-7}$ [Alphas/cm^2/Spontaneous Neutron] achieved at a conversion layer thickness ranging from **2 μm-2.5 μm**. Recall here that in these simulations, the

source was separated by approximately 1 meter of air from the detector. These conversion layer thickness are similar to what is presented in the literature [4], and are good starting points for finer optimizations. Further simulations including more realistic diode layers will be addressed in later sections.

2.2.4 Modeling the Detection Diode

Ultimately, the detection diode absorbs the incident alpha particles emitted from the neutron conversion layer. Specifically, it is the depletion region of the reverse-biased diode in which the incident alpha particles lose energy by means of coulombic scattering, and as a result create electron-hole pairs through the ionization of the targeted silicon atoms. These electron-hole pairs then get swept to their respective electrodes, and cause a detectable change in charge. It is necessary for the depletion region to be thick enough to allow the alpha particles to deposit their total energy (as discussed previously). For this reason, PiN diodes are commonly chosen for the purpose of radiation detection -- as the depletion region must extend across the entire thickness of the intrinsic layer of Si. However, if the diode is made too thick, radiation with higher range (specifically, gamma rays) can begin to contribute to false detection pulses. Thus, it is necessary to implement diodes thin enough to maximize energy deposition from alpha particles, and minimize energy deposition from background gamma ray radiation. According to the literature, however, acceptable gamma ray rejection can be achieved by using diodes thinner than 10 μm [7][12]. For modeling purposes, a 2.4 μm thick diode (where the thickness refers to the intrinsic layer thickness) will be used similar to what is described by McHugh in [11]. Additionally, 2.4 μm thick amorphous silicon (a-Si:H) PiN diodes are capable of being fabricated with the ASU Flexible Display Center's (FDC) process technology [see

Acknowledgments]. Thus, it makes sense to model the diode and associated layers according to the process given. This correlates to a model which can then be potentially fabricated as an actual detector. The appropriate layers used in MCNPX for modeling the diode may be seen in Figure 2.7.

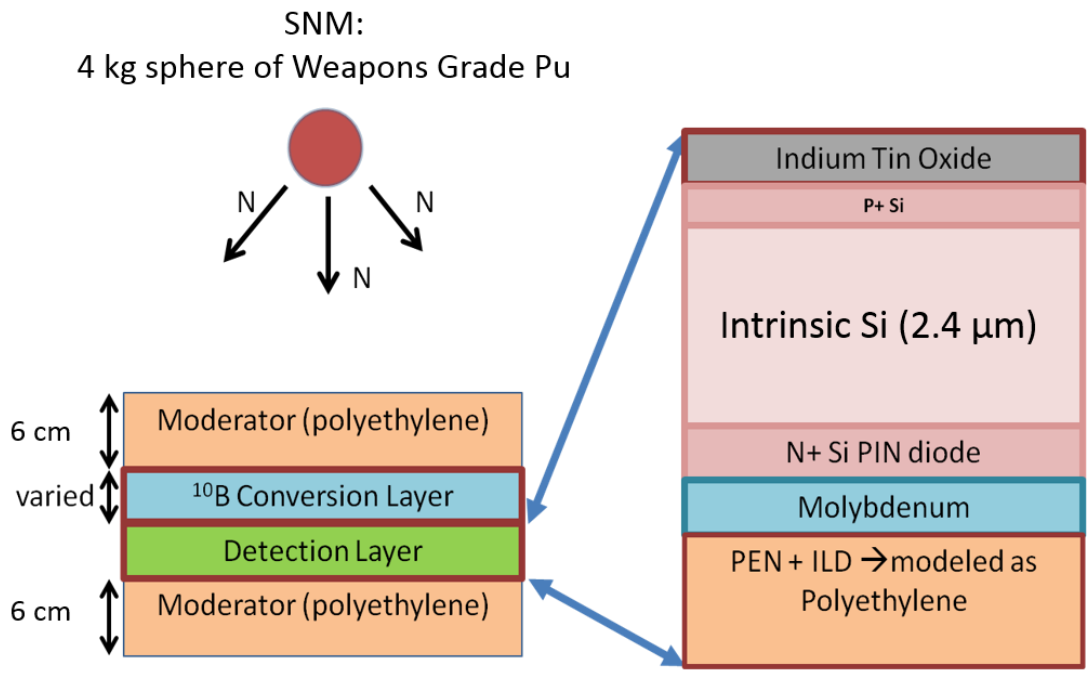

Figure 2.7: Diagram showing example layers for the detection diode. Layers are based off of FDC process technology.

Now taking all of the modeled materials and thicknesses into account, it is possible to further optimize thicknesses to attain a more optimized conversion layer thickness. Since the detector volume, described in Figure 2.5, is void (vacuum), it really represents the ideal case in which thermal neutrons are reflected back to the conversion layer. However, in reality, the detector volume is not void, and many of the thermal neutrons reflected back, have such a low energy, that they are absorbed within the layers associated with the detection diode. This ultimately leads to fewer thermal neutrons striking the conversion

layer. It is also important to note that as the detector volume is no longer void, it is more useful to study the alpha current entering the detection layer -- as opposed to analyzing the averaged flux within the entire detection volume (which was the approach used previously). The new set of simulations for better optimizing conversion layer thickness, taking into account all of the layers discussed in the previous parts, may be seen in Figure 2.8. It is evident from these simulations, that the optimal conversion layer thickness is approximately 2.6 µm. The entire detector as a result has absolute detection efficiency of about 0.6%, and an intrinsic neutron detection efficiency of about 4%. All of these simulations give an idea of how to begin modeling and optimizing a radiation detector. In this case, we optimized a planar neutron detector with a ^{10}B conversion layer and a 2.4 µm PiN diode (using in-house layers). The following section will discuss in more detail how the thickness of the detection diode may be better optimized.

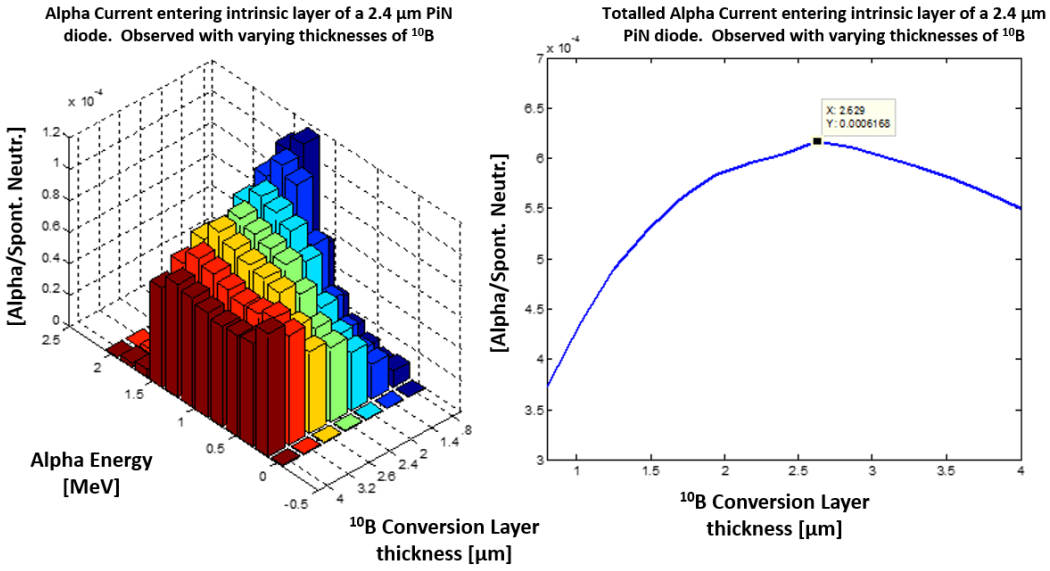

Figure 2.8: (Left) MCNPX simulation results showing the total alpha current entering the 37 cm x 47 cm detection volume. This simulation takes into account all of the layers shown in Figure 2.7. (Right) Plot showing a more precise/optimal conversion layer thickness of 2.6 µm.

2.3 Diode Thickness Optimization

This section discusses in detail the modeling and optimizations conducted using MCNP. This section specifically focuses on choosing optimal diode materials and thicknesses to ensure optimal detection efficiency and proper gamma rejection. The following discussions are primarily taken from already published work in [44].

There are several reports in the literature optimizing the converter layer thickness. McGregor et al. published a definitive work on designing architectures for thin-film coated semiconductor thermal neutron detectors in 2003, however, one aspect of the design which is not considered, is the thickness of the semiconductor diode itself [4]. Many recent reports simulate perforated or textured semiconductor diodes, which are used to enhance neutron detection efficiency [14][15][16].

Single crystal thin films of Si in both silicon-on-insulator (SOI) and free standing forms can be purchased. As discussed previously, using a thinner semiconductor film will reduce interference from gamma interactions. This has been shown using SOI wafers in [17][18]. However, to date there has been no methodical study of the optimum thickness of the semiconductor diode, even for the simplest coplanar arrangements of semiconductor and converter. One exception is the report in [19], which discusses the optimal thickness of both converter and semiconductor for a theoretical LiF:polyacetylene based device. There is also a recently awarded United States patent which describes the optimum thickness of the semiconductor portion of a solid state neutron detector as 10-30 μm, and

although it is not described how this thickness range is derived, it is in excellent agreement with our results presented here [20].

Other than silicon, there are recent reports of additional high quality, single crystal semiconductor films that have been or might conceivably be utilized as thermal neutron detectors. For instance, Almaviva et al. fabricated chemical vapor deposited diamond neutron detectors in the B-doped / intrinsic diamond / Al configuration with an intrinsic layer thickness of 25-100 μm [21]. Kaidashev et al. report ZnO films grown by pulsed-laser deposition on sapphire substrates with a thickness > 1 μm. They achieve a Hall mobility of 100 $cm^2V^{-1}s^{-1}$ with a carrier concentration of only 7.5×10^{15} cm^{-3}[22]. Single-crystal GaAs films with a 2 μm thickness for solar cells have been prepared using epitaxial growth and lift-off in which the growth substrate can be recycled and used for subsequent epitaxial depositions [23]. Finally, epitaxial growth of CdTe with a thickness of 200 μm on a GaAs substrate has also been reported. Although the thickness is quite high, the authors report the film is sensitive to alpha particles [24].

We utilized the publicly available Monte Carlo based computer modeling programs MCNP5 and MCNPX v2.7.0 to simulate neutron, charged particle and photon/electron transport. Our primary tool within these programs was the pulse height tally, which allows easy determination of the energy deposited in a material volume by incident charged particles and photons [25][26]. This allowed us to model both the efficiency of thin film semiconductor neutron detectors, and evaluate the susceptibility of the detectors to background gamma interference. Densities, atomic weights, and isotopic ratios used for simulations, were taken from the 89th edition of CRC Handbook [27].

We first determined the optimal thickness of both converter materials, since this is largely independent of the choice of material or thickness for the diode. Converter layer thickness optimization was conducted through a series of approximately 60 MCNPX simulations for both converter materials, using 5×10^7 particle histories for each converter thickness. We evaluate intrinsic neutron detection efficiency for a normally incident beam of thermal neutrons (0.026 eV), as described by McGregor and Shultis in [28]. Using the pulse tally feature in MCNPX (v2.7.0), it is possible to directly simulate the energy deposited in the detector volume by the alpha, triton, and ^{7}Li ions generated by thermal neutron capture reactions in the converter layer, and thus predict the neutron detection efficiency of different converter/diode arrangements. Analog or explicit capture was used in these simulations, and the neutron capture ion algorithm (NCIA) was used to produce correlated charged particle products from neutron capture reactions. The total number of pulses generated, however, does not represent the true or effective efficiency of such a device, because in practice a lower-level discriminator (LLD) must be implemented to separate actual neutron events from background induced pulses. We evaluated a range of LLD values from 300 to 1800 keV.

We then used the optimal thickness for each converter layer using a 300 keV LLD to study the minimum thickness required for each semiconductor material to collect a certain quantity of energy from either of the charged particle products, i.e. absorb enough energy from the charged particle to produce a "detectable" pulse. In order to accomplish this we ran a series of 610 simulations with MCNPX, with each simulation having an increasing thickness of the semiconductor diode layer for the five different semiconductors and two

converting layers. The reason for choosing the specific LLD setting of 300 keV is to closely follow McGregor's experiments described in [32].

In order to account for the detector gamma rejection capability, we simulated the effect of different diode thicknesses while also varying the gamma ray energy over a broad range. Similar to the optimizations for charged particle detection, these simulations made use of the pulse height tally in order to calculate intrinsic gamma-neutron detection efficiency ($\varepsilon_{int,\gamma n}$). The efficiency $\varepsilon_{int,\gamma n}$ is described using Equation 1 [29]:

$$\varepsilon_{int,\gamma n} = \frac{\text{Number of photons that produce neutron counts}}{\text{Number of photons incident upon the detector}} \quad (1)$$

Ideally, this quantity should be zero – ensuring that no gamma exposure triggers "false-positive" neutron counts. The standard specification for radiation portal monitors, however, requires $\varepsilon_{int,\gamma n} \leq 10^{-6}$. According to specifications laid out by the Pacific Northwest National Laboratory (PNNL), $\varepsilon_{int,\gamma n}$ should be measured with either a ^{192}Ir or ^{60}Co gamma source [29][30]. For our simulations, however, it was beneficial to observe the gamma response over a larger energy range of gamma exposure. For these simulations, a standard LLD setting of 300 keV was chosen.

We also compare the gamma rejection performance of thinner semiconductor layers, down to 3 μm, at two specific gamma ray energies. We chose to evaluate the response of the detector due to 511 keV and 1.46 MeV gammas because these two energies are reported to be the two most frequently encountered gamma-ray energies in an extremely long term gamma background [31].

The resulting intrinsic neutron detection efficiencies predicted for the two converters on 500 μm of Si as a function of thickness and LLD are plotted in Figure 2.9. These results closely agree with calculations performed by McGregor et al., in which similar curves for an LLD of 300 keV are shown [32]. With optimal conversion layer thicknesses chosen for both ^{10}B and ^{6}LiF, it was possible to then model the different diode materials and thicknesses.

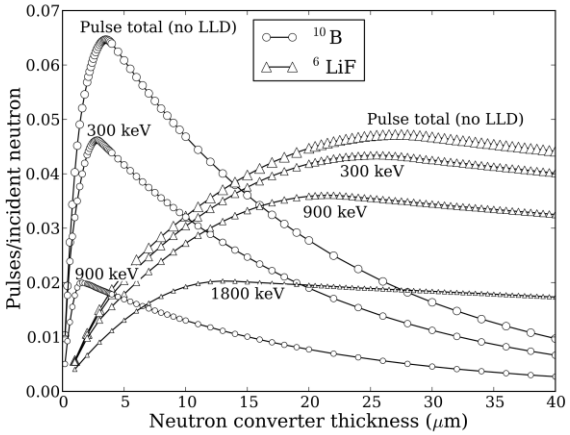

Figure 2.9: Intrinsic thermal neutron detection efficiency for ^{6}LiF and ^{10}B converter films as a function of thickness and LLD. Thickness is shown on the x-axis. LLD is designated by the small numbers near the curves.[1]

It should be noted that no "dead" or contact layer was used in these simulations. Such a layer, usually consisting of ~100 nm of metal and/or heavily doped semiconductor between the converter layer and intrinsic semiconductor, would reduce the energy of the incident charged particles. Consider the charged particle products of a 2.8 μm ^{10}B converter layer. Using MCNPX we find that normally incident alpha and ^{7}Li ions with a kinetic energy of 0.3-1.5 MeV lose on average ~30 and 50 keV, respectively, as they pass

[1] This plot was provided by my colleague John Murphy, a graduate student at UTD. This was a part of our joint research collaboration in our 2012 Applied Physics Letters (APL) publication [44].

through 100 nm of Al. This would reduce the efficiency of the detector from about 4.6% to 4.2% by effectively raising the LLD to ~350 keV. For comparison, a 1 MeV triton will lose only ~10 keV going through 100 nm Al, showing that a ^{6}LiF converter will suffer comparatively less from this effect. We chose not to implement a contact layer for two reasons. First, the choice of contact material will depend on the semiconductor. Second, the geometry of the detector may result in the device having a non-uniform "dead" layer. The neutron detectors demonstrated on SOI wafers [18] did not use the traditional "sandwich" diode structure. Instead they used interdigitated finger contacts where both electrodes are on the same side of the semiconductor layer. In this case, parts of the "dead" layer are made up of the heavily doped Si contacts but other regions of the "dead" layer are composed of 500 nm of protective SiO_2.

Figure 2.10 shows the predicted detector efficiency as a function of thickness for the five selected semiconductor materials with a 2.8 µm ^{10}B and a 26 µm ^{6}LiF converter layer. Each of the curves represents a different LLD setting for each material. As the diode increases in thickness, all of the curves level off at the maximum efficiency for that LLD setting and converter layer. Interestingly, Si and CdTe require almost exactly the same thickness to achieve maximum efficiency, especially for ^{10}B, indicating they have similar stopping power for charged particles despite their large difference in atomic number and bulk density. Diamond requires the least thickness, approximately 50% less than Si to absorb the same amount of energy, ZnO is close to diamond, and GaAs falls in the middle. For instance, it requires approximately 1.3 µm of either Si or CdTe to achieve maximum efficiency for a 300 keV LLD setting and 2.8µm ^{10}B film, while the thicknesses required for diamond, ZnO, and GaAs would be about 0.6, 0.7, and 1.0 µm, respectively.

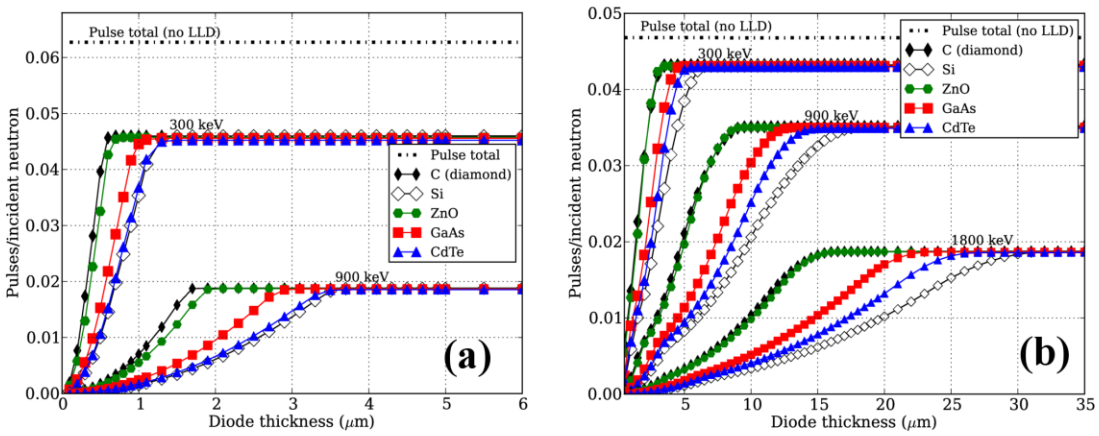

Figure 2.10: Detector efficiency as a function of semiconductor diode thickness; shown to the left is a 2.8 μm ^{10}B converter layer (a), and to the right, a 26 μm ^{6}LiF layer (b).[2]

Results of the simulated intrinsic gamma–neutron detection efficiency, illustrate the maximum allowable diode thicknesses for various materials. This value is found by determining the intersection of the 3D pulse height curve with the $Z=10^{-6}$ plane (see Figure 2.11). The lowest value of diode thickness within this intersection represents the maximum allowable diode thickness for that particular material – according to the $\varepsilon_{int,\gamma n} \leq 10^{-6}$ specification. These results are summarized in Table 2.1.

In general, the added thickness of the ^{6}LiF layer necessitates a lower maximum diode thickness in order to fulfill the $\varepsilon_{int,\gamma n} \leq 10^{-6}$ requirement. This presents an advantage of using ^{10}B over ^{6}Li in a single conversion layer detection approach. This is largely due to the thicker layer of ^{6}LiF enabling more electrons to be generated, as when compared to the detectors with the ^{10}B conversion layer. These electrons are generated primarily due

[2] This plot was provided by my colleague John Murphy, a graduate student at UTD. This was a part of our joint research collaboration in our 2012 Applied Physics Letters (APL) publication [44].

to Compton scattering. The very small change in the CdTe thicknesses originates primarily from the diode material enabling greater amounts of photoelectric absorption due to gamma rays with energies close to the LLD setting.

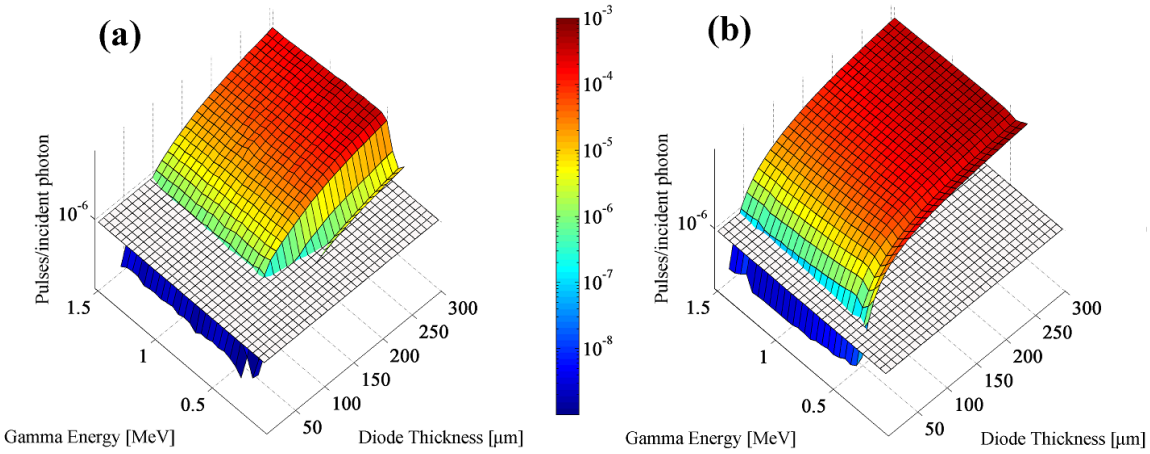

Figure 2.11: Gamma response as a function of diode thickness and incident gamma energy. This shows simulation results for the ^{10}B and Si detector stack (a) and the ^{10}B and CdTe detector stack (b). The LLD for this simulation is 300 keV.

Table 2.1: Maximum allowable diode thickness such that: $\varepsilon_{int,\gamma n} \leq 10^{-6}$ for LLD = 300 keV (Gamma energies:0.3–1.5 MeV).

Diode Material	2.8 μm ^{10}B converter	26.5 μm ^{6}LiF converter
C (diamond)	60 μm	49 μm
Si	86 μm	74 μm
ZnO	36 μm	31 μm
GaAs	38 μm	30 μm
CdTe	28 μm	27 μm

Also observed in the 3D plots in Figure 2.11, is a valley for all diode thicknesses, corresponding to gamma energies around 450 keV. This valley, which can be observed for all five materials, corresponds to the minimum gamma energy required to generate Compton recoil electrons with adequate energy to deposit past the LLD energy bin. The non-zero pulses recorded at lower gamma energies near the LLD bin are due to electrons generated from only photoelectric absorption. The approximate location of this valley can be derived using Equation 2, which Knoll defines for the Compton edge electron energy $E_{e^-}|_{\theta=\pi}$, due to the photon energy hv with a photon scattering angle θ (p. 310-311 from [1]).

$$LLD\ energy \leq E_{e^-}|_{\theta=\pi} = hv\left(\frac{2hv/m_0c^2}{1+2hv/m_0c^2}\right) \quad (2)$$

With the electron rest mass energy m_0c^2 being about 511 keV, and solving for hv with an LLD setting of 300 keV, we determine $hv \geq 464.9$ keV. This value corresponds very closely to the gamma energy value observed in the valleys in the simulated 3D surface plots.

Intrinsic gamma detection efficiencies corresponding to the specific gamma energies and diode thicknesses are reported in Table 2.2. It is clear from these results, that Si provides better gamma rejection as compared to the other four materials. However, it is also clear that when considering all five materials with diode thicknesses less than about 30 µm, there is a rapid decrease in gamma detection efficiencies, such that for thicknesses of <10 µm, the response is so low that it is nearly zero. Here it should also be noted that for diode thicknesses of ≤10 µm, it is difficult to attain non-zero tallies past the LLD

energy bin. Even while running 1×10^9 particle histories along with the forced collision variance reduction technique, tallies of only very small values were recorded. The very high gamma rejection rates are a strong motivation for developing thin-film diode charged particle detectors.

Table 2.2: Intrinsic gamma efficiencies for selected gamma energies and diode thicknesses (LLD = 300 keV and a 2.8 μm ^{10}B conversion layer).

Thickness (μm)	*γ energy (keV)*	*C (diamond)*	*Si*	*ZnO*	*GaAs*	*CdTe*
3	511	0	0	0	0	0
	1460	0	0	8×10^{-14}	0	9×10^{-14}
10	511	0	0	1×10^{-12}	0	6×10^{-13}
	1460	3×10^{-13}	1×10^{-13}	8×10^{-12}	2×10^{-12}	9×10^{-12}
30	511	4×10^{-9}	6×10^{-11}	3×10^{-7}	1×10^{-7}	6×10^{-7}
	1460	1×10^{-8}	1×10^{-10}	2×10^{-7}	6×10^{-8}	2×10^{-7}
100	511	1×10^{-5}	3×10^{-6}	2×10^{-4}	2×10^{-4}	4×10^{-4}
	1460	1×10^{-5}	2×10^{-6}	9×10^{-5}	6×10^{-5}	1×10^{-4}
300	511	7×10^{-4}	3×10^{-4}	2×10^{-3}	2×10^{-3}	4×10^{-3}
	1460	4×10^{-4}	2×10^{-4}	2×10^{-3}	2×10^{-3}	3×10^{-3}

From these simulations, we have provided a range of diode thicknesses and materials from which to design an optimal neutron detector based on a single planar conversion layer. Diamond and ZnO render the greatest stopping power for charged particles, typically requiring only half the thickness of Si to achieve maximum intrinsic thermal neutron detection efficiency. We find that Si possesses the best gamma rejection capability for a given thickness, even greater than that of diamond; this is not surprising given that diamond has the highest atomic density of any material and actually has a greater

electron density than silicon [34]. However, for thicknesses of ≤10 μm, all of the materials are essentially gamma "blind" with an LLD setting of 300 keV or greater.

2.4 Back Plane Array Modeling[3]

This section briefly discusses the system modeling work concerning the back end circuitry in the detection array. The current model in particular, was programmed by Daniel Pressler, using both MATLAB and HSPICE to accurately reproduce the response of an array of active pixel sensors (see Chapter 3 for the discussion of APS). This model accounts for the impact of process variations in both a-Si:H and InGaZnO thin film transistor (TFT) processes. Specifically, these variations were primarily based off of measured mobility and threshold voltage variability on existing FDC runs. It was possible to model these measured data by fitting them with bivariate normal distributions in MATLAB (see Figure 2.12) [35].

By using an algorithm in MATLAB, Daniel Pressler was able to make multiple calls to a circuit simulator (HSPICE) and then assign arrayed, TFT-based, active pixel sensors varying mobility and threshold voltage values -- based on the modeled distributions derived in MATLAB. The results of these simulations (Figure 2.12) provided a distribution of pixel transconductance gains and pixel offset (denoted as output current immediately following reset). This distribution was then fit to a Gaussian Mixture Bivariate Normal Distribution in MATLAB, and then used to generate an array of active pixel sensors in line with the measured process variations [35].

[3] Daniel Pressler, an undergraduate in Dr. Allee's research group, was in charge of developing the active pixel sensor array model. All of the up-to-date detection-array circuitry modeling (briefly described here in this section), was completed by Daniel, and can be studied further in his Honor's Design Thesis [35].

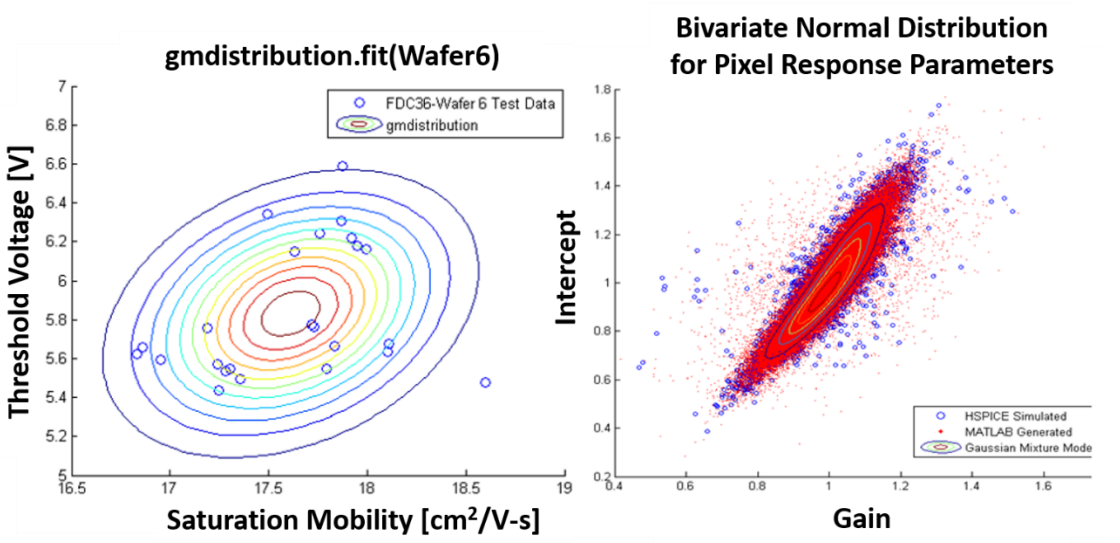

Figure 2.12: (Left) Measured threshold voltage and saturation mobility distributions for an FDC36-Wafer (InGaZnO TFTs). The corresponding fit bivariate distribution is pictured here as well. (Right) Simulated pixel transconductance and pixel intercepts (offsets) distribution. The corresponding fit Gaussian Mixture Bivariate Normal Distribution is pictured here as well Images borrowed from [36]

Finally, it was possible to simulate this generated array, and observe pixel output currents under normal operation. When alpha particle strikes were simulated on the array, however, it soon became clear that manufacturing variations dominated pixel-to-pixel current variations. This discrepancy can be remedied by using correlated double sampling (CDS) in which the output column currents for each pixel during a known state (i.e., no alpha particles present) are stored, and then subtracted from the respective output currents in an unknown state. The effectiveness and requirement of CDS are illustrated below in Figure 2.13.

In summary, this model effectively takes into account manufacturing variations for an active pixel sensor-based array, and especially proves the necessity of using a post-processing technique such as CDS to distinguish positive detections effectively. More

importantly, this model provides an excellent starting point from which to test and simulate other future arrayed detector designs.

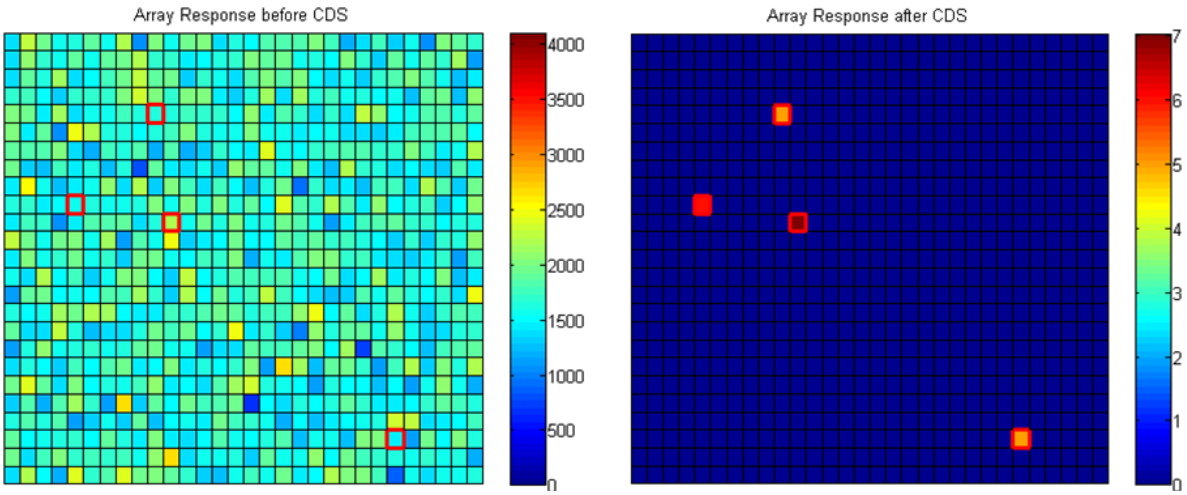

Figure 2.13: Pixel output currents before and after correlated double sampling (CDS) is applied. The squares highlighted in red represent pixels that have been struck by alpha particles. Image borrowed from [35].

3. EARLY SENSING CIRCUITRY DESIGN/IMPLEMENTATION

This chapter outlines the earlier sensing circuitry designs of this research. The sensing circuitry is primarily responsible for detecting and reading out the small amounts of radiation-induced charge generated at the output of the detection diode. In general, the sensing circuitry collects the small amount of charge from the detection diode on to a sensitive node. The charge on this sensitive node is then amplified to a measurable level, using low-input referred noise circuitry.

3.1 Single and Dual stage Active Pixel sensor (APS)

Arrayed pixel sensors have been conventionally, implemented as passive pixel sensors (PPS), in which each pixel contains a sensing diode, of which the output is directly read out through a select switch as seen in Figure 3.1(a). Very similar to the dense layout of dynamic random access memory (DRAM), this structure provides a simple compact means of imaging light or other types of radiation. However, without any kind of pixel amplification, the PPS design must rely heavily on low-noise external amplification to resolve the small amounts of charge detected by each pixel's diode.

With the intent of eliminating the need for this external amplification, and further reducing noise, efforts have been made to develop active pixel sensors (APS) which enable low-noise in-pixel amplification. One such design presented in [36] uses a single source follower stage (see Figure 3.1(b)) to convert the detection diode's small ΔV at the sensitive node, to a change in current at the column output.

However, in order to further optimize noise performance, it is possible to increase the signal transconductance gain by adding a common source stage to the in-pixel amplifier

as presented by Lee and Kunnen in [36]. This is the architecture (Figure 3.1(c)) discussed, and initially chosen for the active pixel sensor readout in the beginning of this research. The key design improvement of the dual-stage architecture, allows one stage to be optimized for low flicker noise, while the other is optimized for high transconductance gain [36].

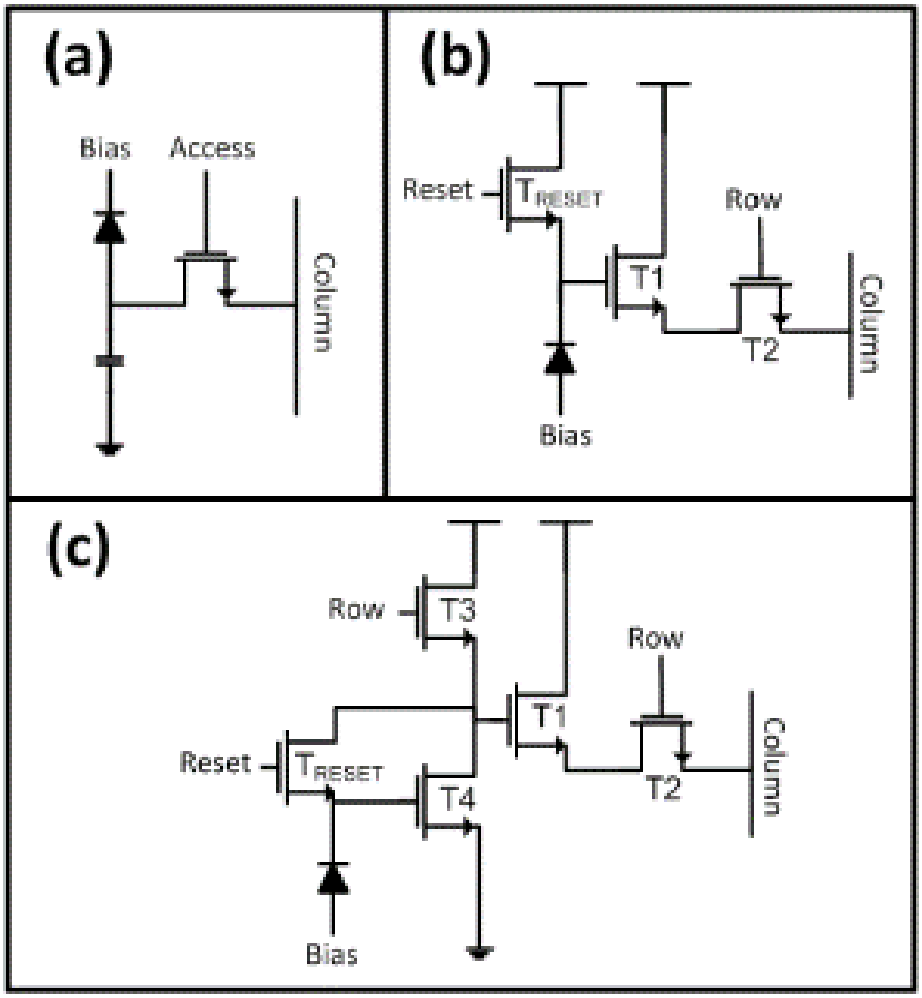

Figure 3.1: (a) Passive Pixel Sensor Architecture as presented in [14]. (b) Single stage active pixel architecture presented in [38]. (c) Dual stage active pixel sensor as presented here and in [36].

This dual stage APS design implements n-type TFTs from either an a-Si:H or InGaZnO FDC process. Any incident charged radiation, or light, on the reverse-biased PiN diode will generate a small change in charge at the cathode. While the Reset transistor is off, the cathode is attached to a floating, high-impedance node (referred to as the "sensitive node"). The change in charge, is seen as a change in voltage at the sensitive, node, and is amplified through the low noise 2-stage amplification circuitry. The resulting column output will see a change in measured current due to the incident radiation on the diode. One should note as well, that the biasing of the common source stage (T3 and T4) can be stabilized in the "high-gain" region by connecting the drain of the Reset transistor to the drain of the common source amplifier transistor (this design is denoted as the Auto-Zero design as later seen in Figure 3.2). More detailed documentation concerning the operation and measurements of this circuit may be examined further in [36].

In experimental tests, the dual stage APS was used in the "Auto-Zero" configuration. The diode used for alpha measurements, was an externally connected commercial PiN diode (OPF480) with a capacitance of about 1.5 pF. Here we assume that the PiN diode capacitance dominates the total capacitance at the sensitive node -- namely $C_{pix} \approx 1.5$ pF. If one assumes that a 5.307 MeV alpha particle strikes the diode (the maximum we could expect from a ^{210}Po alpha test source), and dissipates all of its energy generating electron-hole pairs (assuming 3.6 eV/e-h pair in Si) we may perform the following calculations to attain the approximate change in voltage at the sensitive node due to one alpha strike.

$$\Delta q_{pix} = 1.6 * 10^{-19} \left[\frac{C}{electron}\right] * \frac{5.307\ [MeV]}{3.6\ \left[\frac{eV}{e-h\ pair}\right]} \cong \mathbf{2.4} * 10^{-13}\ [C]$$

$$\cong \mathbf{1.5} * \mathbf{10^6}\ \text{e} - \text{h pairs}$$

$$\Delta V_{sense} = \frac{\Delta q_{pix}}{C_{pix}} = \frac{\mathbf{2.4} * 10^{-13}\ [C]}{1.5\ [\text{pF}]} \cong \mathbf{0.16}\ [\mathbf{V}]$$

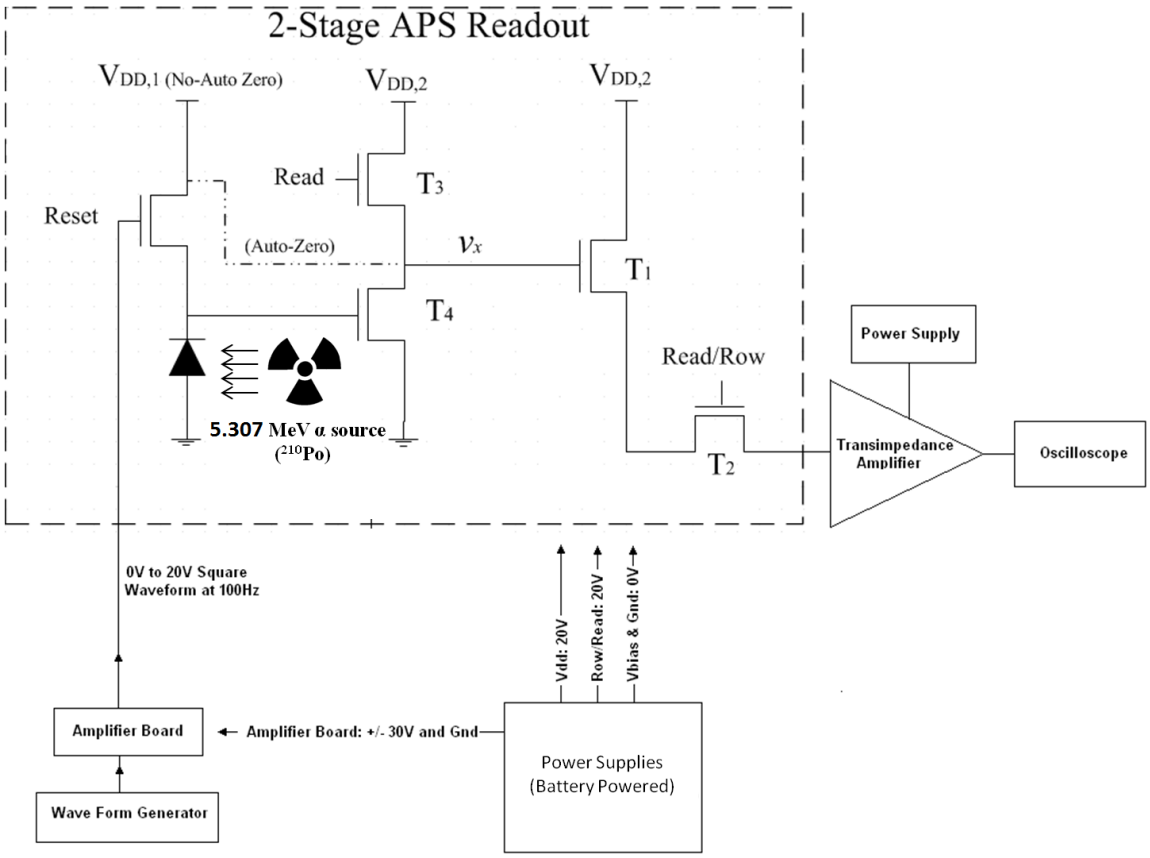

Figure 3.2: Dual stage active pixel sensor, showing experimental setup for alpha particle measurement.

With an APS transconductance gain of approximately 3 μA/V as reported in [36], the expected change in column current at the output will be approximately 480 nA. The entire experimental setup (seen in Figure 3.3) included a battery-driven waveform generator (using an LM55 IC) along with battery-driven supply voltages. All critical components were shielded within a grounded metal box to further reduce the effects of external noise sources. Finally, the column output of the APS was fed into a low-noise transimpedance amplifier to convert the output current to a voltage --enabling measurement with an oscilloscope.

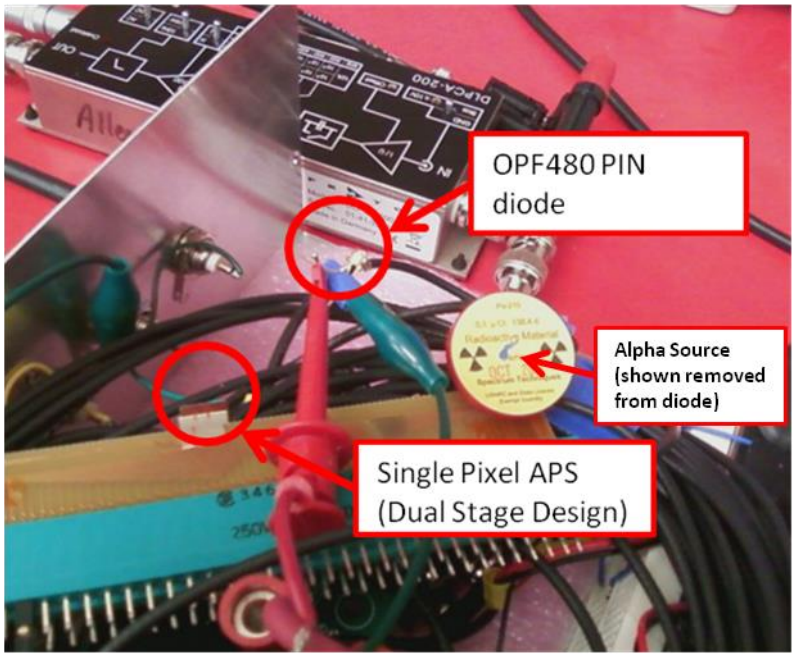

Figure 3.3: Experimental setup used for measuring alpha response of the OPF480 PiN diode using the dual stage APS design.

Finally, the experimental measurements showing successful alpha detection may be seen in Figure 3.4. In this figure two small steps in the output waveform (magenta) are

observed. These correspond to two detected alpha particle strikes. It should be noted here, that considerable effort in creating a low noise experimental setup was needed in order to finally observe an alpha response at the output. This alone suggests the possible need for greater signal gain in the pre-existing APS design.

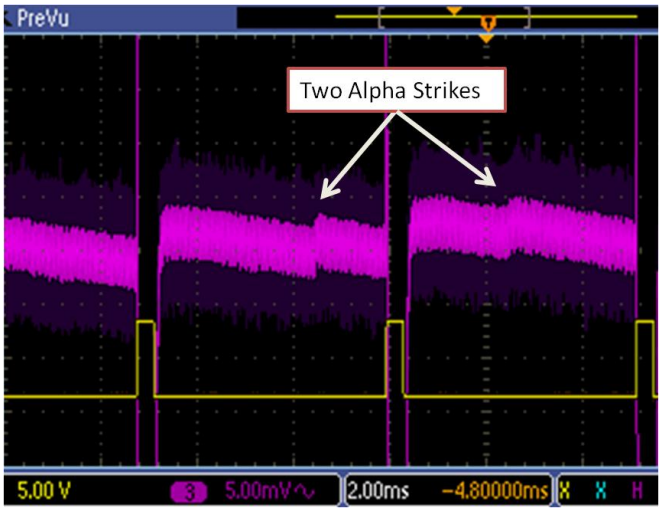

Figure 3.4: Magenta waveform showing two detected alpha strikes at the column output (transimpedance amplifier gain was set to 10^5 V/A). The yellow waveform is the Reset signal

According to the experimental results, an alpha-induced change of approximately **20-50 nA** can be observed at the column output of the single pixel. This is a much smaller number than the expected 480 nA as described in previous calculations. Factors contributing to this small measured change in current are likely due to the following issues:

- Higher than expected capacitance at the sensitive node -- possibly due to external diode interconnect parasitics

- Most likely the gain of the of the CS stage was less than its nominal value due to the reset biasing point on the sensitive node. This would have decreased the overall pixel transconductance gain. Variations in this biasing point can easily have been caused by process variations and shifts in the threshold voltage.

The first issue emphasizes the fact, that from a circuit design perspective, the effective capacitance at the high-impedance sensitive node must be kept as low as possible, while still enabling a large-surface area diode. Consequently, parasitic capacitances (especially interconnect parasitics) at the sensitive node must be reduced as much as possible. Interconnect parasitics can certainly be further mitigated by integrating diodes with each amplifier. One may also deduce that the detection diodes themselves must possess low capacitance per area, be thick enough to absorb all radiation, and efficiently convert energy deposited into electron hole pairs.

3.2 Charge Sensitive Preamplifier (CSP)

A more conventional means of detecting charged particles uses a charge sensitive preamplifier (CSP). Such an amplifier (see Figure 3.5) relies on the large gain of an operational amplifier to provide a virtual ground via a small feedback capacitor (C_F). The small Δq or Q_i of the reversed-biased detection diode, during an ionizing event, is stored on the small feedback capacitor of the op-amp. The output of the op-amp is then essentially equal to Q_i / C_F. Thus, it is optimal to incorporate a very small feedback capacitance to ensure a large response to a small value of Q_i. The addition of a forward biased JFET (as seen in Figure 3.5) eventually allows the charge on C_F to leak through the gate-source junction of the JFET. This enables the preamplifier to "reset" after an ionizing event

occurs. More importantly, however, the JFET also acts as a low-noise circuit element from which the input can be initially amplified.

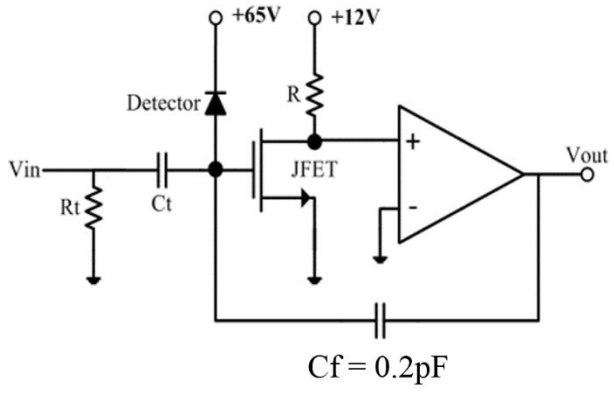

Figure 3.5: Basic schematic of the charge preamplifier. Pictured is the detection diode wired to a JFET and feedback capacitor. The JFET is slightly forward biased, and is connected through its drain to the input of an operational amplifier. Image redrawn from [6].

The low-noise design used for this research was initially presented by Bertuccio et al. in [40] and implemented as an X-ray detector by Ramirez et al. in [6]. This design utilizes a low-noise amplifier based on an N-channel JFET and bipolar junction transistors (BJTs). The design (seen in Figure 3.6), implements a cascoded voltage amplifier stage: consisting of the N-channel JFET (**J2**), a PNP BJT (**Q7**), and a resistor (**R5**). The following second stage implements an emitter follower with an NPN BJT (**Q8**), and also forms a secondary negative feedback loop between the emitter of **Q8** and the base of **Q7**. According to Bertuccio et al., the combination of this secondary feedback loop and resistors (seen as **R4**, **R3**, and **R2** in Figure 3.6), enables a higher dynamic range for the DC input voltage [40]. Finally, the output stage consists of another emitter follower (formed by **Q9**), which allows the amplifier to have a lower output impedance. All of the other

pictured components in Figure 3.6, apply primarily to the proper DC biasing of the amplifier.

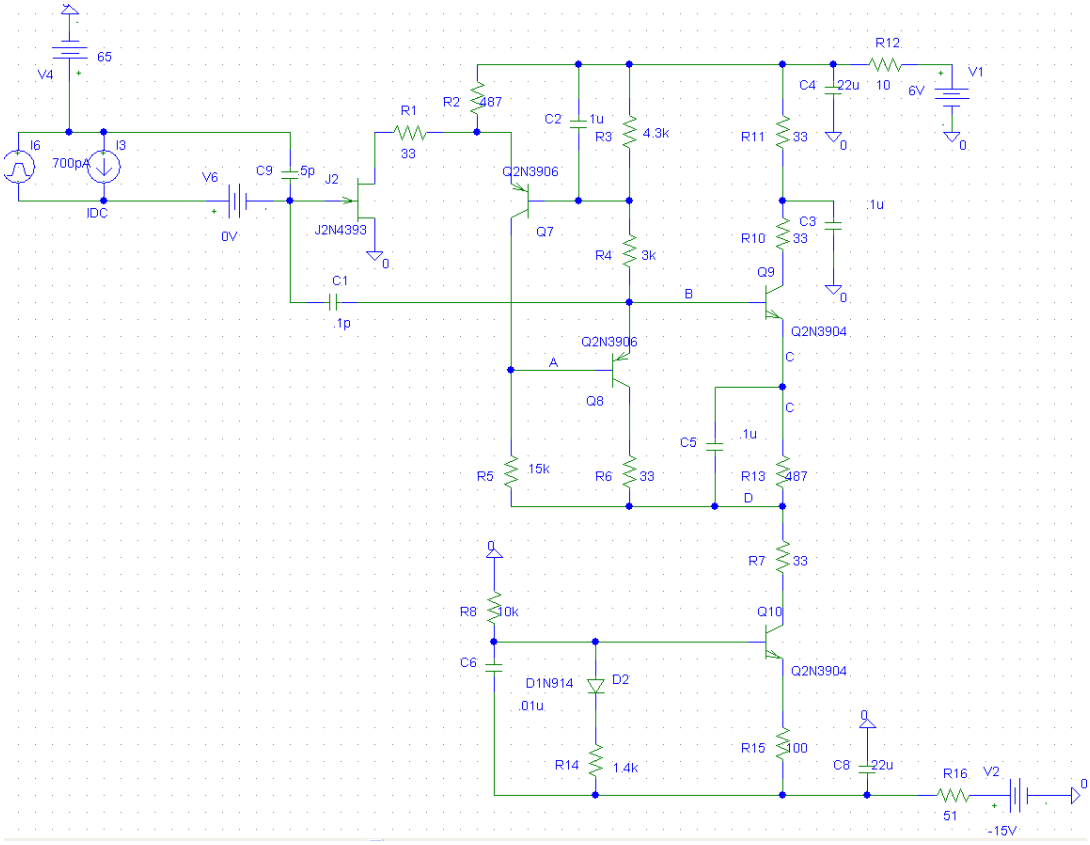

Figure 3.6: Full schematic of the charge sensitive amplifier used in this research. This architecture was adopted from [6][40], built with COTS components on PCB, and implemented as an alpha particle detector.

The CSP was built using commercial-off-the-shelf (COTS) components soldered on to a printed circuit board (PCB). As in the previous section, a commercial OPF480 PiN diode was again used as a detection diode. The entire setup was connected within a shielded metal box, to help negate external noise sources (see Figure 3.7). Experimental measurements with an alpha source revealed pulses at the output with heights ranging from 1 to 1.2 V. With a feedback capacitance of 0.2 pF, this closely corresponds to the

total charge collected at the input due to one 5.307 MeV alpha strike – roughly 1,470,000 electron-hole pairs.

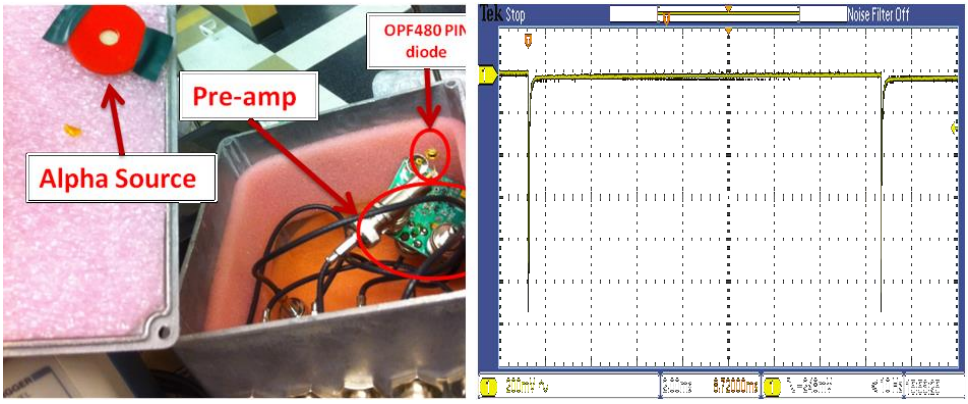

Figure 3.7: (Left) Alpha response experimental setup, displaying home-made charge sensitive preamplifier. (Right) Response of the charge sensitive preamplifier showing two distinct alpha strikes at the output.

It is clear from these measurements that the CSP is much more effective at amplifying the small amounts of charge at the sensitive node when compared to the dual stage APS. Since the CSP utilizes a virtual ground at the input by means of its large gain, any effect of parasitic capacitance at the input has far less impact on the output when compared to that of the APS architecture. Unfortunately, however, it is difficult to implement this CSP as an in-pixel amplifier (as one is able to do with the APS design). Furthermore, it is currently only feasible to implement N-type TFTs with a-Si:H or IGZO processes – therefore high-gain operational amplifiers are difficult to design without P-type TFTs. Thus, the use of a CSP in an arrayed detector would more likely be as an external amplification component , while the detection array itself, for example, could consist of passive pixel sensors which would then feed into their respective CSPs at the periphery.

4. MULTI-STAGE CHARGE SENSITIVE APS

As stated before, the primary issue with implementing APS's in thin film technology is that in general, only one carrier type of FET is available (either N or P). Thus, without the use of complementary-type devices to serve as active loads, resulting amplifier gains are fairly low. This is especially true of the designs presented in [36][38][39]. Although these designs exhibit low input referred noise, their low signal gain translates to a very small alpha induced signal at the output. An experiment showing this small alpha response is later shown in Fig. 5(a). Since this sensor will ultimately be deployed in noisy environments, it is critical for the signal at the output to be large enough to ensure proper hit detection. The active pixel sensors presented here solve this particular issue, and initial experiments (see Figure 4.4) with alpha radiation verify the benefits of this new design.

4.1 Multi-stage APS Design Overview

The next section will present the multi-stage charge sensitive APS design, and will give an overview of basic operation and characteristics. The following section will then discuss the advantages of this new APS design pertaining to the detection of discrete ionizing particles within a large-area, TFT-based, sensing array. The majority of this section has been previously presented in [45].

4.1.1 Design Description

The new multi-stage APS design implemented here consists of an integrated PiN diode and multiple cascaded common source amplification stages. Aside from the PiN diode, the devices in this circuitry consist only of N-type thin film transistors (TFTs) fabricated in either aSi:H or InGaZnO processes. The details of the TFT fabrication process used for these designs, along with TFT device characteristics, may be found in [41][42][43]. For this chapter, simulation and experimental results are based off of designs fabricated using InGaZnO TFTs.

Referring to Figure 4.1(c), the cathode of the integrated PiN diode is connected to the gate input of the first common source amplifier stage (T1). This sensitive node is self-biased in the DC regime via two diode-connected TFTs in series (T2 and T3). Following a change in voltage at the sensitive node (consistent with an alpha strike, for example) the self-biasing enables the sensitive node to slowly "reset" itself to the high-gain DC operating point. A large gate-length TFT (T4) with drain shorted to gate, serves as the CS amplifier load. The output of the CS stage is then connected via an AC coupling capacitor to the input of the next CS amplification stage – which is simply a copy of the first stage. The AC coupling capacitor permits the input of the subsequent stage to have the correct DC bias, while still passing the high frequency pulse we would expect from an almost instantaneous change in charge at the sensitive node (due to an alpha strike for instance). All of the subsequent CS stages (which are simply repeated versions of the first stage) are self-biased in the same manner as described with the first stage.

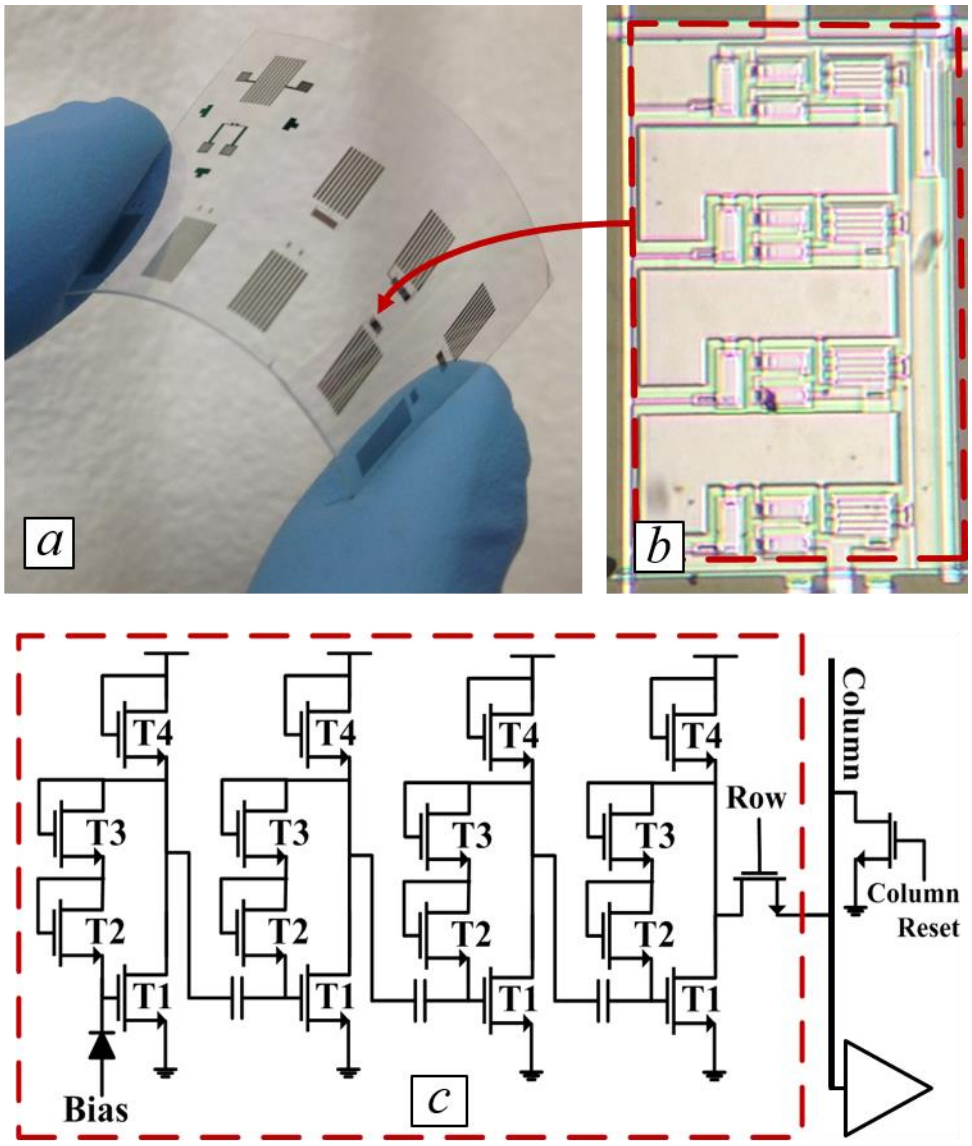

Figure 4.1: (a) Optical photograph of individual TFT APS test structures. Also illustrated, is the flexibility of the polyethylene napthalate (PEN) plastic substrate. (b) Microscopic photograph of the 570 x 1060µm 4-stage APS measured in this work. (c) Single APS schematic portraying the four cascaded CS amplification stages.

As only N-type devices can be used in the design, each CS stage usually provides gains ranging from 1.5-3V/V. Modeling realistic diode leakage, the gain at the first amplification stage will be slightly reduced from the nominal gain setting. Nevertheless, after cascading multiple stages, the total gain from input to output increases exponentially

with each stage. For example, in the case of cascading four CS stages, we expect to see gains ranging from 20-30V/V. Any number of stages can be cascaded, provided the output pulse does not get too large and begin to take transistors out of saturation. Furthermore, since large-area is a requirement for this detector, the larger pixel sizes due to these additional amplification stages, is not detrimental to the overall application. For the purposes of this manuscript, the 4-stage design was chosen as a realistic example for simulations and experimental measurements.

The output of the final CS stage can be directly fed into the array column output, via a row access transistor (as seen in Figure 4.1). Thus, during array readout, all of the columns of only one row are read out at a time. This means, that following a read, each column must be reset to a lower voltage (typically 0V) before the next row is accessed. The circuitry to implement this is pictured on the periphery of the APS schematic in Figure 4.1. This prevents any previous voltage on the column output from affecting the operation of the pixels in the next row. This type of approach would be necessary if the output is read out in voltage mode. Thus, it follows that the outputs of each column would then be separately read out by externally connected unity gain buffers, and then measured using off-chip analog to digital converters.

Another read out approach is to measure the APS output in current mode. In this case, the last CS stage of each APS would feed into a source follower stage, the output of which then feeds via a row access transistor to the column output. In the case of reading the column outputs out in current mode, each column would simply be connected to the vir-

tual ground of an externally connected current integrator. In this case resetting the column after each row access would not be necessary; however, the addition of the source follower would further increase power consumption of the entire array.

4.1.2 Design Advantages

Previous TFT-based APS implementations as presented in [36][38][39], detect an event by sensing a level-change in the output during pixel read out. Specifically, this level-change is determined by comparing the current and previously read output value of a particular pixel. This scheme works very well for detecting light, however, for the purposes of detecting small discrete signals (such as an alpha strike), this becomes impractical. An example alpha strike using such a design is later introduced in Figure 6.2(a). Using this scheme, we would immediately lose information pertaining to time of arrival and number of events occurring on a pixel. Furthermore, implementation of a large array, subsequently leads to a long delay from when a discrete event might be detected on a pixel – to when that particular pixel is actually read out. This long delay will cause the "high-gain" DC biasing point of each APS to leak off – further reducing the already small gain of each pixel. Even worse, since this detector is expected to be fielded in noisy environments, the small APS gains and the resulting small level changes at the output, cause the overall output signal to be more susceptible to corruption by external noise sources – potentially leading to "false-positive" detections, or even worse: missed detections.

Therefore, for the purposes of detecting discrete ionizing particles, the new multi-staged APS design described here presents a more specialized and robust solution. In

addition to achieving higher gains by using more amplification stages, this new APS will continually be biased in a "high-gain" state. Thus each pixel is always sensing, and does not require a sensitive input node to be continually reset as in [36][38][39]. Moreover, the pulse resulting from a positive detection is elongated in time due to the small self-biasing currents (as seen in Figure 4.2 and Figure 4.4(b)). Therefore, given a detected pulse and its long "tail" at the output, it is possible to sample the pulse multiple times at a low duty cycle – essentially allowing other pixel outputs to be sampled at the same time. This ensures that information concerning both time of arrival and number of detection events is also preserved.

4.2 Simulations

A series of simulations was conducted in order to simulate the functionality of the APS. BSIM3 model parameters extracted to match our InGaZnO TFT I-V data, were used for SPICE level simulations. In addition to checking for proper circuit functionality, it became very important to analyze the output characteristics of the APS during transient operation. This is especially important for realizing the specifications for the integrated detection diode.

4.2.1 Simulation of the Alpha Response

In transient simulations, the detection diode was simply modeled as a capacitance connected in parallel with a DC current source. In this case, the capacitance models the junction capacitance of the detection diode, and the DC current models the reverse-bias leakage (dark current). In order to model an alpha strike, an additional pulsed current source was connected in parallel with the diode model. The short duration and amplitude

of the pulse correspond to the total estimated charge collected on the sensitive node due to a high energy alpha particle. In these simulations, it was assumed that such an alpha strike would deposit roughly 0.5 MeV of energy in the diode, yielding approximately 22fC of charge on the sensitive node (assuming a Si diode). This simple diode model was then simulated in the time domain along with the rest of the APS design. An example simulated output pulse is shown in Figure 4.2.

Two qualities of the alpha-induced pulse are important for the operation of this detector: pulse length and pulse amplitude. It is clear that pulse amplitude at the output needs to be as large as possible in order to more easily distinguish pulses above the noise floor. In terms of pulse-length, it is optimal for the pulse to last as long as possible. As multiple pixel-rows share one output column, it is necessary to assert each row's access transistor at a very low duty-cycle. Thus, when a single pixel produces a pulse, the measured output at the column is a sampled version of that pulse. In order to then maintain large arrays, and still "catch" detection events on individual pixels, it is necessary to ensure each APS produces long pulse widths during such a detection event. Otherwise with short output pulses, the array must be smaller in order to support the same row-sampling clock frequency. In simulations, the pulse-measurement of Full Width at Half Maximum (FWHM) was used as a gauge of the pulse length. Additionally, the amplitude of the simulated (continuous) pulse was recorded and divided in half, as a good measure of a realistic sampled amplitude (refer to Figure 4.2 as an example).

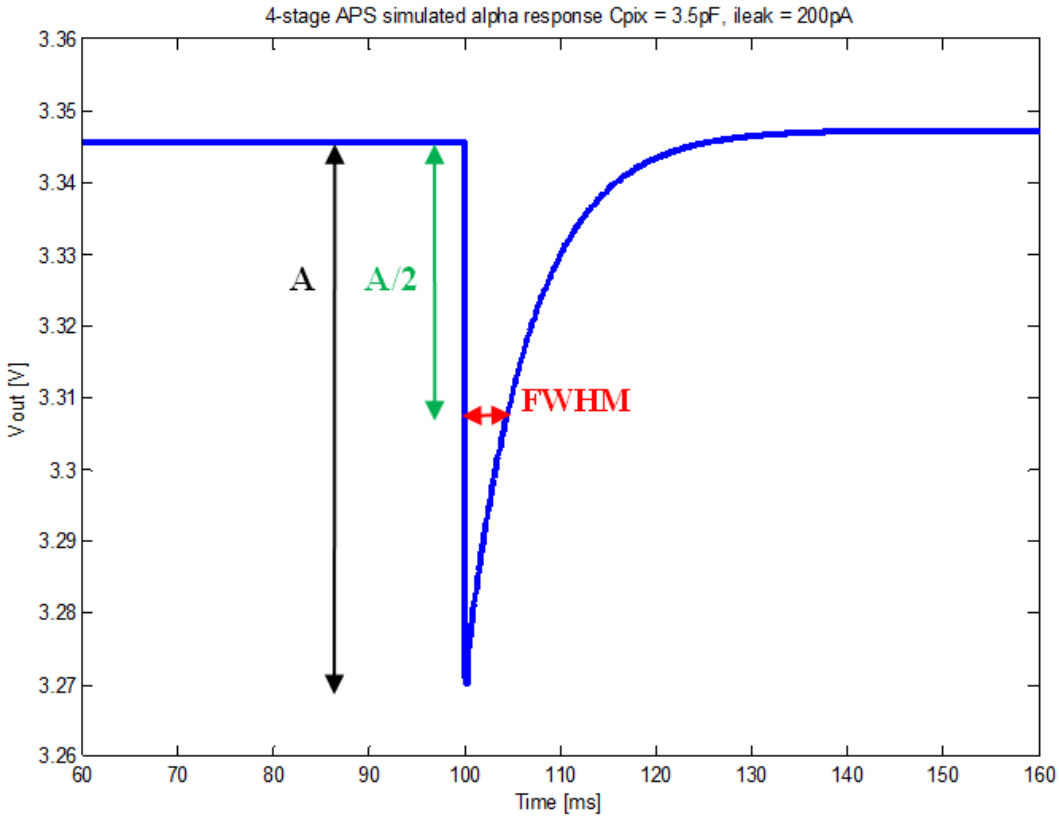

Figure 4.2: Simulated output pulse from 22fC of input charge for the 4-stage APS shown in Figure 4.1. This figure highlights the pulse measurements (FWHM and half-amplitude) which were recorded, and later used to analyze detection diode requirements and array scalability.

4.3 Experimental Measurements

After fabrication of single pixel test structures using InGaZnO TFTs, the 4-stage APS (seen in Figure 4.1) was specifically tested in order to establish a rough overall gain estimate. This was done by asserting a known voltage step (using a signal generator) at the input of the pixel and then subsequently measuring the output pulse as seen in Figure 4.3.

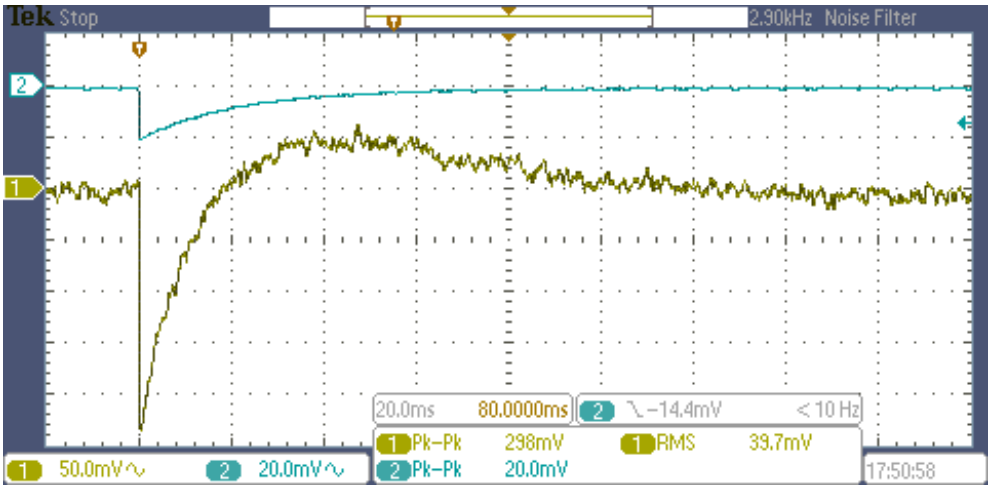

Figure 4.3: Characterization curve of 4-stage APS (fabricated with InGaZnO TFTs). The blue waveform is an ideal input step fed into the pixel via a standard waveform generator. The yellow waveform is the resulting measured pixel output pulse

Gains of the 4-stage design were measured to be about 20V/V fairly close to what was modeled in the simulations. From these initial experiments, it was determined that process variations might easily shift the biasing point of the self-biased CS stages, and thereby decrease each stage's gain. In future implementations, this problem can be resolved simply by implementing a global external voltage bias to each CS stage -- ultimately allowing better control of the overall pixel gain. Nevertheless, even without these improvements, the advantages of this new design are apparent.

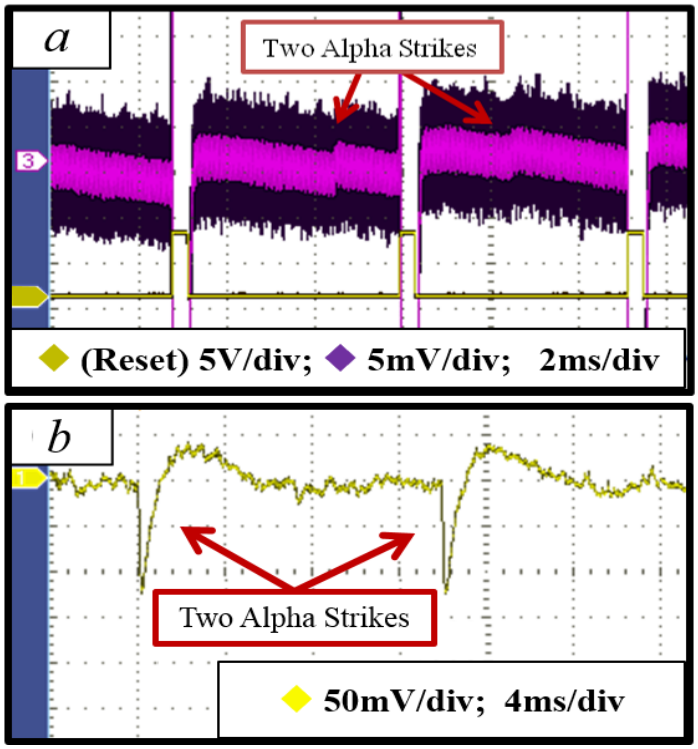

Figure 4.4: Plot (a) depicts the measured alpha response detected with an a-Si:H based dual-stage APS design presented in [36] and [39]. In comparison, (b) depicts the alpha-induced pulses measured at the output of a newly developed 4-stage APS (using InGaZnO TFTs). Note how, in addition to having a weaker signal, the APS in (a), needs to be constantly reset, while the APS from (b) inherently settles back to a "high-gain" state after a detected event occurs. In both experiments, the same Si PiN diode was attached externally as a detection diode, and the same ^{210}Po alpha source was used.

Further experimental measurements tested the alpha response of a single 4-stage APS (Figure 4.4). At the time of this particular investigation, no integrated detection diode was yet developed for the new APS designs. Thus, for testing purposes, the sensing diode used was an externally connected, commercially available Si PiN diode (OPF480). The diode was irradiated with a ^{210}Po alpha source -- which emits ~5 MeV alpha particles. The results of these measurements were also compared to those of a similar experiment in which the dual stage APS presented in [36] and [39] was also irradiated with the same source, while using the same sensing diode. It should be noted that in order to attain the

small alpha response shown in Figure 4.4(a), a low noise setup was very critical. For example, extensive shielding and batteries were needed for the entire setup in order to decrease the effects of external noise sources [39]. In contrast, the results shown in Figure 4.4(b) were attained using a standard power supply, with a minimally shielded setup. Setup aside, strong alpha induced pulses with amplitudes ranging past +100 mV (well above the noise floor), could still be observed at the pixel column output (see Figure 4.4(b)). Compared to the alpha response of the older dual-stage design, it is clear that this implementation provides a much more robust means of detecting individual charged particles – a critical requirement for a "conversion-layer" based neutron detector.

4.4 Conclusion

Simulations of the new single pixel show both the functionality of the new design and lay the ground work for the development of large arrays, given a set of characteristics for the integrated detection diode. Initial experiments characterizing the gain of this new APS design helped determine future improvements that should allow higher gain operation. Improvements aside, alpha response experimental results still illustrate the advantages of this design in comparison to other TFT-based APS designs previously presented in literature.

5. MULTISTAGE APS DESIGN IMPROVEMENTS

5.1 Gain improvement with external bias control

In the first multistage APS design (described in the previous chapter), the self-biasing transistors of each CS stage rely heavily on the TFT threshold voltage. Unfortunately, with process variations, and the resulting shift of threshold voltage levels, each stage's high-gain biasing point will vary as a result. For this reason, an extra biasing port for the APS was added in order to allow better external control over the pixel gain (see Figure 5.1). The increased control over gain, means it is also possible to attain similar gains with less stages. For this reason, designs with varying numbers of stages were implemented as well.

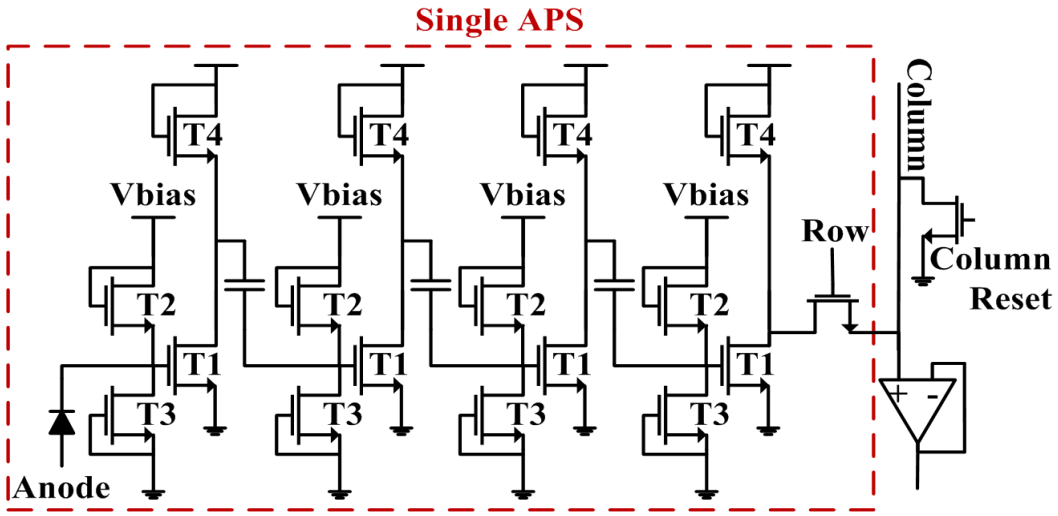

Figure 5.1: Schematic of the improved 4-stage APS design. Note the extra port for controlling the DC bias of each stage.

5.2 Simulations: Pixel Response and Power Consumption

Similar to the SPICE simulations described in the previous chapter, it was possible to model a 0.5 MeV alpha strike at the input of each multi-stage APS variant. The resulting response is highlighted in Figure 5.2. A 0.5 MeV alpha strike was chosen because it represented a plausible energy-deposition level from an incident alpha particle resulting from a neutron capture reaction in ^{10}B. As expected, we observe increasing pixel gain as more stages are added. In this case, the gain of each stage is modeled to be approximately 2.5 V/V for this particular biasing point. For the case described, total pixel gains of 7.6 V/V, 19.7 V/V, 48.8 V/V, and 134.4 V/V for the 2, 3, 4, and 5 stage designs respectively may be observed after simulation.

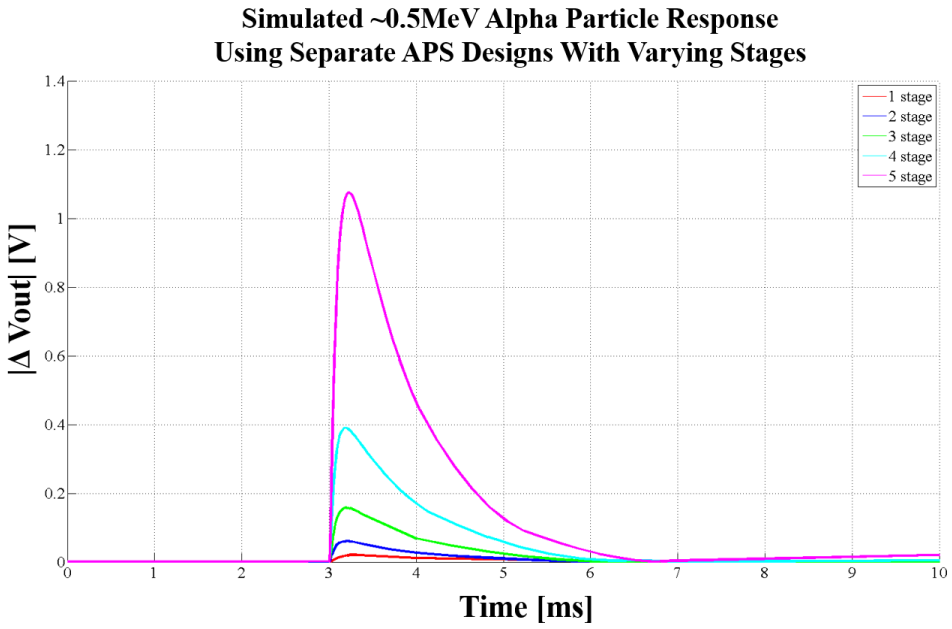

Figure 5.2: Transient simulation of a modeled alpha particle strike on the input of the new multistage APS designs. Shown are the responses of designs: each with a varying number of stages.

With this newer design, it was also noteworthy to estimate the power consumption of a single pixel. This was accomplished by simply observing the current draw from one of the supply nodes in the design during a transient simulation. For the (baseline) IGZO TFT-based 4-stage APS design shown in Figure 5.1, a static current ranging from 9 μA to 17 μA can be observed in simulations. This current, much like the gain of the APS, will be dependent primarily on the biasing voltage applied to each CS stage. With a supply voltage of 20V, these currents translate to a static power consumptions of 180 μW 340 μW per 4-stage pixel. It might be possible in future designs, that a voltage buffer or source follower will be integrated into each APS. With such a design, each pixel will dissipate more power due to the source follower. This might likely range upwards of 5 mW. However, this increased power consumption would only occur for a pixel when its particular row is asserted. Otherwise, when not asserted, the power consumption for that pixel would be comparable to the previous results described. As design of an entire detection array progresses, the issue of power consumption will likely be explored in much greater detail. However, for the purposes of evaluating these improved single pixels, the described results were deemed sufficient for the time being.

5.3 Experimental Results

Parallel to the experimental measurements in the previous chapter, each APS design was first characterized by applying a known voltage step at the input. The measured pulse at the output of the APS was then used to establish a pixel gain. Since the new APS designs exhibit varying gains based off of their respective Vbias input, a table summarizing the assortment of resulting gains according to APS stage number and biasing condition is given in Table 5.1.

After gains were established, alpha particle response measurements were made with the same externally connected OPF480 Si PiN diode and ^{210}Po alpha source used in previous experiments. Some successful detected alpha strikes on the 2-stage and 4-stage APS variants may be seen in Figure 5.3 and Figure 5.4 respectively. From these experiments it was clear that the added improvements provided both greater controllability of the APS, and higher possible pixel gain for the detection of small discrete steps of charge at the input.

Table 5.1: Table of measured APS according to the stage number and applied external bias voltage. Vdd = 20V, input step: high-level 3V, low-level = 2.99V

Vbias	2-stage	3-stage	4-stage	5-stage
1.5V	8V/V	11V/V	14V/V	40V/V
2V	12V/V	17V/V	30V/V	100V/V
2.5V	15V/V	25V/V	50V/V	180V/V
3V	16V/V	32V/V	72V/V	320V/V
3.5V	17V/V	38V/V	90V/V	420V/V
4V	17V/V	29V/V	88V/V	300V/V
4.5V	13V/V	15V/V	58V/V	72V/V
5V	9V/V	8V/V	22V/V	19V/V

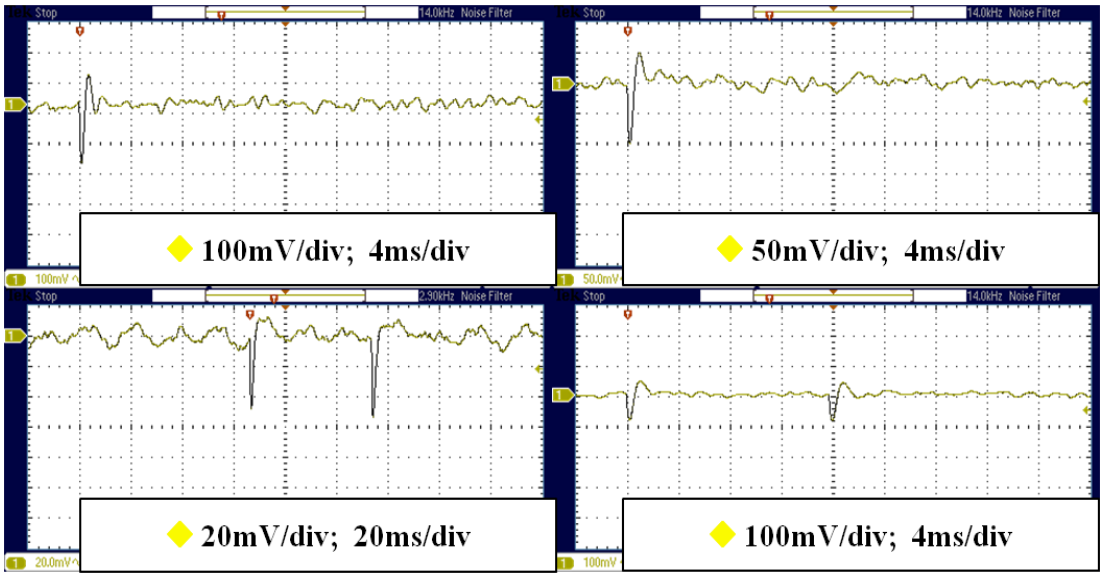

Figure 5.3: Various alpha particle strike responses measured on the improved 2-stage APS designs.

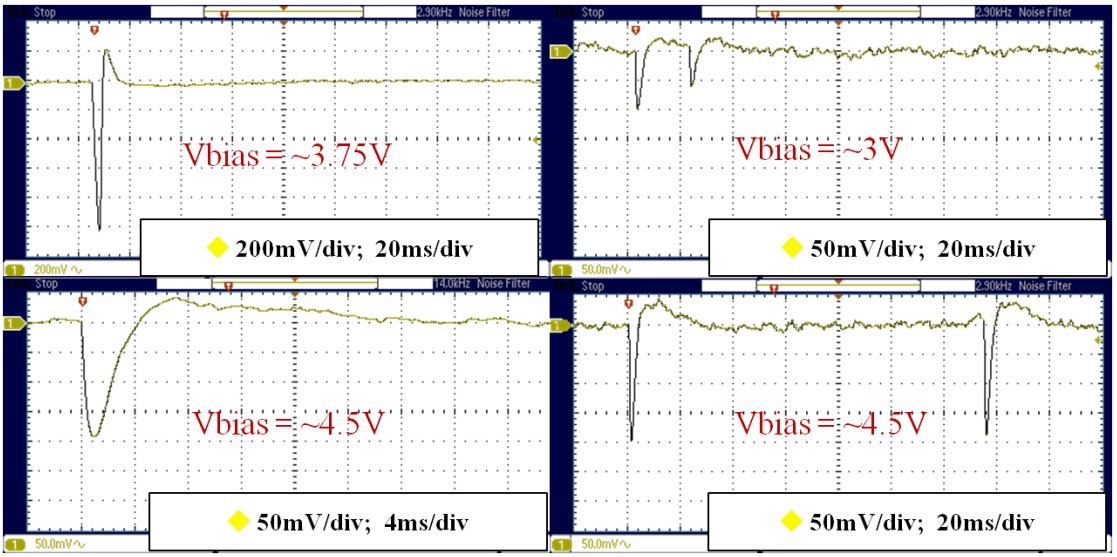

Figure 5.4: Various apha particle strike responses measured on one of the improved 4-stage APS designs. Note the improved response after adjusting the external bias (Vbias = 3.75V yields the best results)[4].

[4]My colleague Hugh Chung, one of Dr. Allee's graduate students, made these particular measurements.

6. ARRAY OPERATION AND SCALING

6.1 Introduction

A critical part of developing the new APS design is to ensure that it can operate within a large sensing array. In order to establish large detection areas, it is necessary to first evaluate various array readout implementations. Two of these readout methodologies are described in this chapter. Along with their descriptions, are discussions evaluating their merits and disadvantages with respect to large area scaling, while still being able to effectively detect neutrons.

6.2 Array Readout Methodology 1: Row Sampling

The first array read out methodology revolves around sampling each row fast enough in order to resolve the elongated detection pulse on an individual pixel. The sampled signal is then detected on an individual column line by off chip detection circuitry. The developed read out circuitry would need to sample each column for every row assertion, and digitally convert and store the sampled value. When the same row is sampled again, the newly sampled data level would be compared/differenced from the previously stored level corresponding to each respective column on the row in question. The readout circuitry then registers a positive detection whenever the magnitude of this difference is larger than a predefined threshold or lower-level discriminator (LLD). This methodology is summarized in a simplified timing diagram for a hypothetical 5-row array shown in Figure 6.1.

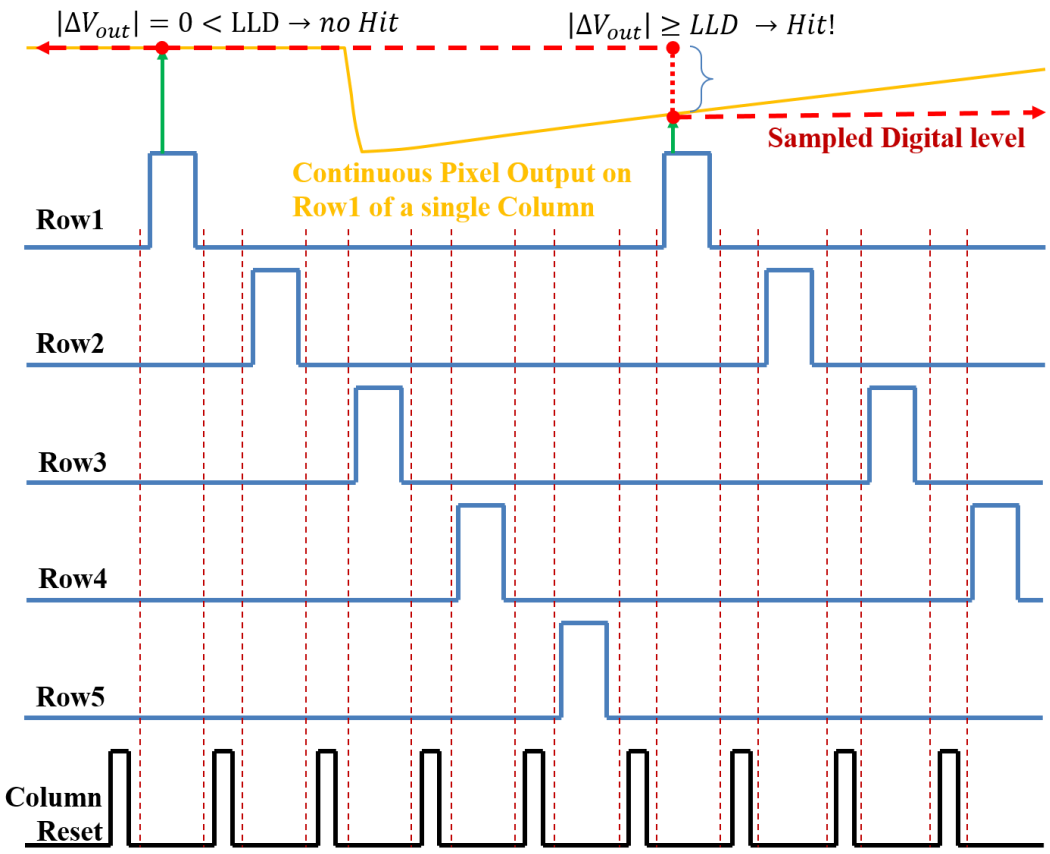

Figure 6.1: Signaling diagram for the row-sampling readout methodology of an output column associated with 5 rows. Illustrated is a situation in which an event is detected on Row1.

Given an APS array of *M* rows, a row sampling period of T_{frame}, and assuming that only half of the period T_{frame} is available for the total/summed "on time" of every row-access transistor on a single column, we can derive a simple expression for the assertion time of each row:

$$t_{assert\,row} = T_{frame}/(2 * M) \quad [sec] \tag{1}$$

Now, in order to still effectively sample a pulse at the output of a pixel, we specify that the row sampling period cannot be longer than the FWHM duration of that pulse. Assuming a downward pulse as in Figure 6.1, this ensures that at least one row-sampled

measurement will be taken at or below the "half-amplitude" mark of the pulse. Thus highlighting the worst case scenario, we can say that minimum row sampling period must equal the FWHM of the output pulse.

$$T_{frame\_min} = FWHM \quad [sec] \tag{2}$$

Now we assume that each accessed APS has a drive current of I_{drive} and the total column parasitic capacitance is C_{column} which consists of all of the parasitic row-access transistor gate capacitances and the column interconnect capacitances:

$$C_{column} \cong M * Cg_{access\_TX} + C_{interconnect} \tag{3}$$

With each column charging up by ΔV directly after a column reset and during a row-access, we can approximate the delay (τ) needed for the APS to be properly sampled at the output.

$$\tau \cong \frac{(M*Cg_{access\_TX} + C_{interconnect})*\Delta V}{I_{drive}} \tag{4}$$

It should be noted that this approximation uses $\tau = CV/I$ and ignores the effect of column sheet resistance. Equating (1) and (4), and solving for T_{frame}, it is possible to determine the minimum row sampling period required to sample all rows in an array, and still effectively resolve pulses at the output of each pixel.

$$T_{frame\_min} \cong (2 * M) * \frac{(M*Cg_{access\_TX} + C_{interconnect})*\Delta V}{I_{drive}} \tag{5}$$

Given a fixed FWHM, and recalling equation (2), the equation derived in (5) also indicates the effect of the pulse length on the scalability of the array – namely the "M" variable. Making some conservative estimates: if the pulse FWHM of the designed APS is 1ms long (resulting in $T_{frame\_min} = 1\ ms$), and assuming I_{drive} is 200 µA, C_{column} is 200 pF, and ΔV is 400 mV: M is then constrained to a maximum value of 1250 rows. From this example, we should note that in order to maximize the number of rows (i.e. array scaling capability), and assuming I_{drive}, C_{column}, and ΔV are fairly fixed, it is necessary to ensure pulses with long duration (high FWHM).

6.2.1 Effect of diode properties on APS operation

It soon becomes evident that the junction capacitance and leakage current of the detection diode have a significant impact on the overall output pulse. In order to observe this impact, both the detection diode capacitance and leakage were varied in a series of transient analyses, while the FWHM and pulse half-amplitude were measured. The results are plotted in Figure 6.2. It is clear from this figure, that in order to maximize pulse length, one needs both low diode leakage, and high junction capacitance. However, higher junction capacitance will lead to lower pulse amplitudes (as evidenced by Figure 6.2(a)). Thus, intuitively, it is best to incorporate diodes with as little leakage/dark current as possible. Given the example in the previous section, in order to attain 0.7 ms FWHM, assuming a diode capacitance of 6 pF, the diode leakage would need to be approximately 200 pA or less. Thus, given a set of fixed diode characteristics, it is possible to use these simulation methodologies in determining the total dimensions of the sensor array containing these new designs. Furthermore the techniques can be used in conjunction with optimized diode thicknesses presented in [44], in order to better design and incorporate

integrated detection diodes to these specific APS designs. Once maximum array dimensions are determined, it is then possible to simply tile separate arrays within a single detector in the interest of achieving larger surface areas.

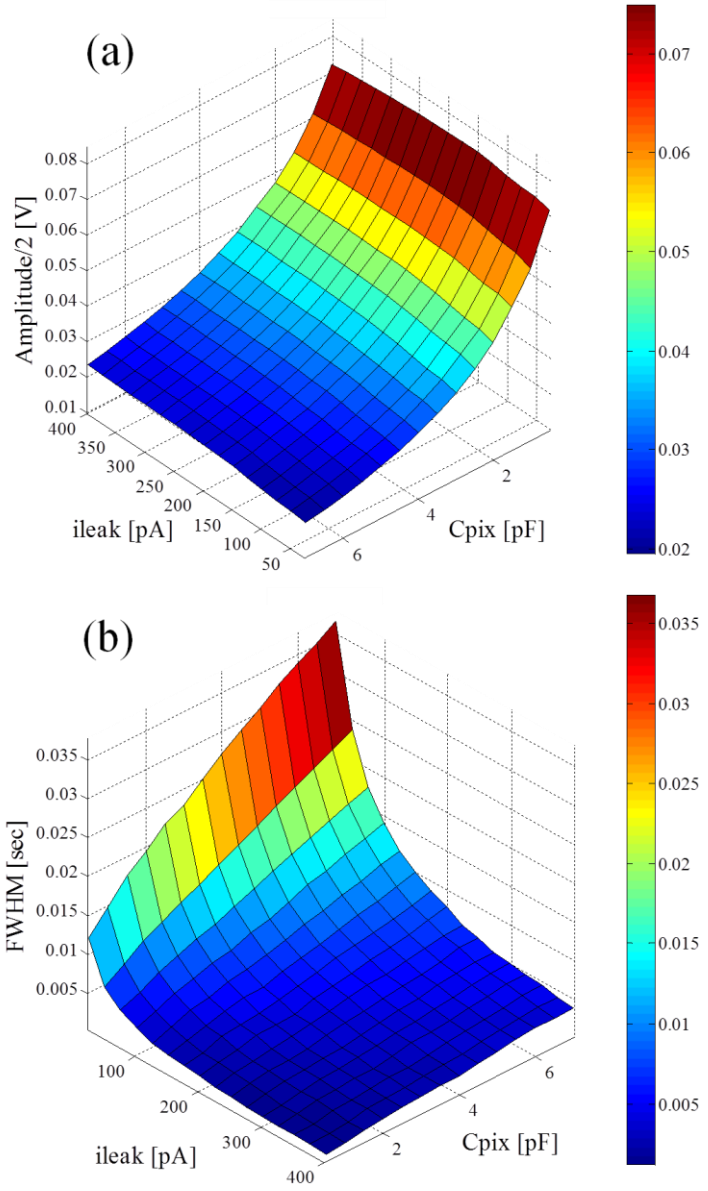

Figure 6.2: Plot (a) shows how the detection diode leakage and junction capacitance affect the pulse amplitude at the output of the 4-stage APS (seen in Figure 4.1). Similarly, (b) shows how these diode characteristics affect the duration (FWHM) of the output pulses.

6.2.2 Dead Time and Pulse Pile up

As the row-sampling readout approach requires each detected pulse to be elongated in time, there is a concern that the pulse will be too long such that it will incur pulse pile-up issues. In the case of pulse pile up, multiple events would need to occur on the same pixel within at least a FWHM length of time from each other. The FWHM duration represents an approximate estimation of the pixel's dead time in this case. Using our modeled weapons grade plutonium described before in Chapter 2, we could expect an emission rate of about $1.11*10^6$ neutrons/sec [8]. Assuming a uniform 4π steradian emission of the source, we can say the following:

$$\frac{\#\ of\ neutrons\ striking\ an\ APS}{sec} \cong \frac{A_{APS}}{4\pi r^2} * 1.11 * 10^6\ neutrons/sec$$

Here $\boldsymbol{r}$ is simply the distance of the source from the detector and $\boldsymbol{A_{APS}}$ is the area of an individual APS. As a realistic example, we will assume that $\boldsymbol{r=1m}$ and $\boldsymbol{A_{APS}=8*10^{-7}m^2}$ ($0.8mm^2$). We can then say that on average, .07 neutrons will strike a single APS per second – or equivalently, 14.15 seconds will pass before another neutron strike occurs on the same pixel – a much greater time than the millisecond FWHM dead times measured in earlier simulations. This average duration increases even more when factoring in the probability of having separate charged reaction products (from separate neutron strikes) both being detected on the exact same pixel. This example shows that since each APS is small in area, the probability of detecting merely two events on the same pixel within a

few milliseconds of one another is extremely small -- such that with this read out approach the issue of pulse pile-up on a single pixel is not an issue.

6.3 Array Readout Methodology 2: AC Coupled Rows

Another array read out methodology is to replace the row select TFT of each APS with an AC coupling capacitor. This methodology is advantageous because it eliminates the need for row select signaling. In effect, each column will continuously sense all of the APS circuits coupled to it. In turn, the column can be readout with discrete sensing circuitry at the periphery of the array.

However, this technique has some scaling issues. The more rows added and coupled to the column, the greater the capacitive loading will be. The increased capacitance of each column decreases the pulse amplitude contributed by the individual sensors at the output – leading to more difficulty in detection by peripheral circuitry. This can be seen in an alpha response simulation, where varying numbers of APS rows were AC coupled to the same column (see Figure 6.3). The APS sensor designs used in this simulation, were the new 2,3,4, and 5 stage designs described before. From observing this curve, it is clear that upward of 40 rows of the 4 or 5 stage design variants, result in lower than 50 mV pulses. This is a huge scaling disadvantage in comparison to the scaling capability of the row sampling readout technique. However, this technique still has benefits in its simplicity, and the fact that it maintains the continuous shape of the detection response at the output. This latter fact in particular, allows for low-power readout implementations via matched filters at the periphery of the array.

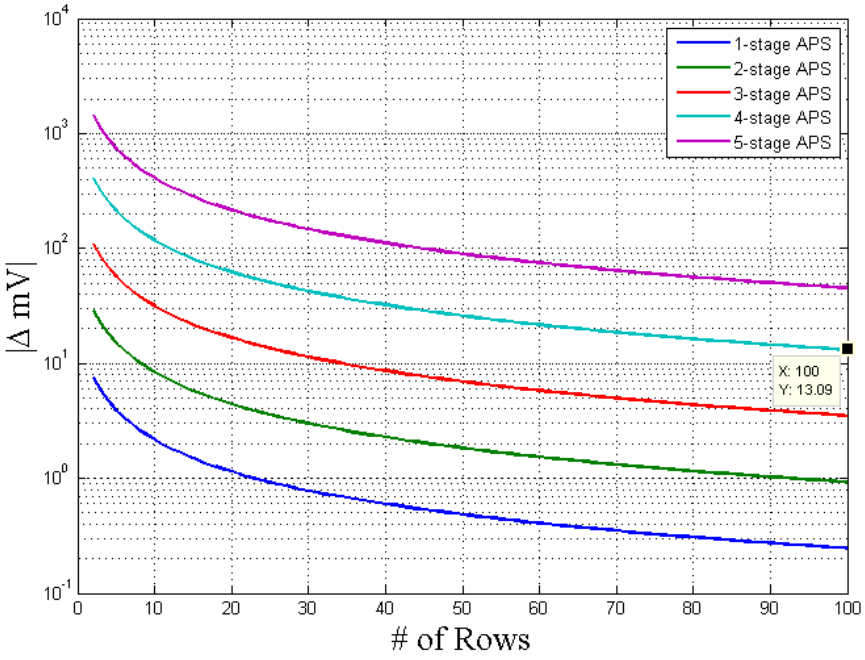

Figure 6.3 Parametric transient results of the multistage APS AC coupled to a single output column.

6.3.1 Dead Time and Pulse Pile up

Aside from decreasing overall pulse amplitude at the column output, the larger combined active area of each coupled column leads to an increased chance of pulses piling up on one another. In this case, if two events occur within a dead-time (FWHM) of each other on the same column (not on the same pixel as before), there will be pile-up issues. Thus using our previous example with the weapons grade plutonium, we can say the following:

$$\frac{\#\ of\ neut.striking\ sensor\ column}{sec} \cong \frac{\#rows * A_{APS}}{4\pi r^2} * 1.11 * 10^6\ neutrons/sec$$

Again, we will assume that ***r=1m*** and $A_{APS}=8*10^{-7}m^2$ ($0.8mm^2$), and that ***#rows=20***. In this case, on average it would be roughly 700 miliseconds in between neutron strikes on the sensor column. Thus, due to pulse pile-up issues, the scaling for this scenario, would be limited to about ***#rows=2000*** – where the time in between strikes decreases to about 7ms (on order with the FWHM of a single pulse). From this simple example, it can be determined that scaling with the "AC coupled rows" read out technique will be primarily limited by the decreasing signal at the output due to capacitive loading (as seen in Figure 6.3) before pile-up issues take effect.

6.4 Conclusion

This chapter presents two possible read out methods and their effect on array size scaling. The row sampling method relies on sampling every pixel with enough samples in order to effectively resolve/detect an incident. For this method to function optimally, each pixel's detection response must be elongated in time to allow for sufficient sampling. The "AC Coupled Row" array readout methodology is much simpler to implement, however, it's scaling is limited in comparison to the row-sampling readout technique. Thus, if large area array scaling is critical, the row sampling method emerges as the best choice. However, the AC coupled row technique should not be discounted if shape of the detection pulse is to be preserved. Furthermore, the AC coupled row technique can benefit from low-power matched filter readout circuitry at the periphery.

7. MATCHED FILTER FOR COLUMN READOUT

7.1 Introduction: Array Readout using Matched Filters

The external readout circuitry of the detection array needs to reliably detect small signals. This becomes especially true in the array read-out methodology of coupling a column output to all of its corresponding row-pixels. Referring back to the previous chapter, as more rows are added, the weaker the detected signal will be at the output. A growing concern is with scaling, these small signals will be buried in noise. One attractive notion is to use a matched filter (MF) for the external readout of such small pulses. By designing a filter with an impulse response closely matching the measured alpha-induced pulse at the column output, we can optimally filter out any white noise added to the channel. Thus, these de-noising properties of a matched filter (MF) allow for weaker pulses – often buried in noise, to be detected from long pixel-column output nodes. This chapter gives a basic overview of the signal processing benefits of the MF, and discusses the ongoing design of such a filter for the external readout of the before-mentioned multi-stage APS designs.

7.2 Matched Filters – a Brief Overview

Given a signal s(t), which we would like to detect, we say it is corrupted by a white noise source n(t), resulting in a received signal r(t) such that the following is true:

$$r(t) = s(t) + n(t)$$

We then apply a filter (with impulse response h(t)) to the received signal, and the resulting output is y(t):

$$y(t) = r(t) * h(t) \;\; (where \;\; * \; denotes \; convolution)$$

We need to then find the optimal filter structure such that the signal power component of y(t) is maximized with respect to the noise power component of y(t) – namely we need to maximize signal to noise ratio (SNR). We can denote the following equation for the SNR [50]:

$$SNR = \frac{\left[\int_0^t s(u)h(t-u)du\right]^2}{E\left[\int_0^t n(u)h(t-u)du\right]^2}$$

It can be shown that in order to maximize the SNR, the optimum filter must exhibit an impulse response $h_{opt}(t)$ matching the actual signal s(t) [50]. Intuitively this makes sense since the signal component of y(t) will be strongly correlated in time to the optimized filter, whereas, the white Gaussian noise components added on top of the signal will not.

In order to better illustrate the benefit of using a matched filter for readout of our detection array, consider the following case study. An ideal single pixel alpha response, Figure 7.1(a) is corrupted and buried in white noise as seen in Figure 7.1(b). This noisy signal is then filtered by a matched filter, and results in a signal closely resembling the original ideal response.

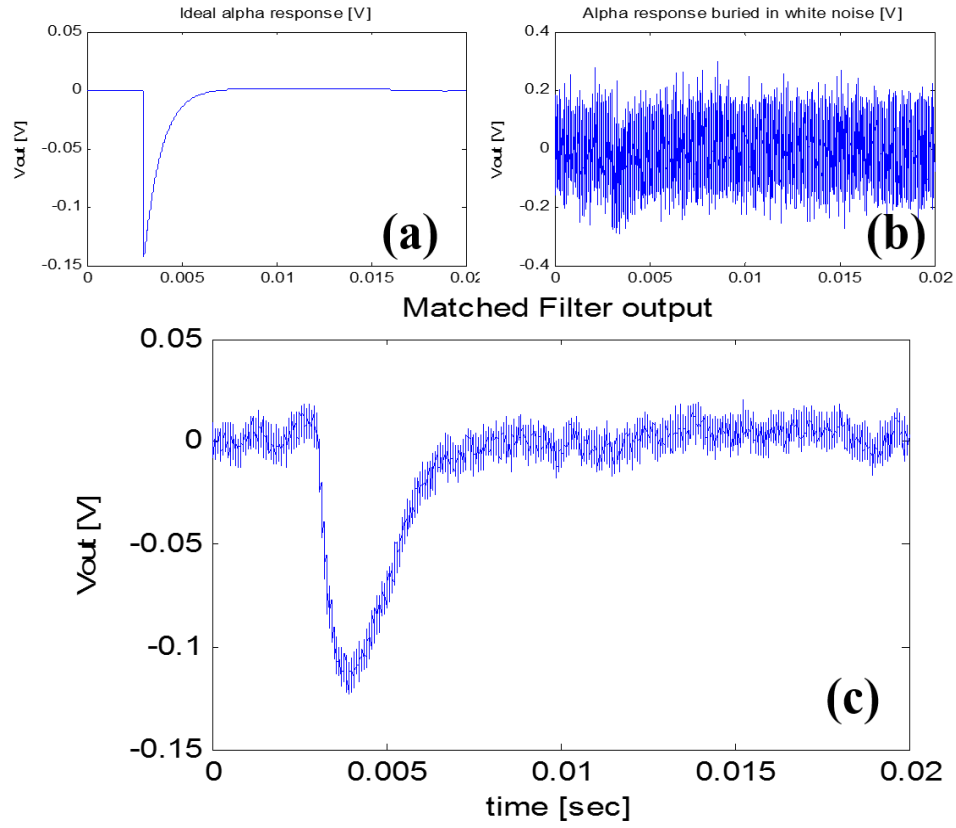

Figure 7.1: (a) Ideal single pixel alpha Response. (b) Alpha response buried in white noise. (c) Matched filter output closely resembling ideal signal.

Now, if we set the detection threshold of our system to ½ of the expected output pulse amplitude, we can estimate the probabilities of attaining "false positive" detections when measuring either the filtered or unfiltered waveforms. Furthermore, since the amplitude of the ideal signal scales down with additional rows, we can estimate this probability as

both a function of the added white noise, and the ideal pulse amplitude (and thereby estimate the amount of rows in the array). A comparison of both the filtered and unfiltered relationships may be seen in Figure 7.2.

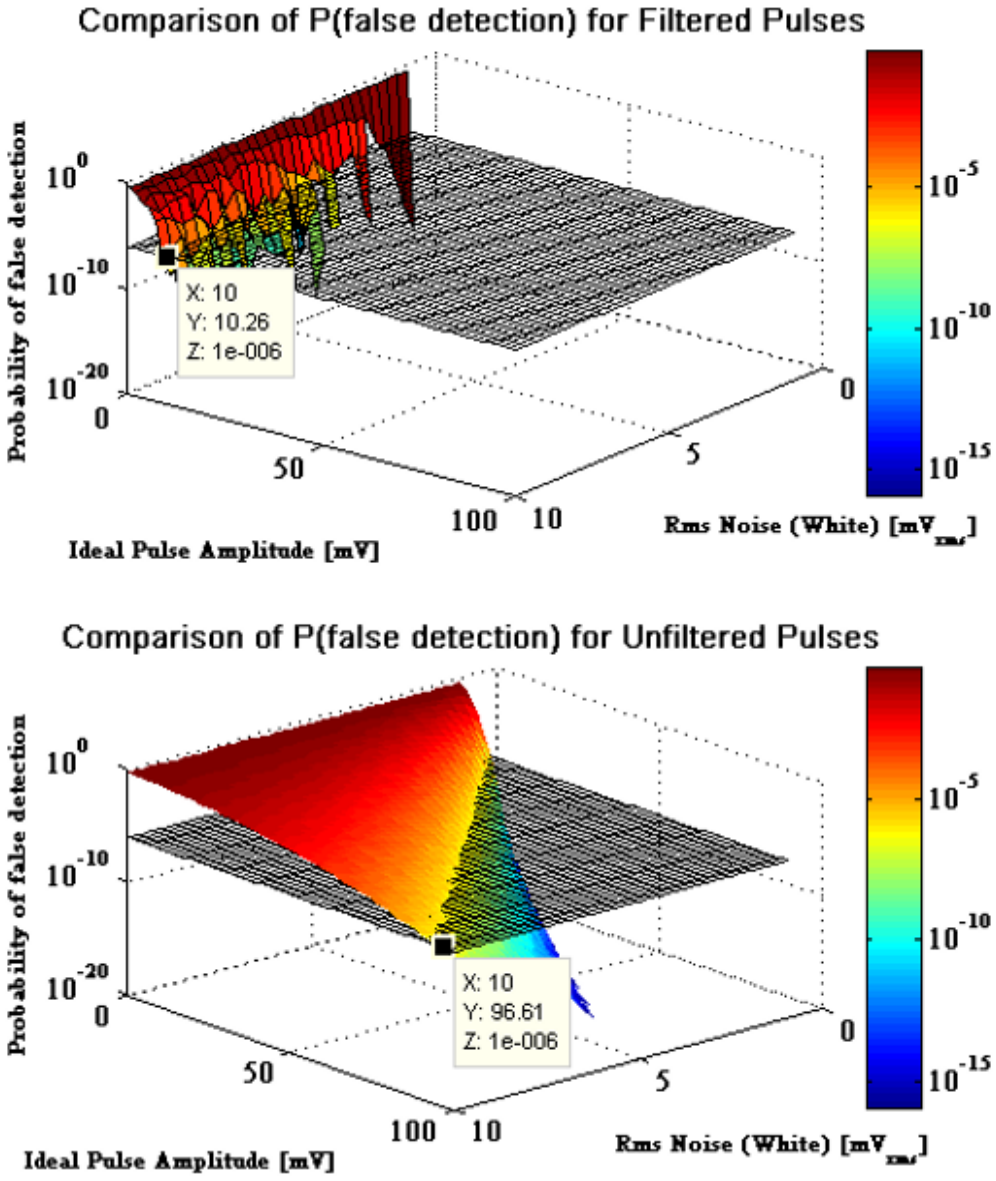

Figure 7.2: Comparing the probability of false detection for filtered (Top) and Unfiltered (Bottom) responses. Matched filtering ultimately allows for much lower output responses to result in true positive detections.

From this comparison, it is clear that matched filtering allows for much smaller signals to be measured at the output of each column (in an AC-coupled row readout methodology for instance), and still have these signals result in true positive detections, rather than false positive detections incurred by external noise. From this analysis, and the analysis seen in Figure 6.3, we can show that with matched filtering, one can support approximately 100 rows of 4-stage APSs before false positive detection probabilities go above 10^{-6} (assuming 10 mVrms white noise injected on the column). However, without filtering this number of rows drops to about 10. Thus, this comparison especially illustrates the array scaling benefits when using a matched filter for column read out.

7.3 Matched Filter Design Methodology

For the purpose of increasing the SNR of detected alpha strikes on a column line, it is necessary to design a matched filter whose impulse response closely matches that of an alpha strike from one of the pixels. The following sections discuss the steps in which such a filter may be realized.

7.3.1 Modeling the Alpha Strike

The first step in the filter design process is to establish the required filter impulse response. Thus from previous discussions of matched filters, the alpha strike APS response will be the starting point from which we develop a filter impulse response. For the initial design highlighted in this document, actual waveform data resulting from experimental tests of the 4-stage APS were used (similar to that seen in Figure 4.4(b)). The raw data was then fit to a "best-fit" polynomial function in MATLAB.

7.3.2 Realization of an S-Domain Transfer function

With the best-fit polynomial function of an actual measured alpha response, it was possible to then take this function and treat it as a filter impulse response within MATLAB. Realizing this, the next step was to use this impulse response in generating the appropriate S-Domain filter transfer function, which would result in such a response. This process is started by generating a state space realization. The state space realization essentially models the ideal transfer function in the S-domain using four matrices: A, B, C, and D. In order to attain the state space realization of the impulse response function, it is necessary to utilize the "*imp2ss*" function (impulse response to state space) in MATLAB. This function is found in the "***robust***" toolbox. For example, the following code creates a state space representation of the impulse response "PSI":

```
[a,b,c,d,tolbnd,hsv] = imp2ss(PSI, .02, 1 , 1);
% Note, PSI must be causal (not have values for time < 0)
```

7.3.3 Approximation

Following the generation of the state space, it is further necessary to approximate and reduce the order of the state space model to ensure realistic implementation in actual filter circuitry. The two approximations best suited for low-power filter designs are the Pade' Approximation, and the L_2 approximation. Chapter 5 of reference [51], and reference [52] discuss these approximations in detail. For the purposes of this project, only the built in balance and reduce operations ("balred" function in the Control System Toolbox) in MATLAB, were available for use[5]. In future designs, however, the L_2 approximation

[5] A special thank you to Dr. Stephen Phillips who pointed our group to this code

will be used. The L_2 approximation is based off of minimizing the least mean square error between the approximation and the ideal. Work is currently being done to implement this approximation in the automated design of these filters.

7.3.4 Synthesization of a gm-C based ladder filter using an S-domain transfer function

Given the S-domain transfer function generated from the previous steps, we can then generate an appropriate ladder filter structure. Denoting *H(s)* as our S-Domain transfer function, it is possible to use the following procedure ("divide-invert-divide") to realize the actual transconductance values in a gm-C ladder filter [51][52][53]:

$$H(s) = \frac{A_{N-1}s^{N-1} + A_{N-2}s^{N-2} + \cdots + A_0}{B_N s^N + B_{N-1}s^{N-1} + B_{N-2}s^{N-2} + \cdots + B_0}$$

$$Numerator: P(s) = A_{N-1}s^{N-1} + A_{N-2}s^{N-2} + \cdots + A_0$$

$$Denominator: E(s) = B_N s^N + B_{N-1}s^{N-1} + B_{N-2}s^{N-2} + \cdots + B_0$$

Now we apply a "continued fraction expansion" of the Denominator $E(s)$. We take $E(s)$ and split it into two equations -- one with all the even order terms, and one with all of the odd order terms:

If N is even:

$$X1(s) = B_N s^N + B_{N-2}s^{N-2} + \cdots + B_0 \quad \rightarrow \quad all\ even\ order\ terms$$

$$X2(s) = B_{N-1}s^{N-1} + B_{N-2}s^{N-3} + \cdots + B_1 s^1 \quad \rightarrow \quad all\ odd\ order\ terms$$

If N is odd:

$$X1(s) = B_N s^N + B_{N-2} s^{N-2} + \cdots + B_1 s^1 \quad \rightarrow \quad all\ odd\ order\ terms$$

$$X2(s) = B_{N-1} s^{N-1} + B_{N-2} s^{N-3} + \cdots + B_0 \quad \rightarrow \quad all\ even\ order\ terms$$

Now we begin to determine "R" values by dividing X1(s) by X2(s), recording the remainder, and iterating in the following manner:

$$\frac{X1(s)}{X2(s)} = \boldsymbol{R_N} * s + \left(remainder_N(s)\right)$$

$$\frac{X2(s)}{remainder_N(s)} = \boldsymbol{R_{N-1}} * s + \left(remainder_{N-1}(s)\right)$$

$$\frac{remainder_N(s)}{remainder_{N-1}(s)} = \boldsymbol{R_{N-2}} * s + \left(remainder_{N-2}(s)\right)$$

$$\vdots$$

$$\frac{remainder_3(s)}{remainder_2(s)} = \boldsymbol{R_1} * s + \left(remainder_1(s)\right)$$

Taking these newly calculated "R" values, we now calculate α coefficients according to the following procedure:

$$\boldsymbol{\alpha_N = \frac{1}{R_N}} \quad \& \quad \boldsymbol{\alpha_i = \sqrt{\frac{1}{R_i * R_{i+1}}}} \quad \boldsymbol{for\ 1 \leq i} < N$$

We also calculate a β_1 coefficient based off of the R_1 value:

$$\boldsymbol{\beta_1 = \sqrt{\frac{R_1}{\pi}}}$$

Now we calculate "*F*" values using the following procedure:

$$\boldsymbol{F_1 = \frac{\beta_1 * E(0)}{E(s)}} \quad \& \quad \boldsymbol{F_2 = \frac{s * F_1}{\alpha_1}}$$

$$\boldsymbol{F_i = \left(\frac{1}{\alpha_{i-1}}\right) * (s * F_{i-1} + \alpha_{i-2} * F_{i-2}) \quad for \quad 3 \leq i \leq N}$$

After calculating all "*F*" values, it is necessary to choose corresponding "*C*" values such that we can attain the original numerator *P(s)*, in the following manner:

$$\boldsymbol{C_N F_N + C_{N-1} F_{N-1} + C_{N-2} F_{N-2} + \cdots + C_1 F_1 = P(s)}$$

After successful completion of this process, one should have an array of $\boldsymbol{\alpha}$ values and an array of $\boldsymbol{C}$ values. All of these values correspond to the relative gm values of the transconductors in a gm-C based orthonormal ladder filter [52]. This can be better understood by studying Figure 7.3. Here we observe the generalized gm-C block diagram of our ladder filter, which uses all of the calculated $\boldsymbol{\alpha}$, $\boldsymbol{\beta}$ and $\boldsymbol{C}$ coefficients.

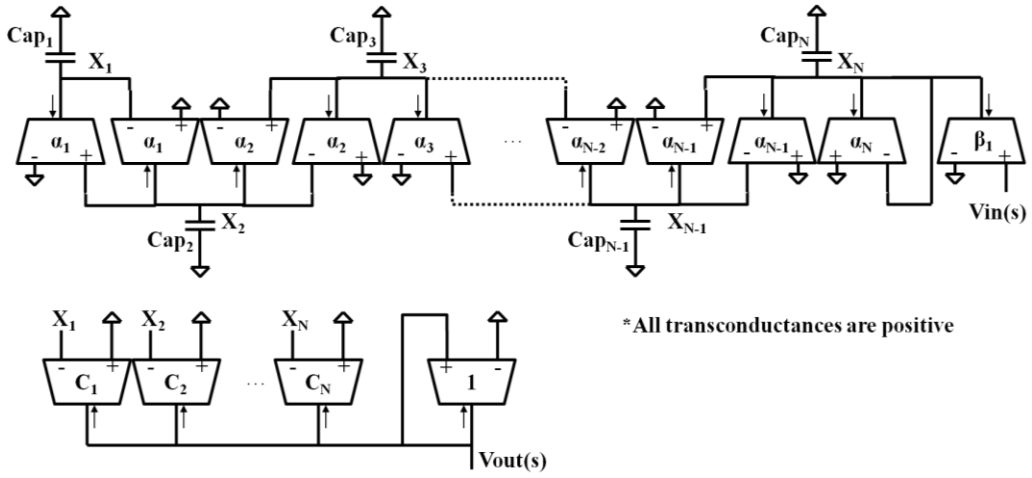

Figure 7.3: Generalized gm-C block diagram used for implementing the orthonormal ladder filter (architecture is used from reference [52])

Observing Figure 7.3 , it is relatively straightforward to generate a customized ladder filter. Each integrator in Figure 7.3 is represented by one capacitor, while the summing and scaling operations are implemented by individual transconductors. It should be noted that the transconductance gains need to maintain their relative values to one another according to their respective calculated $\boldsymbol{\alpha}$, $\boldsymbol{\beta_1}$, and $\boldsymbol{C}$ coefficients.

This method was ported to a MATLAB script in order to further speed up designs. This script was then used to generate a matched filter netlist corresponding to a measured alpha strike. To maintain a simple design, a 3rd order approximation S-domain filter response was generated in MATLAB and implemented in a netlist representing a gm-C ladder[6]. Once the netlist was generated, it was possible to further manually optimize transconductance values to model a more realistic design, and a closer impulse response fit to the actual alpha response. Initial simulations simply used ideal transconductors and capacitors to implement the ladder filter (as seen in Figure 7.4).

7.4 Conclusion

The end goal of this work is to automate the described design methodologies given in this report. Thus, when given a particular signal of interest, one might easily generate an optimized filter at the netlist and layout level. The completed automation up to date, allows the user to generate a reduced order S-domain transfer function – with an impulse response closely matching the signal provided by the user. MATLAB scripts will automatically synthesize a gm-C ladder based off of the "divide-invert-divide" algorithm described beforehand. Essentially, the end result is a generated netlist. Future work on this

[6] Dr. Allee's student, Anthony Pelot helped develop a great majority of this MATLAB script.

automation process, will take this netlist, and then place and route cells from a manually created standard cell library into a top level wavelet filter. Additional improvements such as implementing L_2 approximation scripts, and digital calibration will follow as well.

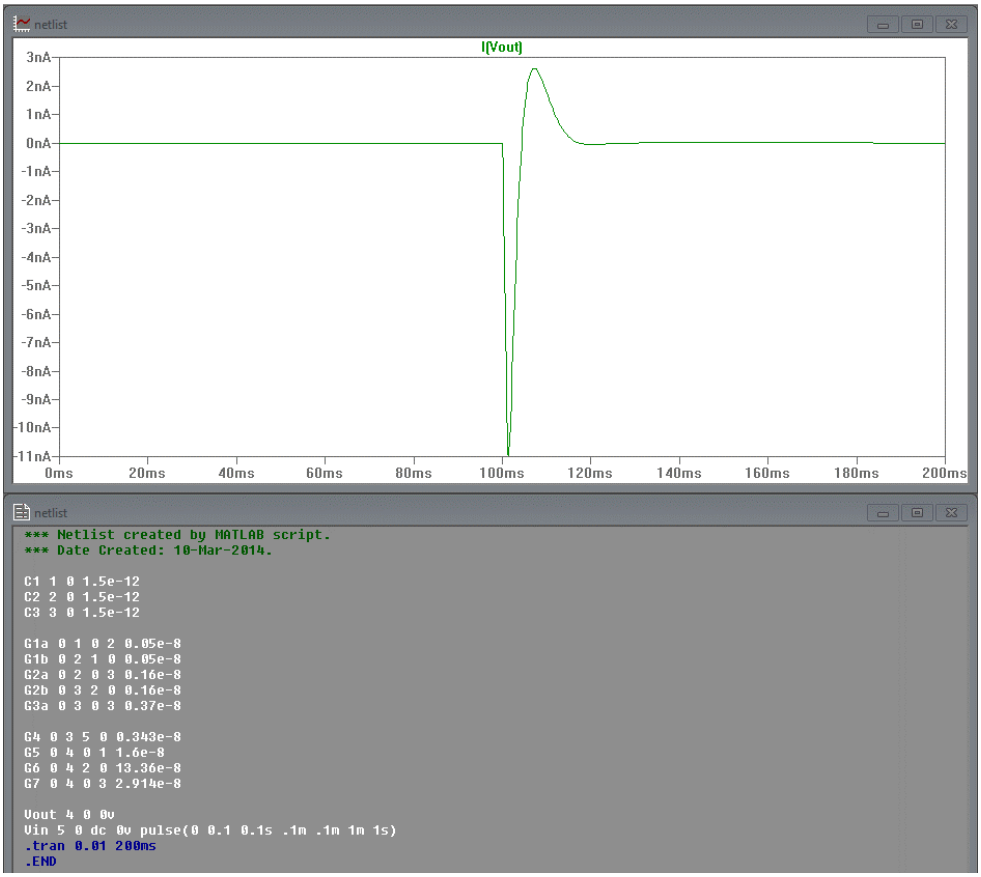

Figure 7.4: Current-mode impulse response closely matching that of a measured alpha strike (Top). Below is shown the netlist which uses ideal voltage-controlled current sources and capacitors to generate the impulse response (Bottom).

8. DETECTION DIODES SUITABLE FOR INTEGRATION WITH THE APS

8.1 Introduction

Up to this point, this manuscript has presented alpha-response experimental results attained from detecting particles with an external commercially available Si PiN diode (the OPF480). Eventually, this diode needs to be replaced by an integrated detection diode which will ultimately be fabricated over the APS – therefore, allowing for optimal fill factor ($\leq 100\%$). Initial attempts discussed here, sought to develop flexible a-Si:H PiN diodes above the developed APS designs. Currently, CdTe detection diodes are being developed by the University of Texas at Dallas (UTD) as an alternative low-cost integrated detection element [49].

8.2 a-Si:H PiN Detection Diodes for Charged particle Detection

Initial attempts at producing an integrated diode for the TFT-based amplifiers, centered on using flexible a-Si:H PiN diodes. a-Si:H PiN diodes were developed by the ASU flexible display center (FDC) for the main purpose of X-ray detection, however, it was deemed possible that these diodes might also detect high energy charged particles as well. To prove initial feasibility, alpha particles emitted from the exempt ^{210}Po source would need to be detected on one of these diodes and amplified through the charge sensitive preamplifier implemented from [6][40]. Once successful alpha strikes were observed using this technique, later experiments would have then replaced the preamp (CSP) with the less-sensitive TFT-based amplifiers. Separate diode test structures of varying areas and thicknesses were developed using the same low-temperature TFT fabrication process

on flexible polyethylene napthalate (PEN) substrates as described in previous chapters[7]. The intrinsic layer thicknesses were 1.2um, 2.4um, 4.8um, and 7.2um. To date, extensive experimental measurements have yielded no observable alpha response detections using these diodes. The conclusion for these results is that alpha induced charge collection efficiency was too low for the a-Si:H diodes. This notion is further supported by the findings presented in [46][47]. Assuming a reverse bias voltage of 10V and a thickness of 7.2um, the results reported in [47], would yield a charge collection efficiency on the order of less than 2%. It should be noted that reverse bias voltages up to 60V were applied to the FDC a-Si:H diodes, and no noticeable alpha response was measured at the output of the CSP. Furthermore, typical energy loss distributions for ionizing particles within a-Si:H are shown to be so low, that at least 10's of microns (+40 μm thick detectors are generally preferable) are necessary to obtain a large enough signal [48]. Due to these issues, an alternative to the a-Si:H diodes was required.

8.3 CdTe Detection diodes for Charged particle Detection

CdTe detection diodes are being developed by the University of Texas at Dallas (UTD) optimized specifically for the purpose of detecting charged particles emitted from a thermal neutron capture within a ^{10}B converter layer. Charge collection efficiencies for these devices have not yet been published but will range upwards of 80%[8]. Using CdTe thin

[7] Michael Marrs, the Principal Process Engineer at ASU's FDC, dedicated his time toward developing and fabricating these structures for this project.

[8] This information is courtesy of John Murphy: a UTD graduate student working for Dr. Bruce Gnade. He will be publishing the specifics pertaining to these results at a later time.

film based detectors, and conventional charge preamplifier readout techniques, measurements reported in [49] illustrate successful charged particle detection under both alpha radiation, and neutron radiation in conjunction with a neutron converter.

For proof of feasibility, it was necessary to show that the multistage APS design could effectively readout alpha induced signals resulting from detections on a CdTe detection diode. An assortment of CdTe diode samples were shipped from UTD to ASU for testing. An example I/V sweep of one diode may be seen in Figure 8.1. Using the diode measured in Figure 8.1, it was possible to then connect it externally to a 4-stage APS. It should be noted that the 4-stage APS used in these earlier measurements, is the original design (from Chapter 4), and did not yet include the design improvements outlined in Chapter 5. The CdTe diode was irradiated with a moderated ^{210}Po alpha source, which was angled toward the sample as seen in Figure 8.2. The alpha source was moderated with a thin sheet of kapton, which resulted in alpha particle energies roughly down to 1.5-2 MeV energies consistent with αparticle energies from the ^{10}B neutron capture reaction.

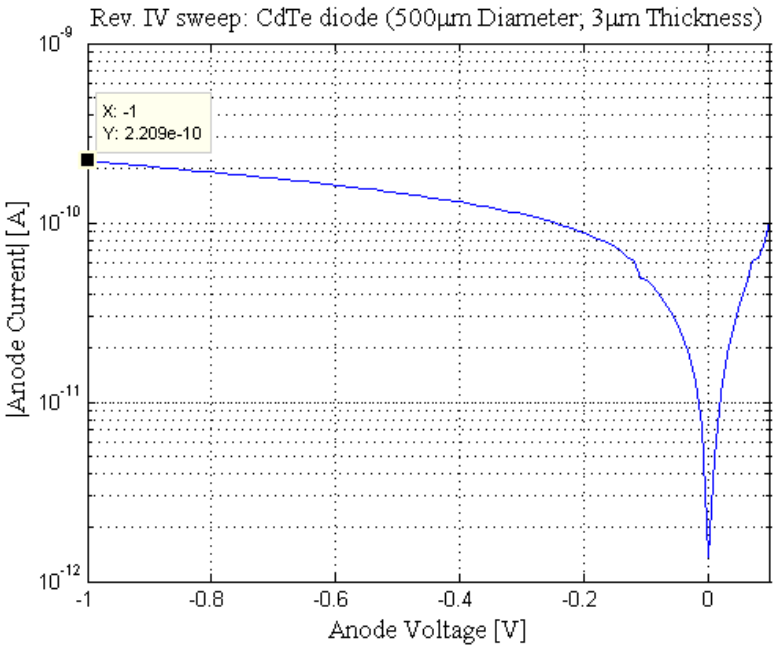

Figure 8.1: IV sweep of the CdTe diode. This particular diode was later used in successful alpha particle radiation measurements in conjunction with the IGZO based multi-stage APS. The 3µm thickness refers to the approximate thickness of the depleted region of the diode.

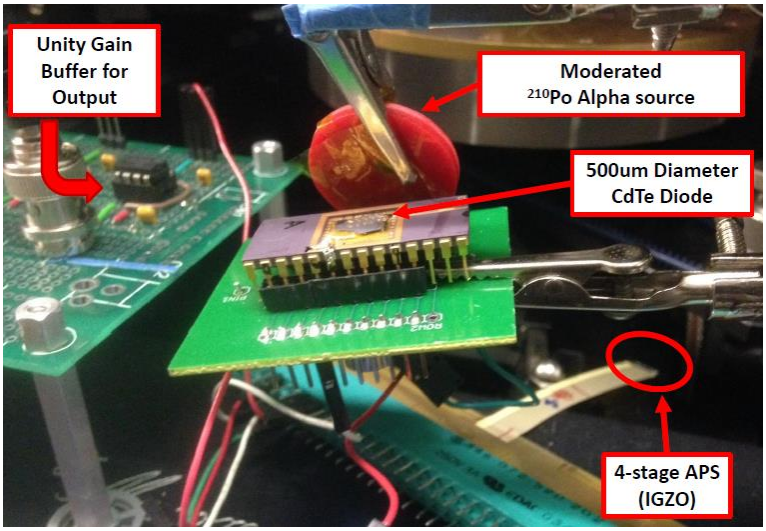

Figure 8.2: Setup for measuring the alpha response of a 4-stage APS with an externally connected CdTe diode.

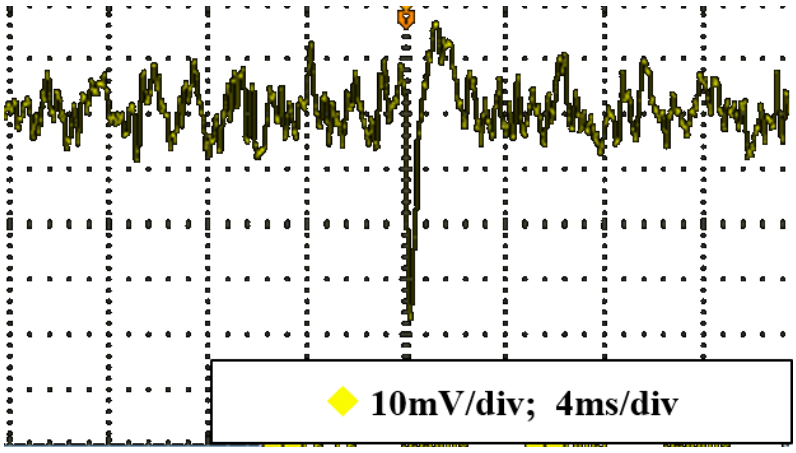

Figure 8.3: Alpha induced pulse measured with an externally connected CdTe detection diode and the 4-stage APS.

Visible alpha strikes (as seen in Figure 8.3) were subsequently measured proving that the CdTe diode in conjunction with the TFT based multi-stage APS could indeed detect and effectively readout alpha particle strikes. It should be noted that the reverse bias "dark" current of the CdTe diode was larger than the dark current of the commercial Si OPF480 used in previous experiments (~2nA of the CdTe diode compared to 0.1nA of the OPF480). This largely contributes to the increased noise observed at the pixel's output.

Later experimental measurements included the updated APS designs described in Chapter 5, and used a newer set of CdTe diode samples sent from UTD. Initial IV sweeps of a 300 μm diameter diode may be seen in Figure 8.4. Similar to previous measurements, the ^{210}Po alpha source was moderated with a thin sheet of Kapton, and angled toward the diode. The diode was probed, and connected to the input of a 4-stage APS. The APS

was tuned to its high gain state, and as a result strong alpha-induced signals were successfully observed at the output of the APS. These may be seen in Figure 8.5[9].

8.4 Conclusion

Initial attempts at developing integrated a-Si:H based detection diodes at ASU's flexible Display Center (FDC) resulted in diode samples with insufficient sensitivity to alpha particles while using conventional charge preamplification circuitry. As the current multistage TFT-based APSs are less sensitive than the conventional charge preamplification techniques, the use of FDC's flexible a-Si:H photodiode, for now, has been ruled out as an integrated thin-film solution for the detector design. Luckily, however, CdTe detection diodes developed by ASU's collaborators at UTD, have been shown to effectively detect high-energy alpha particles resulting from thermal neutron capture reactions [49]. Furthermore, these diodes in conjunction with the new multi-stage APS design have been shown to successfully and reliably detect incident alpha particle strikes. Thus the detector system design will move toward merging a CdTe detection diode with its own multistage APS.

[9] My colleague Hugh Chung, made these particular measurements

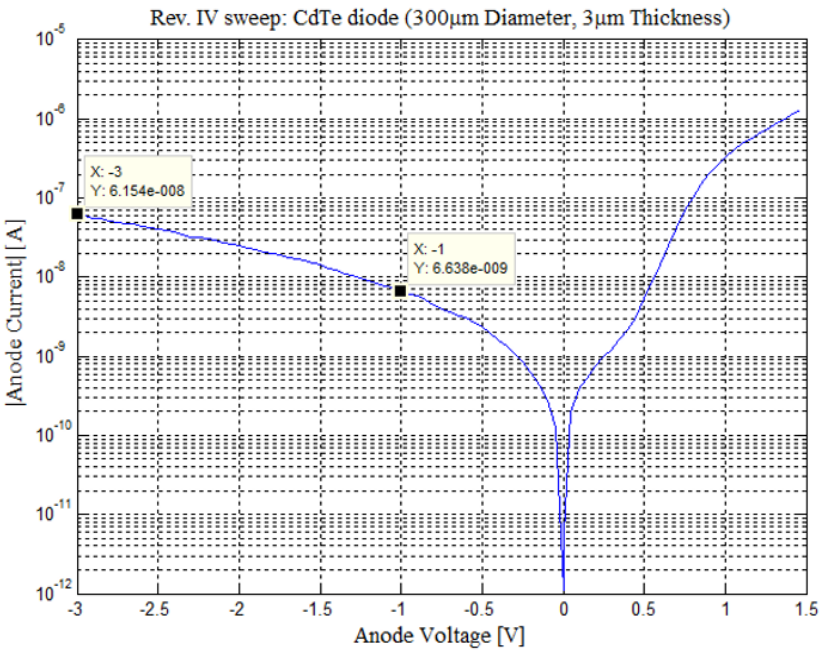

Figure 8.4: IV sweep of the 300 µm diameter CdTe diode.[10] The 3 µm thickness refers to the approximate thickness of the depleted region of the diode.

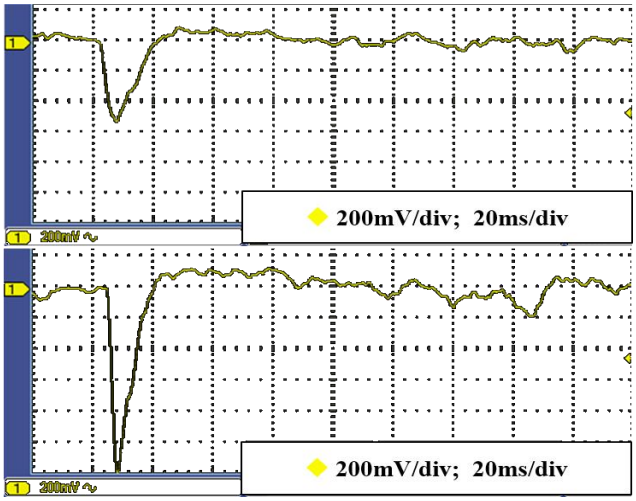

Figure 8.5: Alpha particle detections measured with a 300 µm diameter CdTe diode, and an improved (Chapter 5) 4-stage APS. The APS was biased with an external supply set to about 3.8V (V_{DD} supply was set to 20V).

[10] IV Data for this plot were supplied by the researchers at UTD

9. CONCLUSIONS AND FUTURE WORK

9.1 Original Contributions

In terms of Active Pixel Sensor Design my major original contribution is the invention of a new multi-stage TFT-based amplifier capable of reliably detecting individual alpha particles. In doing so, I have demonstrated and proved the viability of using flat panel TFT technology, for the detection and readout of charged particles – a requirement for the operation of a conversion-layer-based neutron detector. Another major contribution pertaining to the nuclear modeling of a planar thermal neutron detector (using MCNP/MCNPX), is the characterization and optimization of the detection diode thicknesses and materials with respect to gamma rejection. A minor contribution includes developing new ZnO TFT based APSs designs. This constituted developing new BSIM3 ZnO device modeling, initial circuit-level simulation, and layout. Other minor contributions include defining and modeling array scaling limits while using two separate array read-out methodologies. The first methodology was the row-sampling array readout, and the second was the AC-coupled array read-out methodology. Another minor contribution was the development of a gm-C based, matched filter for column read-out.

9.2 Future System Model Work

The modeling of the "front-end" planar detector in MCNPX has laid the foundation for a more complex model. The back-plane detector array model will also continue to evolve along with the improvement of the detector system design itself. Thus, when newer sensing circuit designs are developed, for example, the existing backplane APS modeling can be frequently adapted to evaluate updated array architectures.

9.3 Fabrication and Testing of Matched Filter for Detector Readout

9.3.1 Transistor level design: Low-power Transconductor

In order to implement the gm-C ladders described in the previous sections, it is necessary to design a low-power transconductor to take the place of all the gm elements. In this current design, it was decided to utilize the CMOS triode transconductor described in [54]. This transconductor, pictured in Figure 9.1, uses an input differential pair which is consistently kept in the triode operating regime. This is done in order to sustain a low gm/I_D relationship, which ultimately ensures better controllability of the transconductor's total transconductance [54].

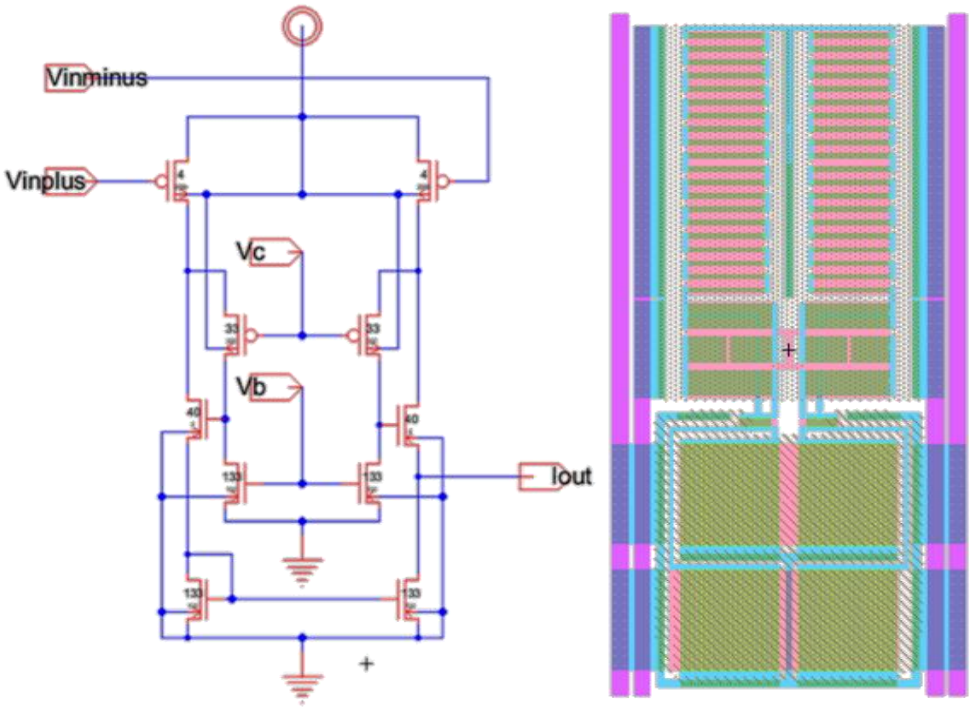

Figure 9.1: Schematic (left) and Layout (right) of the nA/V CMOS triode transconductor. The design used was derived from [54].

Various methods can be used to control the transconductance of each gm cell. One way, is to vary the W/L ratio of the PMOS differential pair which in turn adjusts the total transconductance (an example layout of this is seen in Figure 9.2). The transconductance may also be controlled using the biasing voltages V_B and V_C, by tuning appropriate biasing circuitry [54]. Unfortunately, however, the first method will be extremely prone to process variations and could easily result in mismatching of absolute transconductances (generally on the order of 20% or higher) [55]. Ultimately, it becomes necessary to tune each transconductor via a voltage bias. Furthermore, in order to allow for better matching, it is beneficial to use a unit transconductor which can then be copied, arrayed, and connected in parallel in order to ultimately make a larger gm cell whose transconductance is then a multiple of the unit transconductor. Thus, as long as the unit transconductors are well matched with one another, this ensures that the gm ratios in the whole filter design are dependent on ratios of unit transconductor instances (rather than process dependent device widths and lengths). With this methodology, only one universal biasing voltage would need to be used to tune every unit transconductor in the design. This is contrasted to using a fairly complex biasing array of separately tuned voltages to control individually sized transconductors.

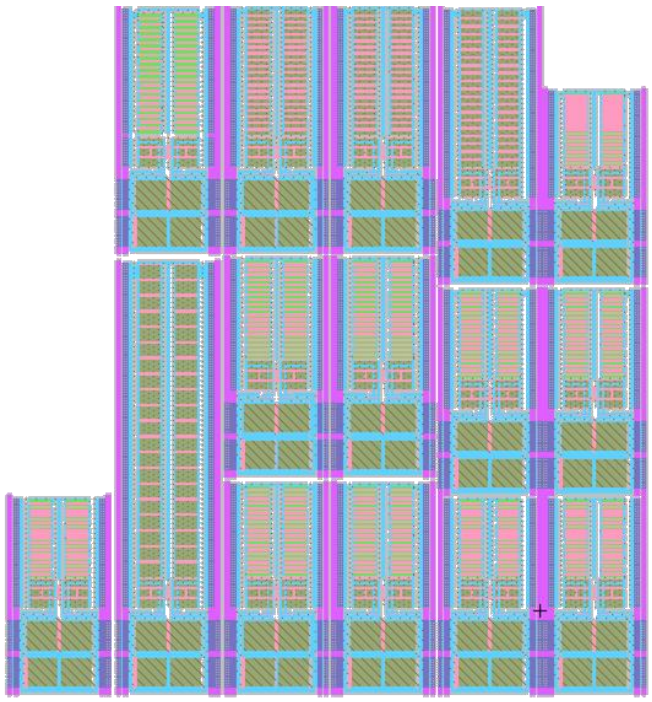

Figure 9.2: Top-level layout of a wavelet filter (shown without top-level routing and biasing). The layout shows various sized transconductors, which could eventually be automatically placed and routed based off of a netlist automatically generated in MATLAB.

Other issues to overcome are variations in the "gm/C" frequency parameter for each integrator section of the ladder. Even though the ratios of these parameters to one another should be matched (as described in the previous paragraph), any global variation such as temperature could vary this parameter from its desired value. For the matched filter, this would ultimately cause stretching or condensing of the desired impulse response. In order to mitigate this issue, it is recommended to explore implementation of an integrated background tuning control loop as described in [55]. Such an approach could use frequency tuning to adjust the transconductor biasing in a replica gm-C integrator. The control loop would work such that the biasing voltage causes the total gm/C value of the replica integrator to equate to a desired reference frequency (provided by the user externally). To the

extent that the transconductor in the replica matches the transconductors in the filter, this biasing voltage would then allow proper tuning filter gm/C values over any global variations.

9.4 Ongoing APS Implementation with ZnO TFTs

The multi-stage APS designs need to be implemented using ZnO TFTs (previous prototypes have been made in FDC's InGaZnO TFT process). This is particularly critical, as it will more easily allow the integration of polycrystalline CdTe detection directly on top of their respective ZnO-based APS circuits. These new active pixel sensors will use UTD's ZnO fabrication process. In order to transfer the multi-stage APS designs to a new and developing technology, however, it is necessary to establish some models for simulating the design. Thus, preliminary I-V curves of ZnO TFT samples were sent from the researchers at UTD to be analyzed and modeled here. A set of these curves are illustrated in Figure 9.3.

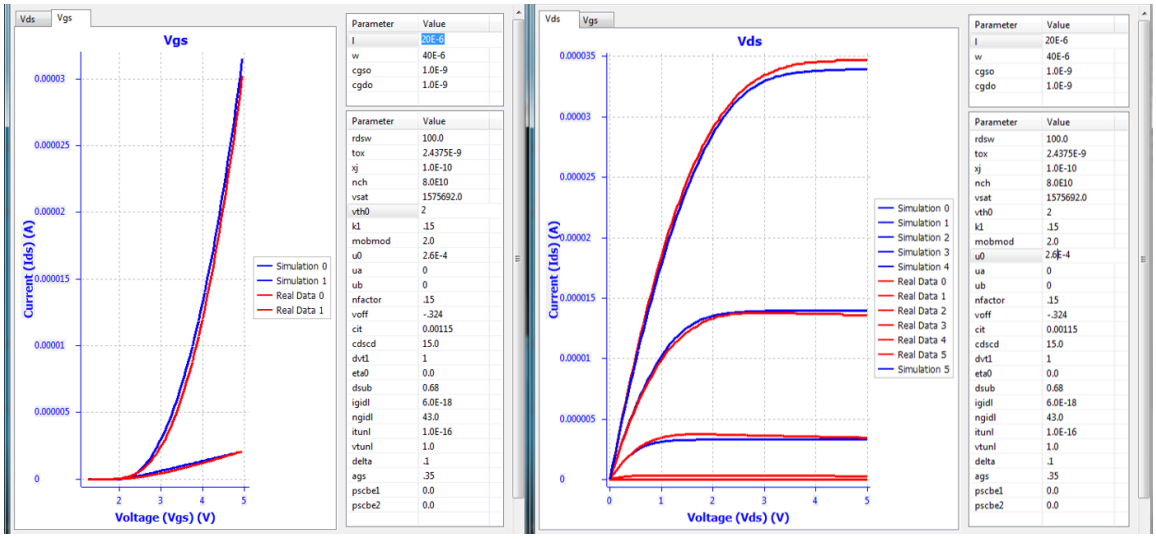

Figure 9.3: I-V characterization sweeps of a ZnO TFT. These sweeps were used to establish a working BSIM3 model later used in design and simulations.

These IV curves were then used to extract BSIM3 model parameters, which were subsequently used in spice level simulations. Example spice simulations of a ZnO based multistage APS may be seen in Figure 9.4. Specifically, the transient simulations show the alpha-induced output pulse from each stage within a 5-stage design. A DC sweep of the input voltage to a single CS stage was also simulated in order to determine the input biasing point needed for optimal gain (approximately 2-3V/V).

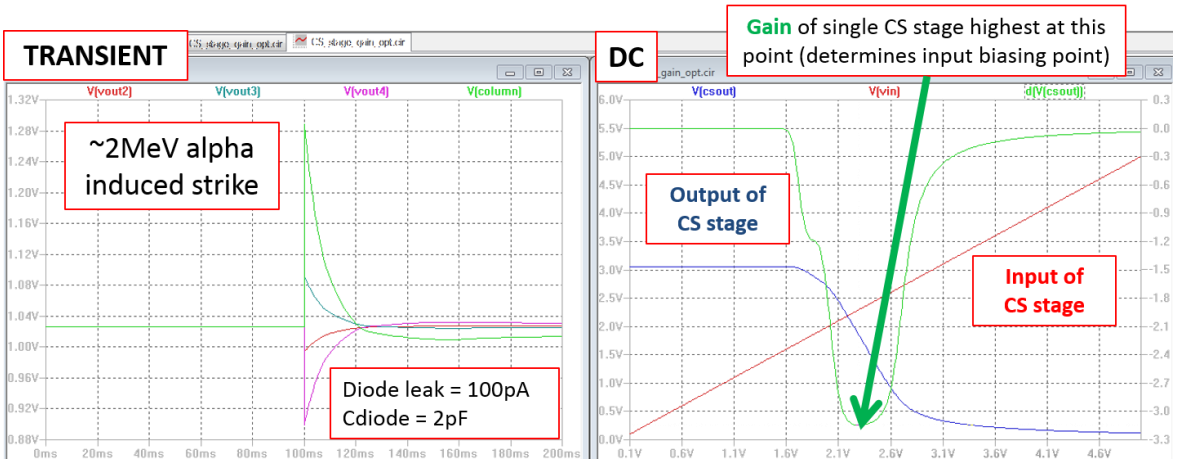

Figure 9.4: Transient analysis simulating the alpha response of a 5-stage APS using ZnO TFTs. DC analysis of Common Source (CS) stage.

Following schematic-level design, a layout of the new design was produced, and can be seen in Figure 9.5. The layout design has currently been fabricated, and is now being tested and evaluated similar to the previous generation of APS designs fabricated with IGZO TFTs.

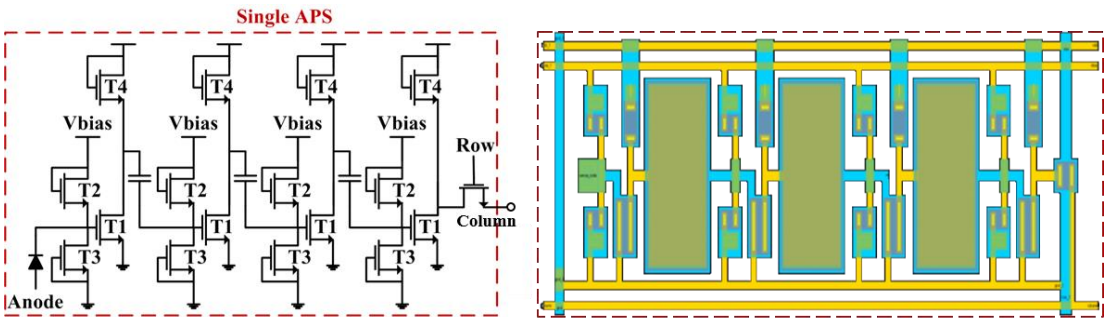

Figure 9.5: Schematic (Left) and Layout (Right) of a new ZnO TFT based APS

9.5 Development of the Detection Array

Once a reliable diode and APS integration is successfully achieved, in which incident alpha particles are reliably detected – work can then move forward on arraying individual pixels and developing the appropriate peripheral readout circuitry. Two separate array readout methodologies have been highlighted in a previous chapter.

The "AC coupled rows" technique requires the use of a low-power matched filter described in previous sections. Otherwise with increasing numbers of rows, the detected signals become much smaller, and would be quickly buried by external noise sources. Thus, each column would require a separate matched filter. The output of each matched filter could then easily be fed into a simple threshold detector in order to ascertain if a detection has occurred on a particular column. Unfortunately, however, an effective implementation of a matched filter would require very careful layout, and complex background tuning mechanism of a gm-C based ladder filter.

The alternative detection array implementation focuses on sampling each row. Prior analysis shows that this technique will provide optimal area scaling capability at the expense of more complex array signaling and power consumption. This all requires properly phased row driver circuitry along with analog to digital converters associated with each individual column. A similar readout technique was used for the earlier APS designs presented in [36][39]. The same hardware might be similarly reprogrammed to accurately read out detections from an array of newer multistage APSs.

REFERENCES

[1] Knoll, G. F. "Ionization Chambers", "Proportional Counters", "Scintillation Detector Principles", "Slow Neutron Detection Methods", and "Fast Neutron Detection Methods", Radiation Detection and Measurement 3rd Edition. Boston, MA: John Wiley & Sons (2000): 129-134, 159-169, 220-235, 310-311, 505-523, and 538-553.

[2] National Nuclear Data Center: Evaluated Nuclear Data File (ENDF) Retrieval & Plotting, http://www.nndc.bnl.gov/sigma/index.jsp?as=6&lib=endfb7.1&nsub=10, retrieved (7/23/2013)

[3] Schultis, J. K., Faw, R. E. "Radiation Detection", Fundamentals of Nuclear Science and Engineering. Boca Raton, FL: Taylor & Francis Group (2008): 206-229.

[4] McGregor, Douglas S., et al. "Design Considerations for Thin Film Coated Semiconductor Thermal Neutron detectors—I: Basics regarding Alpha Particle Emitting Neutron Reactive Films." *Nuclear Instruments and Methods in Physics Research Section A: Accelerators, Spectrometers, Detectors and Associated Equipment* 500.1 (2003): 272-308.

[5] Runkle, R. C., L. E. Smith, and Anthony J. Peurrung. "The Photon Haystack and Emerging Radiation Detection Technology." *Journal of Applied Physics* 106.4 (2009): 041101,041101-21.

[6] Ramírez-Jiménez, F. J., et al. "A Novel Application of a PiN Diode-Preamplifier Set for the Measurement of Charged Particles." *Nuclear Instruments and Methods in Physics Research Section A: Accelerators, Spectrometers, Detectors and Associated Equipment* 545.3 (2005): 721-6.

[7] Runkle, R. C., A. Bernstein, and P. E. Vanier. "Securing Special Nuclear Material: Recent Advances in Neutron Detection and their Role in Nonproliferation." *Journal of Applied Physics* 108.11 (2010).

[8] Kouzes, Richard T., et al. "Passive Neutron Detection for Interdiction of Nuclear Material at Borders." *Nuclear Instruments and Methods in Physics Research Section A: Accelerators, Spectrometers, Detectors and Associated Equipment* 584.2–3 (2008): 383-400.

[9] Kouzes, R. T. "The ^{3}He Supply Problem", PNNL -18288, (2009).

[10] M. L Wald, "Nuclear Bomb Detectors Stopped by Material Shortage", Nytimes.com (2009), Retrieved on 02-14-2012.

[11] McHugh, H., et al. "Laminated Amorphous Silicon Neutron Detector." *DOE report http://www.osti.gov/bridge/purl.cover.jsp* (2009).

[12] Nikolic, RJ, et al. "6: 1 Aspect Ratio Silicon Pillar Based Thermal Neutron Detector Filled with 10 B." *Applied Physics Letters* 93.13 (2008): 133502,133502-3.

[13] Shores, EF. "Data Updates for the SOURCES-4A Computer Code." *Nuclear Instruments and Methods in Physics Research Section B: Beam Interactions with Materials and Atoms* 179.1 (2001): 78-82.

[14] Shultis, J. Kenneth, and Douglas S. McGregor. "Efficiencies of Coated and Perforated Semiconductor Neutron Detectors". *Nuclear Science Symposium Conference Record, 2004 IEEE.* IEEE , 2004. 4569-4574.

[15] Solomon, CJ, et al. "A Hybrid Method for Coupled neutron–ion Transport Calculations for ^{10}B and ^{6}LiF Coated and Perforated Detector Efficiencies." *Nuclear Instruments and Methods in Physics Research Section A: Accelerators, Spectrometers, Detectors and Associated Equipment* 580.1 (2007): 326-30.

[16] Conway, Adam M., et al. "Numerical Simulations of Pillar Structured Solid State Thermal Neutron Detector: Efficiency and Gamma Discrimination." *Nuclear Science, IEEE Transactions on* 56.5 (2009): 2802-7.

[17] Phlips, Bernard F., et al. "Neutron Detection using Large Area Silicon Detectors." *Nuclear Instruments and Methods in Physics Research Section A: Accelerators, Spectrometers, Detectors and Associated Equipment* 579.1 (2007): 173-6.

[18] Subramanian, Mythili, Bernard Phlips, and Fritz Kub. "Characteristics of a Silicon on Insulator Neutron Detector". *Nuclear Science Symposium Conference Record (NSS/MIC), 2009 IEEE.* IEEE , 2009. 1306-1309.

[19] Kress, Kenneth A. "A Polymer Material-Composite Neutron Detector." *Nuclear Science, IEEE Transactions on* 28.1 (1981): 807-10.

[20] Orava, Risto, and Tom Schulman. "Ultra thin neutron detector, method for manufacturing the neutron detector and neutron imaging apparatus." U.S. Patent No. 8,022,369. 20 Sep. 2011.

[21] Almaviva, S., et al. "Thermal and fast neutron detection in chemical vapor deposition single-crystal diamond detectors." *Journal of applied physics* 103.5 (2008): 054501.

[22] Kaidashev, E. M., et al. "High electron mobility of epitaxial ZnO thin films on c-plane sapphire grown by multistep pulsed-laser deposition." *Applied Physics Letters* 82.22 (2003): 3901-3903.

[23] Bauhuis, G. J., et al. "Ultra Thin Tunnel Junction for use in III–V Multijunction Solar Cells". *Photovoltaic Specialists Conference (PVSC), 2012 38th IEEE.* 2012. 000909-000912.

[24] Jiang, Q., et al. "Growth of Thick Epitaxial CdTe Films by Close Space Sublimation." *Journal of electronic materials* 38.8 (2009): 1548-1553.

[25] Pelowitz, D. B. ed., MCNPX User's Manual v2.7.0 (Los Alamos National Laboratory report LA-CP-11-00438, Los Alamos, NM, 2011.

[26] X-5 Monte Carlo Team, MCNP – A General Monte Carlo N-particle Transport Code, Version 5 – Vol. II: User's Guide (Los Alamos National Laboratory report LA-CP-03-0245, Los Alamos, NM, 2008.

[27] Lide, D. R ed., CRC Handbook of Chemistry and Physics, 89th edition (CRC Press, Boca Raton, 2008.

[28] McGregor, Douglas S., and J. Kenneth Shultis. "Reporting detection efficiency for semiconductor neutron detectors: A need for a standard." *Nuclear Instruments and Methods in Physics Research Section A: Accelerators, Spectrometers, Detectors and Associated Equipment* 632.1 (2011): 167-174.

[29] Kouzes, R. T., et al. "Neutron Detector Gamma Insensitivity Criteria", Pacific Northwest National Laboratory report PNNL-18903, Richland, WA, 2009.

[30] Pacific Northwest National Laboratory, Specifications for Radiation Portal Monitor Systems Revision 6.7, Pacific Northwest National Laboratory report PNNL-14716, Richland, WA, 2003.

[31] Bossew, P. "A very long-term HPGe-background gamma spectrum." *Applied radiation and isotopes* 62.4 (2005): 635-644.

[32] McGregor, Douglas S., et al. "Thin-film-coated bulk GaAs detectors for thermal and fast neutron measurements." *Nuclear Instruments and Methods in Physics Research Section A: Accelerators, Spectrometers, Detectors and Associated Equipment* 466.1 (2001): 126-141.

[33] Knoll, Glenn F. , Radiation detection and measurement. John Wiley & Sons, (2010): 310–311.

[34] Schmid, G. J., et al. "A neutron sensor based on single crystal CVD diamond." *Nuclear Instruments and Methods in Physics Research Section A: Accelerators, Spectrometers, Detectors and Associated Equipment* 527.3 (2004): 554-561.

[35] Pressler, Daniel "System Modeling to Enhance Neutron Detection Design," Honors Thesis, Arizona State University, April 2012.

[36] Lee, Edward H., et al. "A low-noise dual-stage a-Si: H active pixel sensor." *Electron Devices, IEEE Transactions on* 59.6 (2012): 1679-1685.

[37] Yoo, Geonwook, et al. "Hemispherical thin-film transistor passive pixel sensors." *Sensors and Actuators A: Physical* 158.2 (2010): 280-283.

[38] Karim, Karim S., Arokia Nathan, and John Alan Rowlands. "Amorphous silicon active pixel sensor readout circuit for digital imaging." *Electron Devices, IEEE Transactions on* 50.1 (2003): 200-208.

[39] Kunnen, GR, et al. "Large Area Sensing Arrays for Detection of Thermal Neutrons". *Nuclear Science Symposium and Medical Imaging Conference (NSS/MIC), 2012 IEEE.* IEEE , 2012. 156-161.

[40] Bertuccio, Giuseppe, Pavel Rehak, and Deming Xi. "A novel charge sensitive preamplifier without the feedback resistor." *Nuclear Instruments and Methods in Physics Research Section A: Accelerators, Spectrometers, Detectors and Associated Equipment* 326.1 (1993): 71-76.

[41] Kaftanoglu, Korhan, et al. "Stability of IZO and a-Si: H TFTs processed at low temperature (200ºC)." *Journal of Display Technology* 7.6 (2011): 339-343.

[42] Marrs, Michael A., et al. "Control of threshold voltage and saturation mobility using dual-active-layer device based on amorphous mixed metal–oxide–semiconductor on flexible plastic substrates." *Electron Devices, IEEE Transactions on* 58.10 (2011): 3428-3434.

[43] Allee, David R., et al. "Circuit-level impact of a-Si: H thin-film-transistor degradation effects." *Electron Devices, IEEE Transactions on* 56.6 (2009): 1166-1176.

[44] Murphy, John W., et al. "Optimizing diode thickness for thin-film solid state thermal neutron detectors." *Applied Physics Letters* 101.14 (2012): 143506.

[45] Kunnen, G., et al. "TFT-based, multi-stage, active pixel sensor for alpha particle detection." *Electronics Letters* 50.9 (2014): 705-706.

[46] Hordequin, C., et al. "Nuclear radiation detectors using thick amorphous-silicon MIS devices." *Nuclear Instruments and Methods in Physics Research Section A: Accelerators, Spectrometers, Detectors and Associated Equipment* 456.3 (2001): 284-289.

[47] Pochet, T., et al. "Sensitivity measurements of thick amorphous-silicon pin nuclear detectors." *Nuclear Science, IEEE Transactions on* 43.3 (1996): 1452-1457.

[48] Despeisse, M. "Hydrogenated Amorphous Silicon Radiation Detectors", Semiconductor Radiation Detection Systems, FL: CRC Press (2010): 83-107.

[49] Murphy, J. W., et al. "Thin Film Cadmium Telluride Charged Particle Detectors for Large Area Neutron Detectors", Submitted to *Applied Physics Letters*.

[50] Turin, George L. "An introduction to digitial matched filters." *Proceedings of the IEEE* 64.7 (1976): 1092-1112.

[51] Haddad, Sandro AP. "Ultra low-power Biomedical signal processing", Diss. PhD Thesis, Delft University of Technology, (2006): 33-169.

[52] Johns, David A., W. Martin Snelgrove, and Adel S. Sedra. "Orthonormal ladder filters." *Circuits and Systems, IEEE Transactions on* 36.3 (1989): 337-343.

[53] Humpherys, DeVerl S. "The analysis, design, and synthesis of electrical filters", Englewood Cliffs, NJ: Prentice-Hall, 1970.

[54] De Lima, Jader A., and Wouter A. Serdijn. "A compact nA/V CMOS triode-transconductor and its application to very-low frequency filters." *Circuits and Systems, 2005. ISCAS 2005. IEEE International Symposium on.* IEEE, 2005.

[55] Schauman, R. "Transconductance-C Filters", Design of Analog Filters, 2nd Edition, NY: Oxford University Press, 2009, pp. 646-653.